UNIVERSIDADE FEDERAL DO PARANÁ

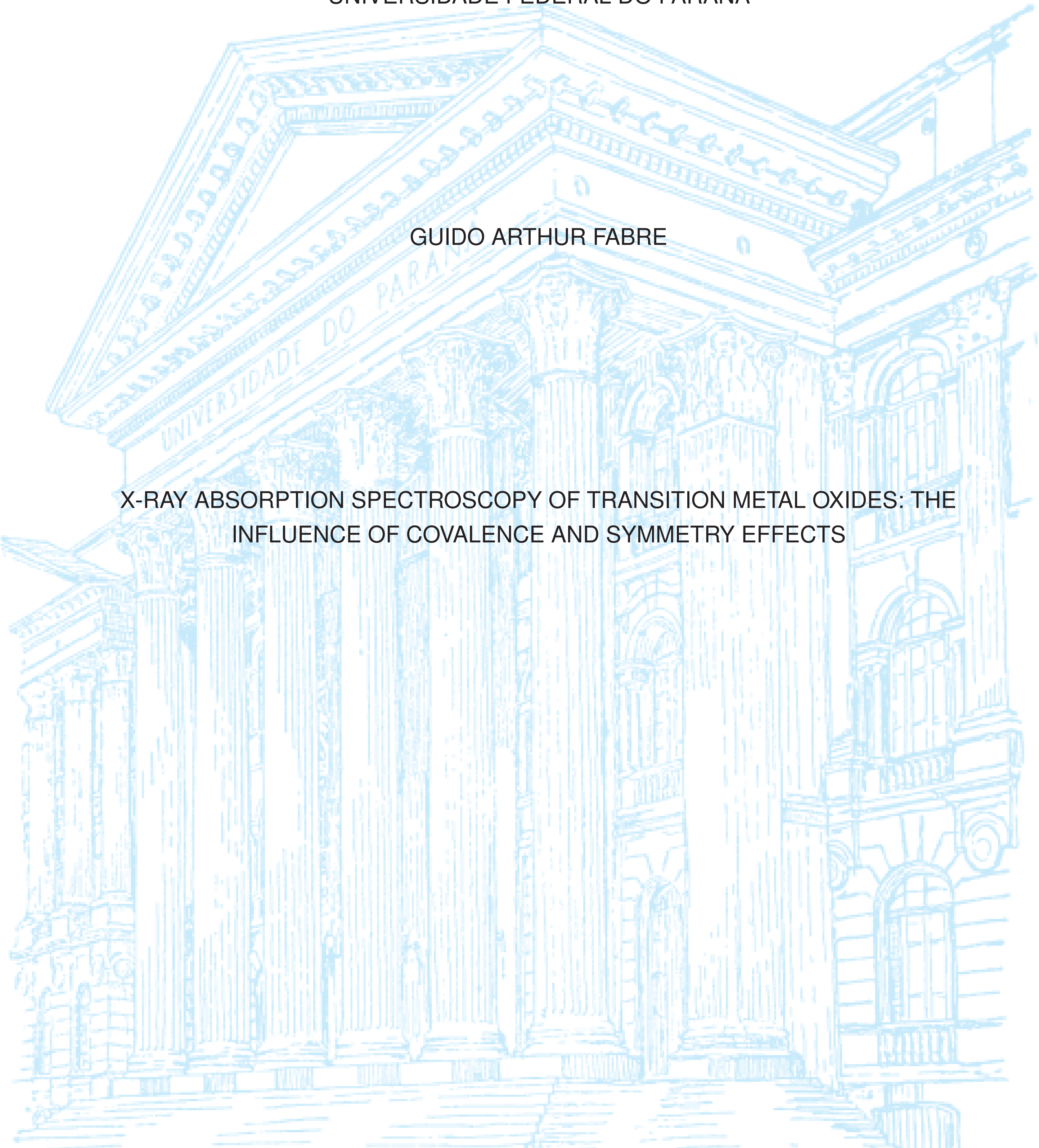

GUIDO ARTHUR FABRE

X-RAY ABSORPTION SPECTROSCOPY OF TRANSITION METAL OXIDES: THE INFLUENCE OF COVALENCE AND SYMMETRY EFFECTS

CURITIBA

2024

GUIDO ARTHUR FABRE

X-RAY ABSORPTION SPECTROSCOPY OF TRANSITION METAL OXIDES: THE INFLUENCE OF COVALENCE AND SYMMETRY EFFECTS

Dissertação apresentada ao Programa de Pós-Graduação em Física do Setor de Ciências Exatas da Universidade Federal do Paraná como requisito parcial para a obtenção de título de Mestre em Física.

Orientador: Prof. Dr. Rodrigo José Ochekoski Mossanek

CURITIBA

2024

DADOS INTERNACIONAIS DE CATALOGAÇÃO NA PUBLICAÇÃO (CIP)
UNIVERSIDADE FEDERAL DO PARANÁ
SISTEMA DE BIBLIOTECAS – BIBLIOTECA DE CIÊNCIA E TECNOLOGIA

Fabre, Guido Arthur
X-Ray absorption spectroscopy of transition metal oxides: the influence of covalence and symmetry effects / Guido Arthur Fabre. – Curitiba, 2024.
1 recurso on-line : PDF.

Dissertação (Mestrado) - Universidade Federal do Paraná, Setor de Ciências Exatas, Programa de Pós-Graduação em Física.

Orientador: Rodrigo José Ochekoski Mossanek

1.Espectroscopia de raio X. 2.Estrutura eletrônica. I. Universidade Federal do Paraná. II. Programa de Pós-Graduação em Física. III. Mossanek, Rodrigo José Ochekoski. IV . Título.

Bibliotecário: Leticia Priscila Azevedo de Sousa CRB-9/2029

MINISTÉRIO DA EDUCAÇÃO
SETOR DE CIÊNCIAS EXATAS
UNIVERSIDADE FEDERAL DO PARANÁ
PRÓ-REITORIA DE PESQUISA E PÓS-GRADUAÇÃO
PROGRAMA DE PÓS-GRADUAÇÃO FÍSICA - 40001016020P4

TERMO DE APROVAÇÃO

Os membros da Banca Examinadora designada pelo Colegiado do Programa de Pós-Graduação FÍSICA da Universidade Federal do Paraná foram convocados para realizar a arguição da Dissertação de Mestrado de **GUIDO ARTHUR FABRE** intitulada: **"X-Ray Absorption Spectroscopy of Transition Metal Oxides: The Influence of Covalence and Symmetry Effects"**, sob orientação do Prof. Dr. RODRIGO JOSÉ OCHEKOSKI MOSSANEK, que após terem inquirido o aluno e realizada a avaliação do trabalho, são de parecer pela sua APROVAÇÃO no rito de defesa.
A outorga do título de mestre está sujeita à homologação pelo colegiado, ao atendimento de todas as indicações e correções solicitadas pela banca e ao pleno atendimento das demandas regimentais do Programa de Pós-Graduação.

CURITIBA, 26 de Fevereiro de 2024.

Assinatura Eletrônica
27/02/2024 15:38:40.0
RODRIGO JOSÉ OCHEKOSKI MOSSANEK
Presidente da Banca Examinadora

Assinatura Eletrônica
27/02/2024 16:18:21.0
JULIO CRIGINSKI CEZAR
Avaliador Externo (LABORATÓRIO NACIONAL DE LUZ SÍNCROTRON)

Assinatura Eletrônica
28/02/2024 11:34:35.0
SERGIO D´ALMEIDA SANCHEZ
Avaliador Interno (UNIVERSIDADE FEDERAL DO PARANÁ)

This work is dedicated to all people that had even a little contribution to its making, specially the ones who were there in the most harsh times.

Acknowledgements

I would like to thank my supervisor, Professor Rodrigo Mossanek, for not only helping me become a better physicist and person, but also serving as an example of what kind of physicist I want to become. I want to be capable of at least having an idea of where I can find or even answer right there when someone asks me a question. For always having the patience and charisma that he had with me and my graduate colleagues when we had questions. Or at those times when we brought results without even knowing what they could mean. Always have good humor when something goes wrong and have the perseverance to make it right. Thank you for your help, trust, teachings and some memorable moments in these almost three years together. Thank you for being this great professor, supervisor, and partner in this academic path.

Also, I am grateful to Professor Miguel Abbate for introducing me to this area back in 2019. When I thought about quitting physics, you gave me the opportunity to find something that I would find incredible.

I thank the members of the two committees of the MSc course, Drs. Ismael L. Graff, Sergio d'A. Sanchez, Marlus Koehler, Alessandra de Souza Barbosa and Julio C. Cezar. Your suggestions and corrections helped to increase the quality of this work.

To all my professors during the undergraduate and Masters courses. Without you, I wouldn't know and become what I am today.

To my family, for all the support and courage given that made it possible to go through another academic phase. To Carol for all the companionship, love, and for putting up against all my anxiety crises just by being by my side. To my friends, for all the conversations, laughs, and, especially, gossip.

To CNPq for the scholarship.

And, of course, I would like to thank myself. For not giving up to the pressure and even when things didn’t look to have a good end, even small steps forward require some steps back.

"You gotta learn to let it all go, oh
And flow like the river"
Shawn James

RESUMO

Adquirir uma compreensão mais aprofundada da estrutura eletrônica dos óxidos de metais de transição (MT) continua sendo um desafio atual na física da matéria condensada. Isso pode ser alcançado investigando a ampla gama de propriedades simples e complexas exibidas por esses compostos. Entre as várias técnicas disponíveis para estudar a estrutura eletrônica, o foco deste trabalho está na espectroscopia de absorção de raios-X (XAS). Este método baseia-se em transições eletrônicas que ocorrem entre estados do núcleo e estados não ocupados da banda de condução, mostrando alta sensibilidade ao ambiente químico local. Uma análise completa é garantida ao considerar os efeitos completos do multipleto na valência nominal. Além disso, o fator de covalência, frequentemente negligenciado entre o MT e seus ligantes, é considerado, o que pode influenciar diretamente os resultados do estudo. Com o intuito de estender este trabalho, exploram-se simetrias alternativas (reduzidas) em relação às esperadas para óxidos de metais de transição. Neste trabalho, a XAS de diferentes óxidos de metais de transição, nomeadamente, manganês, ferro e cobalto, com as valências nominais de $2+$, $3+$ e $4+$, respectivamente, é analisada. Ao empregar as teorias de multiplete atômico e campo cristalino juntamente da implementação do método de interação de configurações, a energia do estado fundamental, a contagem de elétrons da banda 3d, o momento magnético e as espectroscopias XAS das bordas $2p$ do MT e $1s$ do O para ambos os sistemas são determinados, variando o número de configurações eletrônicas. Essas configurações eletrônicas descrevem a base do estado fundamental do sistema estudado e são o principal "ingrediente" para incluir adequadamente a covalência. Os cálculos são conduzidos assumindo a simetria octaédrica (O_h), como seria esperado para "*clusters*" de metais de transição da série 3d. Além disso, para abranger simetrias reduzidas de O_h, tornou-se necessário incluir um novo MT na lista, o vanádio, que manifesta a simetria piramidal quadrada (C_{4v}) em seu estado de oxidação $5+$, juntamente com a simetria tetragonal (D_{4h}) para Mn^{3+}. Através da análise dos resultados observa-se que, para descrever com precisão a estrutura eletrônica de qualquer um desses sistemas, independentemente da simetria exibida, é necessário um número maior de configurações eletrônicas em comparação com o que poderia ser esperado com base puramente em comparações experimentais. Essa dependência é particularmente influenciada pela valência nominal do metal de transição. Portanto, a interação covalente entre o MT e íons ligantes mostra-se crucial para caracterizar efetivamente a técnica XAS.

Palavras-chaves: Óxidos de metais de transição; estrutura eletrônica; espectroscopia de absorção de raios-X; simetria; configurações eletrônicas; covalência.

ABSTRACT

Gaining a better understanding of the electronic structure of transition metal (TM) oxides remains a current challenge in condensed matter physics. This can be achieved by investigating the diverse range of simple and complex properties exhibited by these compounds. Among the various techniques available for probing the electronic structure, the focus of this work is on X-ray absorption spectroscopy (XAS). This method relies on electronic transitions that occur between the core and unoccupied conduction states, showcasing a high sensitivity to the local chemical environment. A complete analysis is ensured by considering full multiplet effects on the nominal valence. Furthermore, the often overlooked covalence factor between TM and its ligands is acknowledged, which can directly influence the results of the study. In order to extend this work, alternative (reduced) symmetries are explored from those expected for transition metal oxides. In this work, the XAS of different transition metal oxides, namely manganese, iron, and cobalt, with nominal valences of $2+$, $3+$ and $4+$, respectively, is analyzed. By employing atomic multiplet and crystal field theories alongside with the implementation of the configuration interaction method, the ground state energy, 3d band electron count, magnetic momentum and the TM $2p$-edge, along with O $1s$-edge XAS spectra for both systems are determined, varying the number of electronic configurations. These electronic configurations describe the ground state basis of the system studied and are the main "ingredient" for properly accounting the covalence. The calculations are conducted assuming octahedral (O_h) symmetry, as one would expect for transition metal clusters of the $3d$ series. Additionally, to encompass reduced symmetries from O_h, it became necessary to include a new TM in the list, vanadium, which manifests the square pyramidal (C_{4v}) symmetry in its oxidation state of $5+$, along with the tetragonal (D_{4h}) symmetry for Mn^{3+}. Through the results analysis, it is observed that, in order to accurately describe the electronic structure of any of these systems, regardless of the exhibited symmetry, a larger number of electronic configurations is necessary compared to what might be expected based purely on experimental comparisons. This dependency is particularly influenced by the nominal valency of the transition metal. Therefore, the covalent interaction between TM and ligand ions proves to be crucial in effectively characterizing the XAS technique.

Key-words: Transition metal oxides; electronic structure; X-ray absorption spectroscopy; symmetry; electronic configurations; covalence.

List of Figures

List of Tables

Contents

CHAPTER 1

Introduction

In this introductory chapter, we lay the groundwork for a comprehensive study of transition metal oxides (TMOs), materials distinguished by their partially filled d-electron bands and an impressive variety of intrinsic properties. This chapter presents an introductory look at the electronic structure, a key to understanding the microscopical origin of the varied physical properties that TMOs can present. Next, a dedicated section on spectroscopic techniques unfolds, followed by a discussion about X-ray absorption spectroscopy (XAS) and its pivotal role in uncovering the electronic structure (ES) of TMOs. Further sections will articulate the objectives of the thesis, the motivations that drive this study, and the theoretical frameworks that underpin this research.

1.1 Transition Metal Oxides

Transition metals can be described as elements that have a partially filled d-electron band, or an element that can form stable cations with an incompletely filled d band [1]. In addition to that, f-block elements comprising lanthanides and actinides can be considered as transition metals as well. However, they are often called inner transition metals, since they have a partially filled f orbital. Furthermore, the group of elements zinc (Zn), cadmium (Cd) and mercury (Hg) is sometimes excluded from transition metals [2]. This is because they have the electronic configuration $Nd^{10}Ms^2$ ($N = 3, 4, 5$, $M = 4, 5, 6$), where the d shell is complete and also the d shell is complete in all their known oxidation states [2].

Now, in oxides, it is often considered as transition metals the elements separated in the three following series: $3d$ series (Ti - Cu), $4d$ series (Zr - Ag) and $5d$ series (Hf - Au), which can be seen in Figure 1. Many of these materials exhibit a crystalline structure resembling perovskite or perovskite-like arrangements, featuring a BO_6 octahedra, with B being the transition metal studied. A broader variation of this cubic perovskite structure can be expressed by the formula $ATMO_3$ or even A_2BO_4, known as layered perovskites, with A typically originating from a cation of the first or second columns of the periodic table. Additionally, certain perovskites may deviate from the conventional cubic configuration, displaying irregular or distorted octahedra, as exemplified by $LaMnO_3$ or $SrMn_{0.7}Mo_{0.3}O_3$, which will be explored further in subsequent chapters. Visual representations of these structures are provided in Figure 2 and Figure 3.

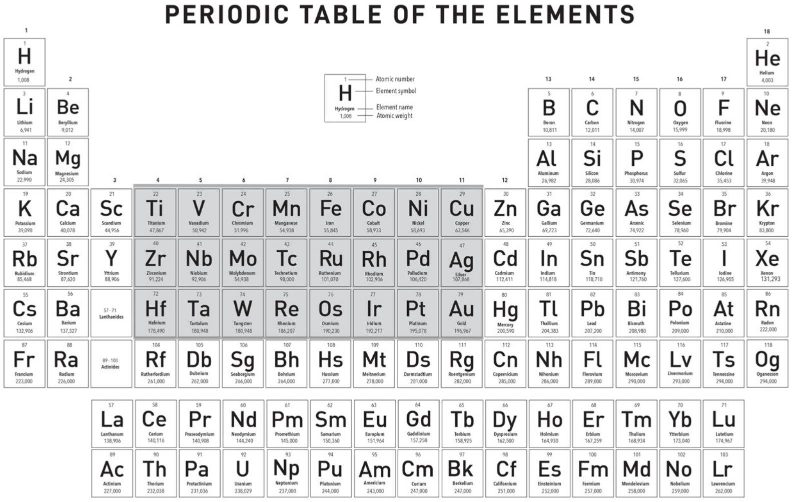

Figure 1 – Periodic Table with the relevant transition metals highlighted [3].

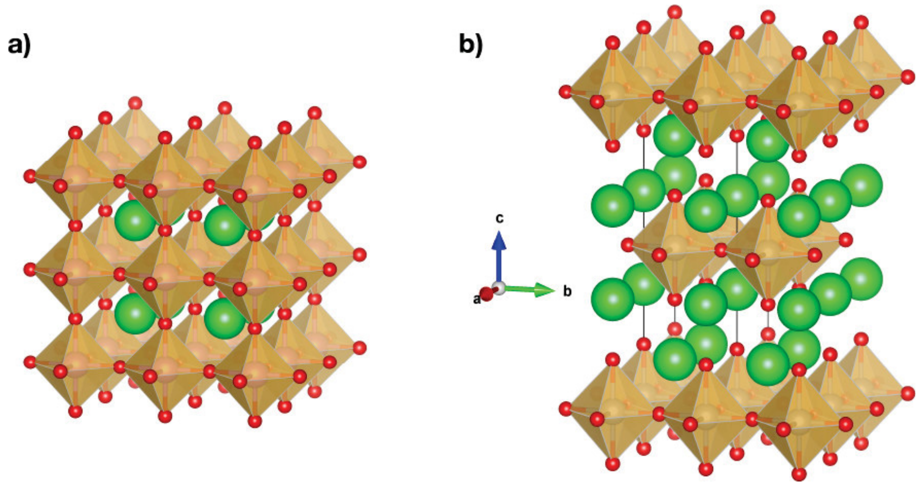

Figure 2 – (a) Crystal structure of a cubic perovskite with the ABO_3 formula, where A is represented in green, B in orange, and O in red. (b) Crystal structure of a layered perovskite with the A_2BO_4 formula, using the same color scheme for A, B, and O [4].

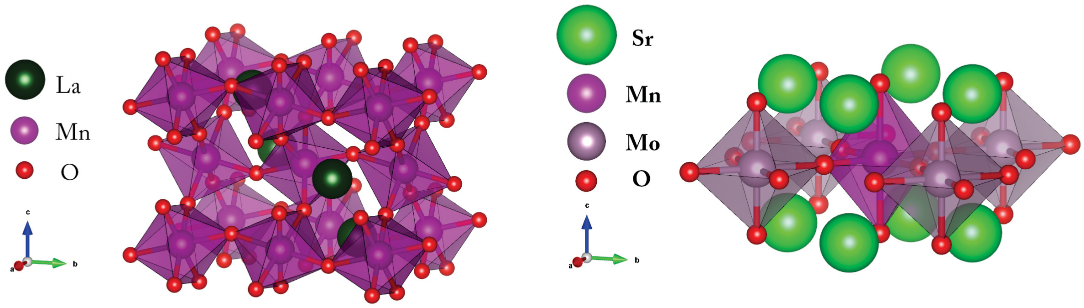

(a) (b)

Figure 3 – (a) Representation of the crystalline structure of the perovskite $LaMnO_3$ which presents a small distortion in the Mn cluster, but in this case it still can be considered an O_h cluster. (b) Crystalline structure of the double perovskite $SrMn_{0.7}Mo_{0.3}O_3$, on which with this specific molybdenum concentration, the manganese cluster is distorted sufficiently to be required to consider another type of symmetry that differs from the expected for $3d$ transition metals.

These materials exhibit a wide array of physical properties, making them a subject of great interest for both theoretical and experimental research. This array can span electrical, magnetic, optical, and other domains. What sets TMOs apart is not just these properties but also the complexity and unique ways in which they manifest. For example, the magnetic phase diagram of the double perovskite $La_{1-x}Sr_xMnO_3$, depicted in Figure 4, illustrates this diversity. The phase diagram for $La_{1-x}Sr_xMnO_3$ shows the full spectrum of strontium concentrations, mapping out the transition between various crystal structures, from Jahn-Teller-distorted orthorhombic to hexagonal, and magnetic states, ranging from paramagnetic to different antiferromagnetic configurations. It highlights the transition of the material across different electronic states, distinguishing insulating from metallic behaviors, thus illustrating the complex interplay of structural, magnetic, and electronic phases in this compound. This example highlights the wide range of characteristics observable in TMOs, from various crystalline structures to different spin ordering regimes, all within a single compound.

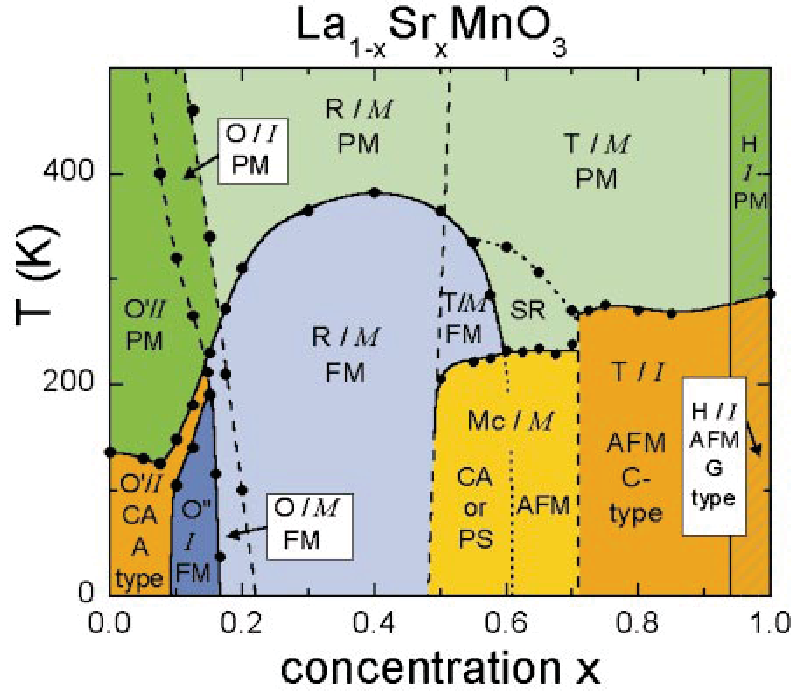

Figure 4 – Phase diagram of $La_{1-x}Sr_xMnO_3$ for the complete concentration regime. The crystal structures (Jahn-Teller distorted orthorhombic: O', orthorhombic O; orbital-ordered orthorhombic: O", rhombohedral: R, tetragonal: T, monoclinic: Mc, and hexagonal: H) are indicated as well as the magnetic structures [paramagnetic: PM (green), short-range order (SR), canted (CA), A-type antiferromagnetic structure: AFM (yellow), ferromagnetic: FM (blue), phase separated (PS), and AFM C-type structure] and the electronic state [insulating: I (dark), metallic: M (light)] [5].

This abundance of properties of TMOs can be credited to the relatively high electron correlation that the transition metal d bands encounter. So, there is some kind of intermediate state where these electrons are not delocalized, as for the s and p bands, but also they are not totally localized like f band electrons [6]. Because of this, these compounds can have a variety of classifications, such as insulators: $SrTiO_3$ [7], semiconductors: VO_2 [8] and good conductors: ReO_3 [9]. They can have paramagnetic character: $CaVO_3$ [10], antiferromagnetic: NiO [11] and ferromagnetic: $SrFeO_3$ [12]. There are also some compounds with peculiar properties such as high-temperature superconductivity: $La_{2-x}Ca_xCuO_4$ [13] and some have colossal magnetoresistance: $La_{1-x}Ca_xMnO_3$ [14]. In addition, because they are in oxide form, the covalent contribution of the oxygen ions can be crucially important for the study of the TMOs.

In summary, understanding the microscopic origins of the properties of transition metal oxides is central to this work and paves the way for deeper insights. This pursuit naturally leads us to examine their electronic structure, a complex endeavor that depends on the specific material under investigation and the property of interest. The next section will focus on unraveling the electronic structure, which is essential for understanding the origin and how the various properties of TMOs are given.

1.2 Electronic Structure

The electronic structure of a material refers to the arrangement and energy levels of the electrons within it. At its simplest, it is about which orbitals in an atom are filled with electrons and how these electrons are distributed. But more fundamentally, it is about how these electrons behave, how they move, interact with each other, and respond to external forces like electric and/or magnetic fields. These interactions are sensitive to the arrangement of atoms in a crystal lattice and can lead to a variety of ground states and excitations, such as magnetism, superconductivity, and metal-insulator transitions. The electronic structure dictates not only the material's response to external fields and stimuli but also its reactivity and stability.

The exploration of ES began around the dawn of the 20^{th} century, and it has been worked on ever since, from the development of the Drude Model by Paul Drude [15, 16] where the kinetic theory of gases was employed to analyze the electrical conductivity of metals around the year 1900, until the development of the electronic band theory, revealing that the arrangement of valence electrons determines whether a material exhibits metallic or insulating characteristics, where a visual explanation of these characteristics can be seen in Figure 5.

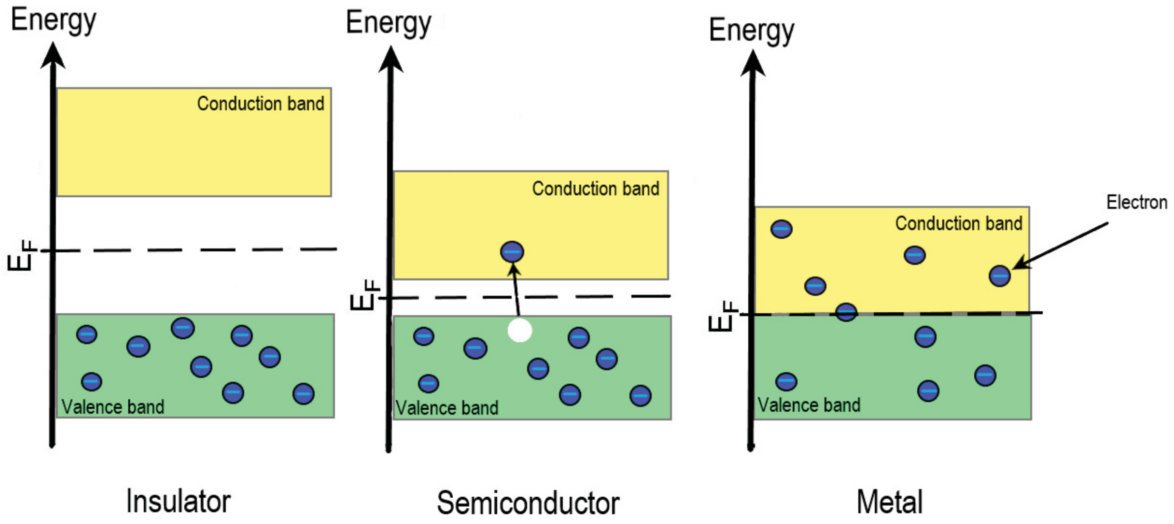

Figure 5 – Depiction of the electronic energy bands. When the valence band is partially filled or it overlaps with the conduction band for example, at absolute zero temperature, the material demonstrates metallic behavior, whereas a fully occupied valence band, creates an energy gap to an empty conduction band, transforming the material into an insulator. At finite temperatures, insulators with a small gap can be turned into semiconductors by temperature increase [17, 18].

However, while this theory has successfully predicted or explained the physical properties of numerous materials, it falls short for certain systems because of inherent approximations, such as the one-electron approximation. For example, a significant number of transition metal oxides featuring partially filled d valence bands were classified as insulators, a perplexing observation at the time [19]. The role of d valence electrons is crucial here, as they give rise to relatively localized bands, more so than p bands but less so than f bands. In this case, the electron-electron interaction cannot be ignored, leading to electronic correlation effects such as energy gaps among other effects. Recognizing this deviation from the predictions of band theory, N. F. Mott and R. Peierls postulated that strong Coulomb repulsion could be responsible for the insulating behavior of partially filled d systems [20], creating the field of *Strongly Correlated Systems*, which is the field of study of our research group. Mott further advanced the understanding of this intriguing state, known as a Mott insulator [20–24]. One of the primary methods employed to investigate the electronic structure of solids is the Density Functional Theory (DFT). Although DFT is close to an exact approach, it relies on various approximations that often hinder the accurate description of certain systems, especially those necessitating the incorporation of relatively higher electronic correlation effects. Another widely used approach involves model Hamiltonians such as the Anderson model [25] and the Hubbard model [24]. These models have considerable success in describing the electronic structure of materials, as they allow for the inclusion of effects such as atomic multiplet, electronic correlation, charge transfer, and more [26–31].

The electronic structure of materials can be directly probed using a range of X-ray spectroscopic techniques, including X-ray Absorption Spectroscopy, X-ray Photoemission Spectroscopy (XPS), and X-ray emission spectroscopy (XES), among others, as shown in Figure 6 [32]. Basically, the valence states consist of a filled valence band and an empty conduction band. XAS analyzes unoccupied electronic states, where X-rays are absorbed, causing core-level electrons to transition to higher energy states. This provides details on the oxidation states and local environments. XPS involves irradiating a material with X-rays to eject electrons, transitioning to continuum states, thereby revealing elemental compositions and chemical states. In XES, the core electron can be excited to either the continuum state, which is characterized as normal XES (NXES), or a nearby state, leading to the resonant XES process (RXES) [32]. NXES detects X-rays emitted during electron de-excitation, mapping both occupied and unoccupied electronic states. Lastly, RXES observes the absorption and subsequent reemission of X-rays, offering insights into dynamic electronic structures and transitions. These techniques together enable a multifaceted understanding of the electronic structure of materials, each contributing unique insights into their atomic and molecular configurations.

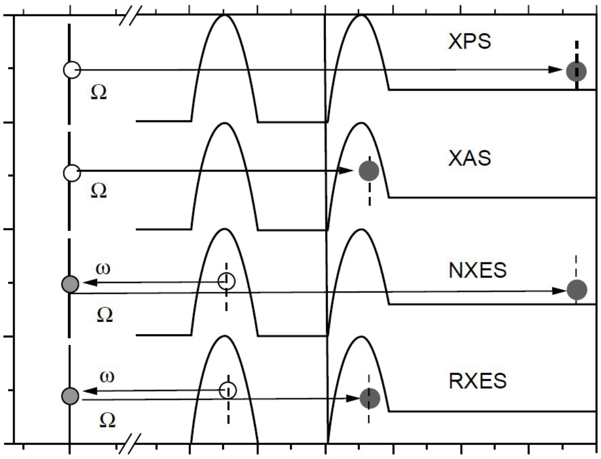

Figure 6 – Schematic representation, where the valence states consist of a filled valence band and an empty conduction band, which shows how the spectroscopic processes of XPS, XAS and XES work. In XPS, a core electron is excited by incident X-rays, transitioning to continuum states, and is subsequently detected as a photoelectron. In XAS, the core electron is excited to near energy states within the conduction band. In XES, the core electron can be excited to either the continuum state, which is characterized as normal XES, or a nearby state, giving rise to the resonant XES process [32].

Furthermore, the continuous evolution of these spectroscopic experimental techniques, propelled by the construction of advanced synchrotron light sources, enhanced equipment capabilities, and general technological progress, has fueled growing interest in the study of electronic structures of materials. Consequently, theoretical models employed to simulate and investigate the electronic structure must undergo continuous improvement to accommodate and explain the novel findings emerging from these advances. Understanding the electronic structure is thus not merely a theoretical pursuit, it is a gateway to material innovation and technological advancement.

1.3 Spectroscopy

Spectroscopy is the study and measurement of spectra resulting from the interaction of radiation with matter [33]. At its core, it revolves around the study of how matter interacts with electromagnetic radiation [34, 35]. These interactions, whether through absorption, emission, or scattering, offer profound insights into the structure and properties of materials at the most fundamental level [33–35]. Spectroscopy enables the study of the energy levels, chemical composition, and physical properties of a substance. By examining the absorption, emission, or scattering of light across various wavelengths, spectroscopy can reveal detailed information about the atomic and molecular structure of materials, as illustrated in Figure 7. This technique is pivotal in various fields, including chemistry, physics, astronomy, and environmental science. Different types of spectroscopy, such as infrared, ultraviolet-visible, and X-ray, are tailored to specific applications, making it an indispensable tool in both research and industry [33].

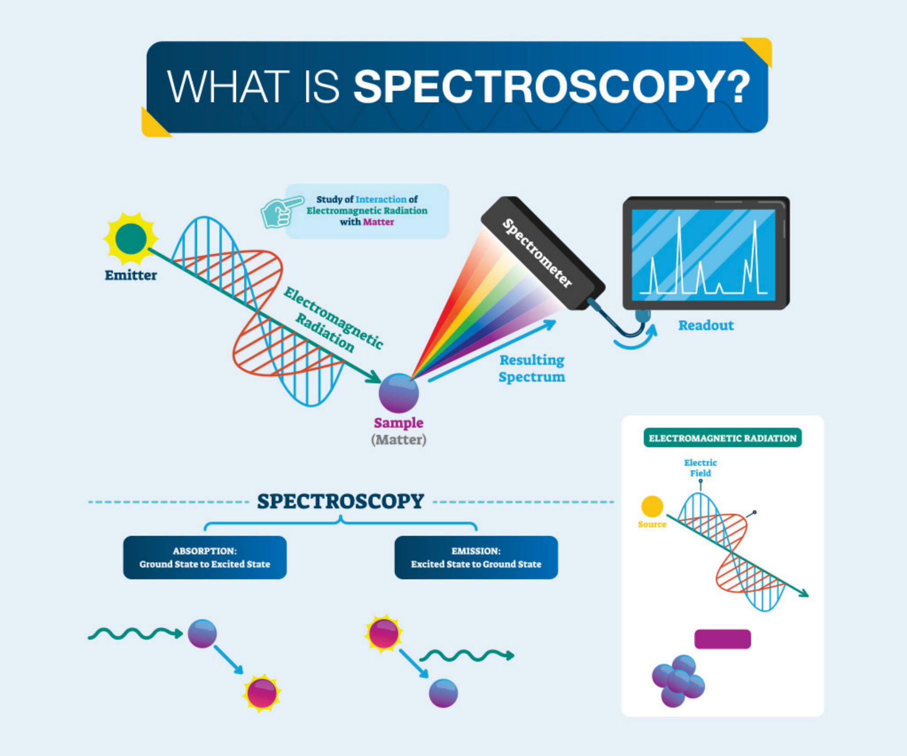

Figure 7 – An illustration depicting the concept of spectroscopy. The image shows a source that emits radiation that is being passed through a sample material. The radiation can interact with the sample in various ways, with two examples given: absorption and emission. The radiation is then split into various wavelengths, and a detector captures this spectrum, displaying a spectroscopy graph. This represents how spectroscopy analyzes the interactions between radiation and matter, revealing information about the composition and properties [33].

Since one of the focuses of this work revolves around the study of the electronic structure of TMOs, there is one type of spectroscopy very interesting to consider, the X-ray spectroscopy. It is a powerful tool for accessing and investigating the electronic structure of materials because it facilitates the access to portions of the ES at the atomic level, making it possible to study certain properties that conventional techniques, like specific heat or electrical conductivity measurements, may not be able to probe. For example, X-ray absorption spectroscopy can give access to the unoccupied portion of the ES [32], providing information on the oxidation states, as mentioned in the previous section.

But it is interesting to note that this technique, along with other X-ray techniques, is not so simple. It can depend on some certain aspects, and it can cause numerous interactions inside the structure of the sample that it is being studied, but its theoretical analysis can also be made in different ways, as will be seen in the next section.

1.4 X-ray absorption spectroscopy

X-ray Absorption Spectroscopy is a technique that focuses on the absorption of X-rays [32]. This process, which is rich in information, provides insights into the chemical and electronic properties of the materials studied. This makes XAS an indispensable tool in the study of complex materials, particularly the transition metal oxides, which are known for their intricate electronic structure and diverse physical properties as mentioned in previous sections. Furthermore, XAS is element specific due to the unique energy levels of core electrons in different elements, as shown in Figure 8, as an example of XAS spectra for different TMOs, which will be detailed in the next chapter. The figure shows that each TMO has its specific energy interval, making visible the specificity mentioned before. This specificity allows researchers to target specific elements in a compound or material, making it an invaluable tool in the study of complex systems where multiple elements are present.

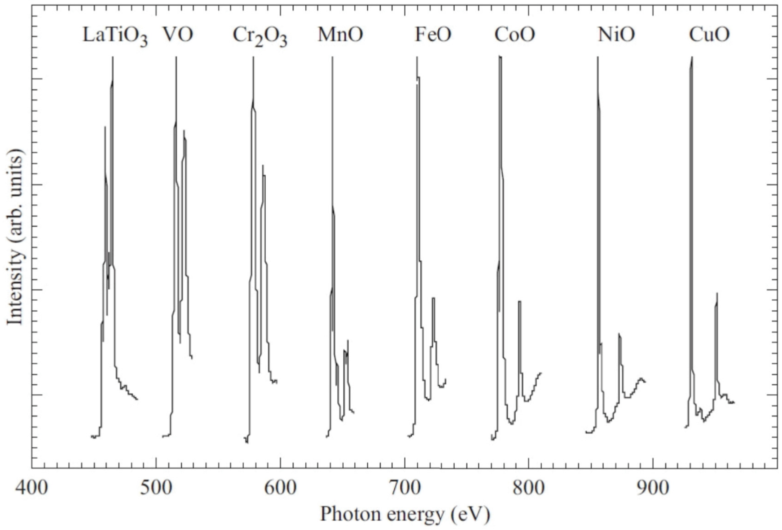

Figure 8 – XAS spectral profiles of various transition metal compounds, each showcased at distinct photon energies for each element, serving as a fingerprint for their identification [36].

At its heart, XAS is based on the interaction between X-ray radiation and the electrons within a material. When X-rays, with known and variable energy, $\hbar\omega$, are absorbed by a material, they induce transitions of core electrons to higher unoccupied energy states [32]. The subsequent relaxation of this state can occur through two primary pathways: fluorescence decay or Auger decay. In fluorescence decay, the vacancy in the core shell is filled by an electron from a higher energy level, emitting a photon characteristic of the energy difference between these shells [32]. Alternatively, in Auger decay, the energy released from the electron transition is transferred to another outer-shell electron, resulting in its ejection as an Auger electron [32]. The final state of the atom, post-relaxation, plays a significant role in determining the material's properties and is a key aspect of the investigation in XAS, aiding in the comprehensive understanding of materials at the atomic level.

One of the primary objectives of this research is to investigate the influence of covalence effects on the XAS results of TMOs. Historically, theoretical calculations used to interpret XAS results have often prioritized visually replicating experimental spectra [37–42]. While these calculations have been successful in providing a superficial resemblance to observed data, they often fail to fully account for covalence effects. Covalence, which refers to the sharing of electrons between atoms, plays a crucial role in determining the electronic structure and consequently the XAS results of TMOs, as will be shown in the sequence. The partial consideration of these effects in traditional models may lead to a gap in understanding the true nature of interactions within these materials. This gap can be seen in Figure 9, where a comparison is presented between theoretical spectra calculated considering the implementation used in this work (which is explained in Chapter 3.3), and the theoretical spectrum extracted from the literature [42].

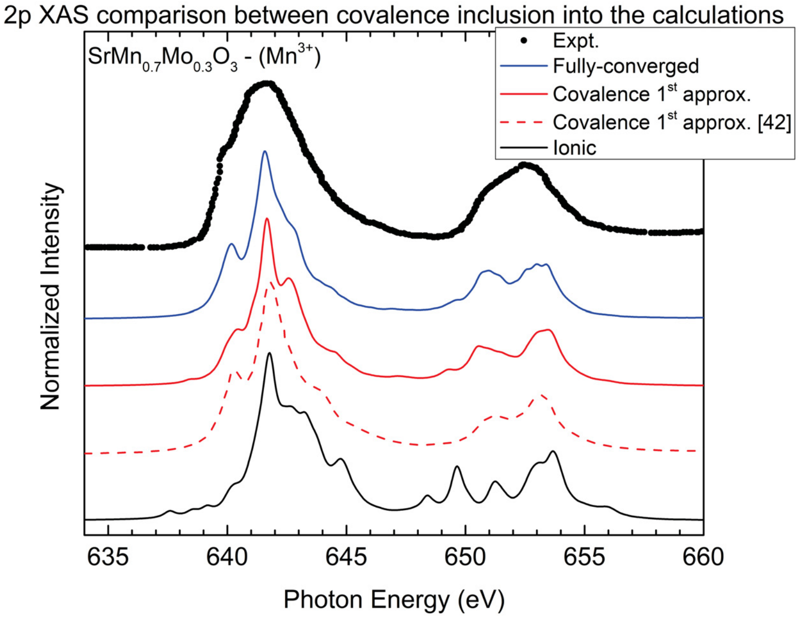

Figure 9 – Comparison between experimental [42] and theoretical data considering the inclusion of covalence in calculations taking into account the implementation used in this work and the one used in the literature.

The experimental data is extracted from the same reference [42]. The theoretical data calculated are divided into three types:

1. Ionic spectrum (black line) - In this case there is no interaction between TM and O and, as a consequence, no presence of covalence.

2. Covalence 1^{st} approximation spectrum (red full line) - In this case, it is considered the first step to include the covalence into the calculations, by increasing the size of the basis that describes the system one step beyond the ionic configuration. This case will be further studied in the next chapters.
3. Fully-converged spectrum (blue line) - Here, the calculation takes into account all possible interactions present considering the implemented model, in other words, it is considered the full multiplet effects and can be considered the most accurate to reproduce the experimental data (this case is better delved into in Chapter 5).

As for the theoretical spectrum obtained from the reference [42] (red dashed line), it has some aspects to be taken into account:

1. It is established in the field that parameters related to some atomic interactions (the Slater-Condon parameters [43] which are explained in Chapter 3 and Appendix B) are reduced to 80% of their atomic values to account for inherent charge screening effects [44]. However, in the reference considered in this example and others in the literature [45], the calculations were performed reducing these parameters even more, in this case to 60% of their atomic values, which is historically made to try to account for covalence effects.
2. In this case, the spectrum was obtained considering something similar to the covalence 1^{st} approximation used in this work. In this case, only the first step beyond the ionic configuration was considered.

As was mentioned earlier, partial consideration of the covalence effects can cause the clear difference between the two similar spectra, leading to an erroneous reproduction of the experimental data.

1.5 Objectives

This thesis has as main objective the study of the electronic structure of transition metal oxides, primarily manganese, iron, and cobalt. The initial property of interest of this work was only the covalence and how it could affect the results obtained by considering X-ray spectroscopy. By adopting an approach that fully incorporates covalence effects into theoretical models, this study seeks to provide a more accurate and nuanced interpretation of XAS data. Since an important part of the study of transition metal oxides resides in the TM cluster, changing the symmetry that the cluster manifests became another interest of this work, extending the analysis from only the covalence effects to include symmetry lowering effects in the results as well. As a consequence, another transition metal was included in the list, vanadium. As mentioned previously, through the use of X-ray absorption spectroscopy and the interpretation of the results along with comparison with experimental data, this research intends not only to advance the understanding on the electronic structure of TMOs but also to refine the methodologies used in spectroscopic analysis, thereby contributing to the broader field of condensed matter physics.

This thesis is divided in the following way: Chapter 2 presents a brief explanation about the interaction of X-rays with matter and gives a general view of X-ray spectroscopy. Then, a more detailed explanation about the specific technique used in this study is presented. Chapter 3 delves into the theory used in this work. It brings all the required "ingredients" utilized to perform all calculations and analysis about the effects of interest.

Chapter 4 has a bibliographic review of the systems studied. It has important properties, such as the crystalline structure, spin configuration, and specific information that each system can present that make them interesting to study.

Chapter 5 presents the results obtained considering the X-ray absorption spectroscopy of the $TM\ 2p$ and $O\ 1s$ edges of each system considered, for the related symmetry that they manifest. It presents an extensive discussion on how covalence and symmetry affect the outcomes of the technique used.

Chapter 6 presents the conclusions, and, finally, Appendix A has mathematical details about the origin of the Fermi's Golden Rule. Appendix B presents a more extensive explanation about the atomic multiplet theory and Appendix C has detailed calculations necessary in crystal field theory. Appendix D has a brief introduction on group theory regarding molecules, Appendix E presents details on how the main studied effects were implemented computationally, and, finally, Appendix F has the list of attended events during the Master's course.

CHAPTER 2

Spectroscopy and Electronic Structure

This chapter provides an introductory overview of the technique central to this study. It presents a brief explanation on the topic of interaction of X-rays with matter and a general view of X-ray spectroscopy. Later, the main technique employed in this work, X-ray absorption spectroscopy, is described in more detail.

2.1 Interaction of X-rays with matter

X-rays are defined as electromagnetic radiation with an energy in the range of about $100\ eV$ to around $100\ keV$ or between approximately $10\ nm$ and $10\ pm$ in terms of wavelength, as shown in Figure 10. It can be classified into two categories: soft X-rays, between around $100\ eV$ and approximately $3\ keV$, and hard X-rays, above around $3\ keV$. The intermediate range with photon energies of several keV is often referred to as tender X-rays [32, 46].

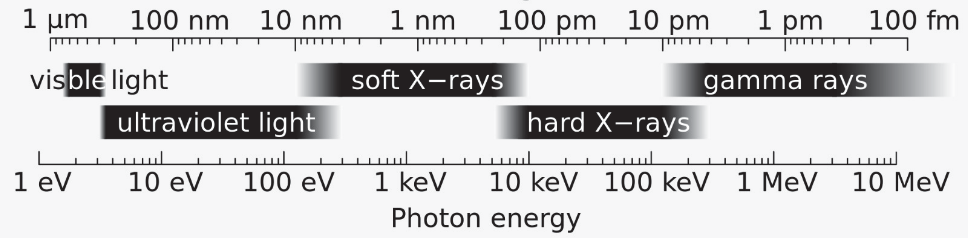

Figure 10 – Electromagnetic spectrum with the location of soft and hard X-rays between from around $10\ nm$ to approximately $10\ pm$ in terms of wavelength, or from around $100\ eV$ to approximately $100\ keV$ in terms of energy [47].

Upon striking a sample, an X-ray photon can undergo one of several interactions, with the strength of these interactions being influenced by both the X-ray energy and the elemental composition of the material. It may pass through without interaction, get absorbed, or be scattered. In the soft X-ray regime and at lower hard X-ray energies, the dominant interaction mechanism is typically photoabsorption or photoelectric absorption. In contrast, at higher energy levels, Compton scattering is dominant, as shown in Figure 11.

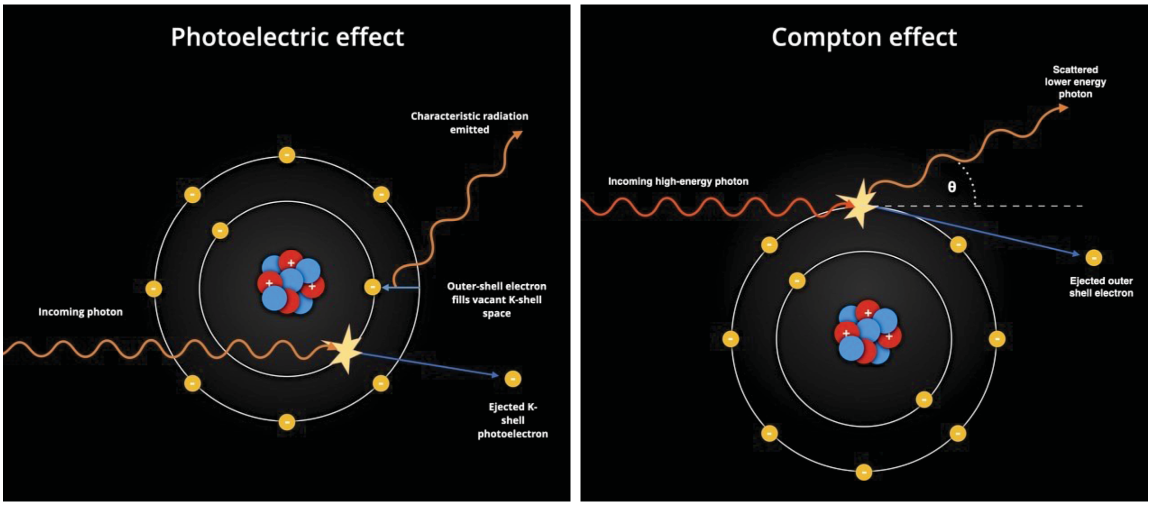

(a) (b)

Figure 11 – (a) Scheme illustrating how the photoelectric effect or absorption occurs. In a straightforward manner, a photon engages with the inner shell electron of an atom, removing it from its shell [48]. (b) As for the Compton effect, it serves as the primary driver of scattered radiation. This phenomenon arises from the interaction between a photon and either free or outer shell electrons. In this process, the incident photon undergoes scattering, changing its direction and transferring energy to the recoiling electron. Consequently, the scattered photon exhibits alterations in both wavelength and energy compared to their initial values[49].

In the case of absorption, an electron can absorb the photon, potentially becoming excited, which forms the basis for X-ray absorption techniques. Eventually, the photon can eject an electron as a photoelectron, giving rise to X-ray photoemission spectroscopy [32]. In the next section we will delve into the X-ray spectroscopy.

2.2 X-ray spectroscopy

X-ray spectroscopy is a powerful tool for accessing and investigating the electronic structure of materials, which fundamentally encompasses their physical and chemical characteristics. Although conventional techniques, such as measurements of specific heat, magnetic susceptibility, and electrical conductivity, can yield targeted insights into the ES, there are instances where the data from these methods may prove insufficient for a comprehensive understanding of the observed physical properties of a certain material. In such scenarios, the incorporation of X-ray spectroscopy techniques becomes necessary. For example, techniques like photoemission or X-ray absorption can be implemented simultaneously, given that they are complementary since they access the occupied and unoccupied ES, respectively. The depiction of this technique is presented in Figure 12. A more detailed explanation on X-ray absorption is given in the next section, since it is the technique used in this work.

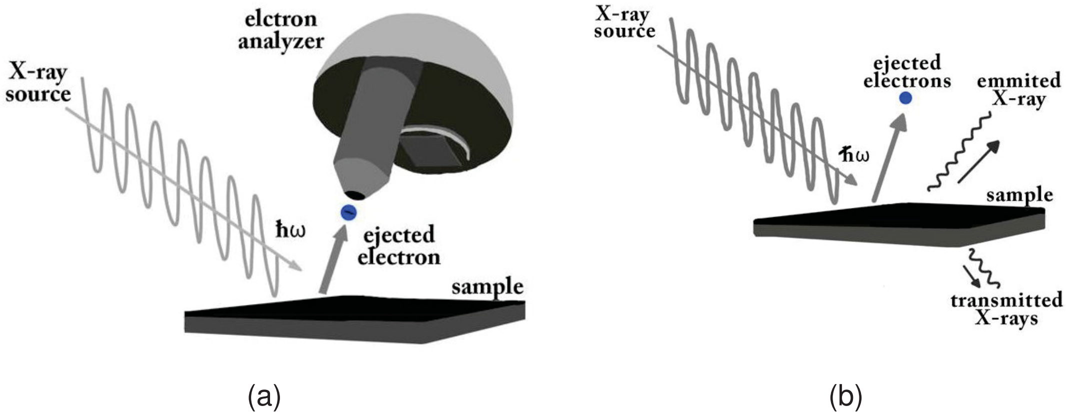

(a) (b)

Figure 12 – (a) Visualization of the XPS technique: X-ray photons impact the sample, leading to the ejection of electrons. Subsequently, an electron analyzer measures the kinetic energy of these ejected electrons. (b) Incoming X-ray photons are absorbed by the sample, causing the promotion of a core electron to the conduction band. Following this, the ionized system undergoes decay, leading to the creation of an X-ray photon or an electron.

2.3 X-ray absorption spectroscopy

X-ray absorption spectroscopy involves the irradiation of a sample with photons of known and variable energy $\hbar\omega$. To achieve this variability, experiments employing this technique are typically conducted using synchrotron radiation sources. At a specific energy interval, known as the absorption edge (E_{edge}), the absorption rate undergoes a sharp increase, defining the absorption edge. Photons with energies greater than E_{edge} are absorbed and excite an electron from a particular core level of the sample to unoccupied states within the conduction band [32].

Subsequent to the photon absorption, the core hole exists for approximately 10^{-15} seconds [32] before its decay, which can occur through either the emission of a photon, in a process known as "fluorescence", or the emission of an electron from a core or valence state in a process referred to as "Auger" decay, as shown in Figure 13. However, these are in a manner of speaking the main processes that can occur in the absorption process. It is important to emphasize that any of the decay processes can generate a cascade effect. In practice, the most common is the collection of all the electrons emitted from the grounding of the system and the connection of an ammeter to measure the current, leading to the measurement technique *Total Electron Yield*. As a consequence, the resulting spectrum should be given with current as a function of energy, but the current is eventually proportional to intensity, which is why the intensity is what appears in the results. The equation below depicts what happens to the sample, with valence state of d^n, when it is irradiated by photons with energy $\hbar\omega$. After the absorption of a photon, an internal electron will get excited leaving a core hole, $\underline{c}d^{n+1}$, and eventually it can decay through one of the processes described previously [32].

$$d^n + \hbar\omega \rightarrow \underline{c}d^{n+1} \rightarrow \begin{cases} d^n + \hbar\omega \ (Fluorescence) \\ d^{n-1} + e^- \ (Auger) \end{cases} \tag{2.1}$$

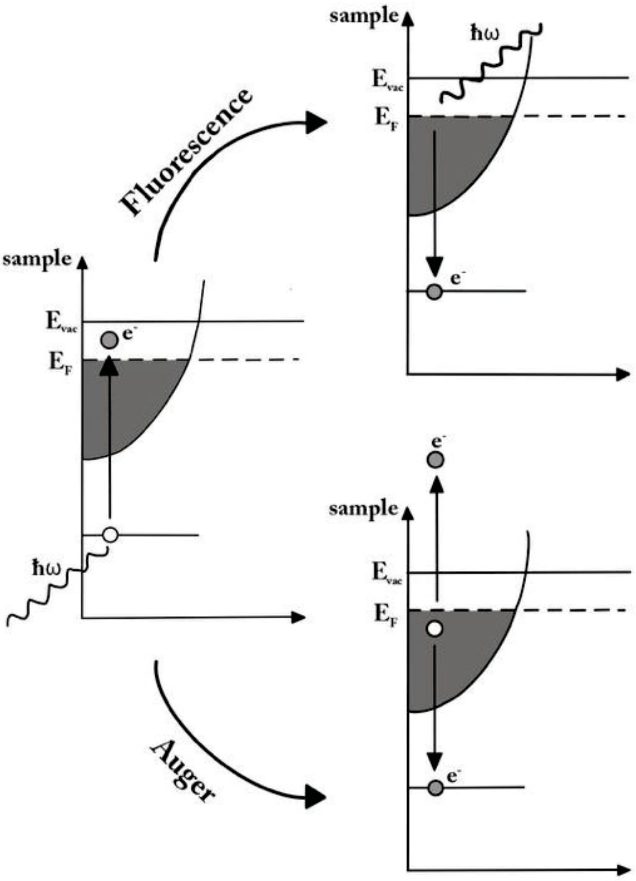

Figure 13 – Diagram showing how the decay processes in XAS are given. Following photon absorption, the system undergoes decay through either the emission of a photon (fluorescence) or the release of an electron (Auger).

The number of emitted photons in the case of fluorescence or Auger electrons ejected during Auger decay is directly proportional to the availability of unoccupied states that can be excited. Consequently, the X-ray absorption spectrum is directly linked to the unoccupied portion of the electronic structure.

Furthermore, the intensity of the spectrum is governed by the transition probability W_{fi} between initial (Φ_i) and final (Φ_f) states, which is determined by Fermi's Golden Rule:

$$W_{fi} \; \alpha \; \sum_f \left|\langle \Phi_f | \, \hat{e}_q \cdot \hat{r} \, | \Phi_i \rangle\right|^2 \delta \left(E_f - E_i - \hbar\omega\right). \tag{2.2}$$

Here, $\hat{e}_q$ denotes a unit vector for a polarization q and $\hat{r}$ is the position operator originated from dipole transition, E_i and E_f are the energies of the initial and final states, and $\hbar\omega$ is the incident photon energy. (For a detailed explanation on how this expression is obtained, refer to Appendix A). It is customary to separate the matrix element into radial and angular contributions, which can be accomplished with the use of the Wigner-Eckart Theorem [32] where the wave functions can be given in terms of the quantum numbers J and M, for both initial and final states. With this, the matrix element from equation 2.2 is written as:

$$\langle \Phi_f(JM) | \, \hat{e}_q \cdot \hat{r} \, | \Phi_i(J'M') \rangle = (-1)^{J-M} \begin{bmatrix} J & 1 & J' \\ M & q & M' \end{bmatrix} \langle \Phi_f(J) | \, \hat{e}_q \cdot \hat{r} \, | \Phi_i(J') \rangle. \tag{2.3}$$

The radial component determines the transition's line strength, while the angular component yields the dipole selection rules. These rules dictate that the overall momentum quantum number J cannot change by more than 1 ($\Delta J = \pm 1$), or $\Delta L = \pm 1$ when neglecting spin-orbit coupling. Furthermore, the magnetic quantum number M changes in accordance with X-ray polarization, with $\Delta M = q$ [32].

Figure 14 illustrates two examples of the XAS spectra addressed in this study. Specifically, it focuses on the TM $L_{2,3}$-edge and O K-edge or $2p$ and $1s$ edges, respectively. When probing the TM $2p$-edge, the unoccupied TM $3d$ states become discernible. The key features of the $L_{2,3}$-edge arise from dipole transitions originating from the core TM $2p$ level to the vacant TM $3d$ states [50]. These spectra exhibit two broad multiplet structures, distinguished by spin-orbit splitting [51] of the TM $2p_{3/2}$ (L_3 edge) and TM $2p_{1/2}$ (L_2 edge) [50]. Both edges are further divided into peaks with their intensity ratio dictated by the interplay of crystal field effects and electronic interactions, elaborated upon in the subsequent chapter.

With respect to the O $1s$-edge, absorption in this region provides insight into unoccupied states, primarily the O $2p$ band. For perovskite systems such as $ATMO_3$, the O $1s$ spectra typically manifest in three main segments, as shown in Figure 14 (b). The spectra exhibit a general shape corresponding to oxygen $2p$ states hybridized with metal $3d$ states. The configuration of these features correlates with the valency and spin state of the transition metal ion. Subsequently, the oxygen $2p$ states hybridize with the unoccupied states of A, which may vary depending on the rare-earth element present in the system, for example, the $La \rightarrow 5d$ states. Finally, the spectra encompass the O $2p$ states hybridized with the TM $4sp$ states [4]. In the case of simple or double oxides like TMO or TMO_2, the $O\ 1s$ spectra reveal structures associated with $TM\ 3d$ and $TM\ 4sp$ states [4]. However, in this work, due to the limitations of the implemented methods, the $O\ 1s$ spectra only feature the first portion of the complete spectra, the probing of the unoccupied $TM\ 3d$ states hybridized with the $O\ 2p$ states. In the next chapter, the required theory for one to be able to understand this work will be introduced.

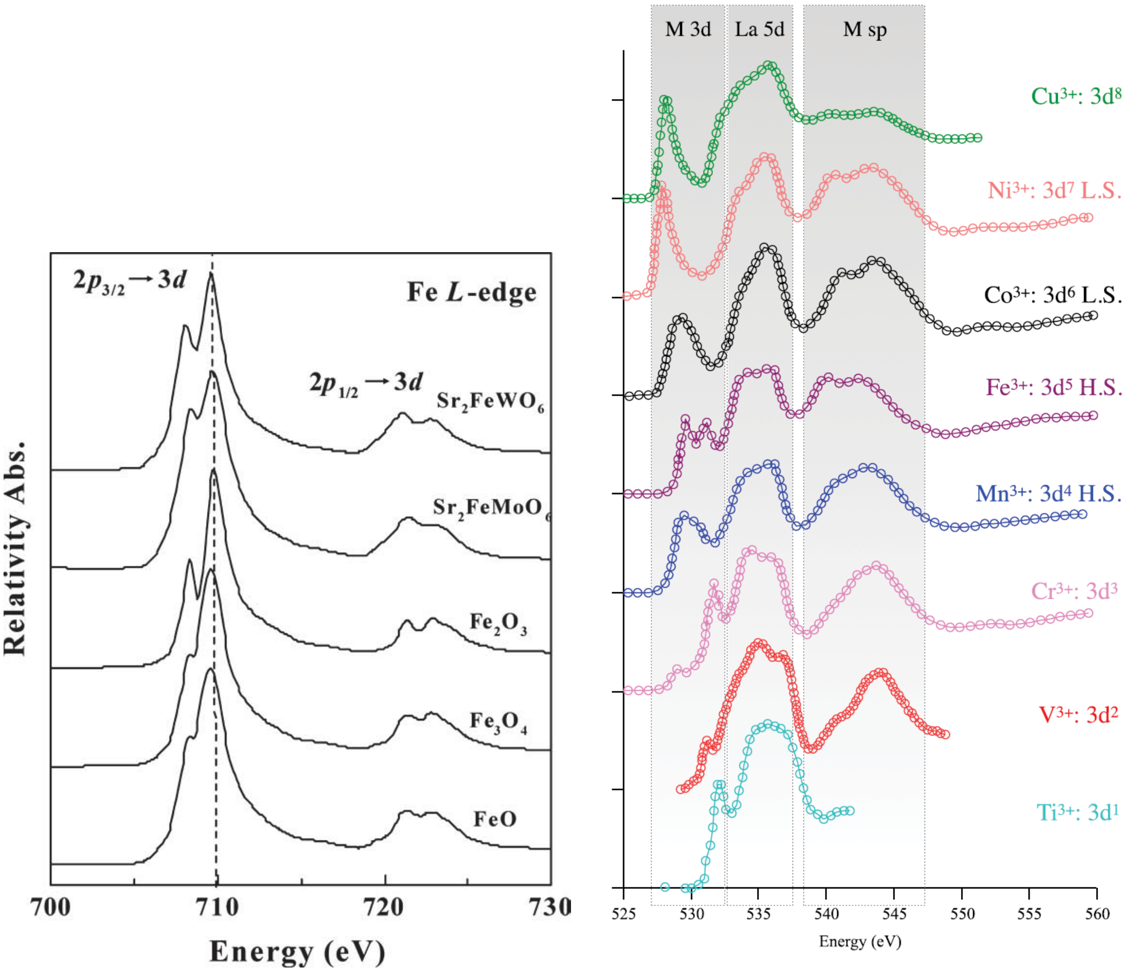

(a) (b)

Figure 14 – Illustration of the two types of XAS spectra analyzed in this study. (a) The main spectral features of the $L_{2,3}$-edge for iron originate from dipole transitions occurring between the core level ($Fe\ 2p$) and empty states ($Fe\ 3d$). The spectra exhibit two distinct multiplet structures, separated by the spin-orbit splitting effect in $Fe\ 2p_{3/2}$ (L_3 edge, approximately $705\ eV$ to $715\ eV$) and $Fe\ 2p_{1/2}$ (L_2 edge, around $715\ eV$ to $725\ eV$). These edges further divide into several peaks, depending on the analyzed system, and their intensity ratio is determined by the interplay of crystal field effects and electronic interactions [50]. (b) Oxygen K-edge spectra from a series of $LaTMO_3$ perovskites. The spectra exhibit a consistent general shape, featuring an initial single or double peak corresponding to oxygen $2p$ states hybridized with transition metal $3d$ states. The configuration of these features is related to the valency and spin state of the transition metal ion. At approximately $535\ eV$, the hybridization between $O\ 2p$ states with $La\ 5d$ states manifested, followed by oxygen $2p$ states hybridizing with the metal $4sp$ states [4].

2.4 Electronic structure and covalence

Before going through complicated techniques and models, it is necessary to know how to study the $TMOs$ and their electronic structure. First, one must understand the properties they present and can also be used to characterize them. There are two important parameters that are essential to describe the ES of transition metal oxides [52]. The first is the Coulomb repulsion energy (U), which represents the energy required for an electron to transfer between the energy levels of transition metals. The second key parameter is the charge transfer energy (Δ), which describes the energy necessary for an electron transfer between the transition metal and oxygen sites [52]. The interplay of these values categorizes the system into distinct regimes. These regimes are represented in a simpler adaptation of the diagram known as the Zaanen-Sawatzky-Allen (ZSA) diagram [52, 53]. The diagram is present in Figure 15, where the three main regions of the original diagram are represented by A, B, and C.

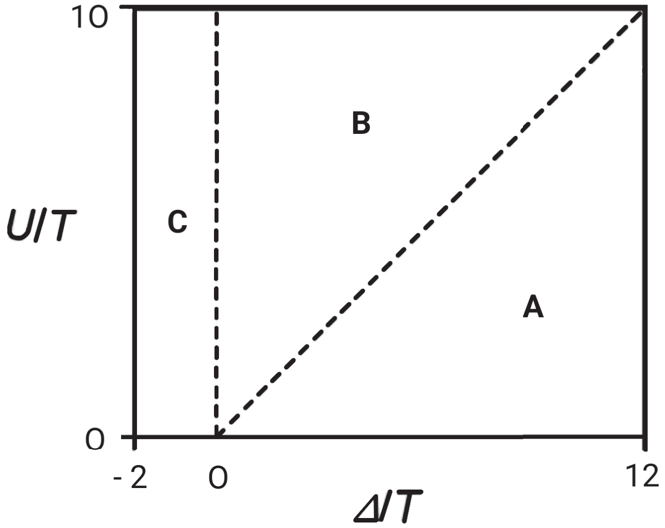

Figure 15 – Simplified ZSA diagram in terms of the repulsion energy U and the charge transfer energy Δ, both in hybridization units (T). The regions of the diagram are related to three main regimes that $TMOs$ can be characterized. A: $\Delta > U \rightarrow$ *Mott-Hubbard regime*; B: $\Delta < U \rightarrow$ *Charge Transfer regime*; C: $\Delta < 0 \rightarrow$ *Negative Charge Transfer regime*.

In the ZSA diagram's region A, where $\Delta > U$, the system is in the Mott-Hubbard regime. In this case, the electronic structure, particularly the d states, tends to lie next to the Fermi level (E_F), which is defined as the highest energy level that an electron can occupy at absolute zero temperature [54]. Thus, the electronic structure in the Mott-Hubbard regime is dominated by transition metal d states. An illustration of this can be seen in Figure 16 (a). Also, the occupied (unoccupied) bands are represented by the solid (open) structures and the dashed lines are the Fermi level (E_F). It is possible to see that the band gap value in the case of the Mott-Hubbard regime is proportional to the value of U. This means that electrons and holes move through the $TM\ d$ bands and are said to be *heavy*, due to the low dispersion of the d band. In region B, where $0 < \Delta < U$, the system is in the Charge-Transfer regime, where the band gap is now proportional to Δ, as illustrated in Figure 16 (b). The ES has a mixed p-d character next to the Fermi level E_F. Here, the electrons are *heavy* due to the low dispersion of the d bands, while the holes are *light*, due to the greater dispersion of the p bands. This causes excitations to occur from occupied $O\ 2p$ to unoccupied $TM\ d$ states [52, 53, 55].

There is also the possibility that Δ exhibits negative values ($\Delta < 0$), which characterizes the Negative Charge Transfer regime, given by region C of Figure 15 and depicted in Figure 16 (c). Here, the band gap is again proportional to Δ and the electronic structure has a p-p character. In this case, electron transfer from $O\ 2p$ to the $TM\ d$ band is favorable, pushing the oxygen $2p$ band close to E_F and pushing the $TM\ d$ band to negative energies. However, the region above the Fermi level also exhibits both $TM\ d$ and $O\ 2p$ character [56].

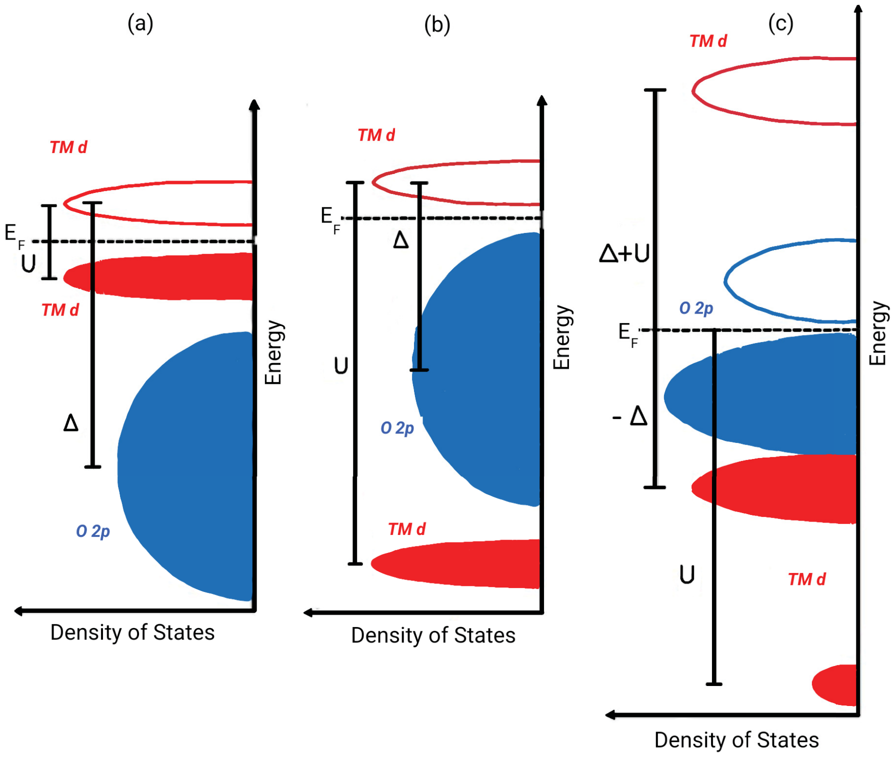

Figure 16 – Illustration of the electronic structure of transition metal oxides in the Mott-Hubbard (a), Charge Transfer (b) and Negative Charge Transfer (c) regimes.

Covalence, the sharing and transfer of electrons between transition metal and oxygen ligand atoms, emerges as a pivotal factor in defining the electronic structure of TMOs across the Mott-Hubbard, Charge-transfer, and Negative Charge-transfer regimes. It plays a crucial role in determining the classification of TMOs within these regimes [53], since with the increasing of this factor by including hybridization between $TM\ d$ and $O\ 2p$ orbitals, the charge transfer effect become more important [55]. Covalence is not just a bonding mechanism, it is essential for understanding the complex electron interactions and behaviors in TMOs. By examining covalence, we gain deeper insights into the nature of charge transfer, the formation of electronic bands, and the resultant physical properties of these materials, emphasizing its significance in the study of TMOs' electronic structures.

After all this discussion, we are ready to see how and which theories are required to perform the study on the electronic structure of TMOs. More specifically, how the covalence can be included properly in theoretical simulations and how it is possible to interpret the outcomes obtained.

CHAPTER 3

Theoretical Methods

This chapter introduces the theoretical methods used to interpret the experimental data extracted from the literature. The cluster model plays a central role, incorporating a model Hamiltonian that effectively describes many-body effects. To ensure accuracy in this approach, we took full multiplet effects into consideration by employing three important theories: the atomic multiplet, crystal field, and charge-transfer multiplet. Additionally, because one of the main focus of this work is to study the covalence effects in the TMOs, it is required to account for possible charge transfer effects. For that, the configuration interaction method was implemented, which, in a simple view, consists of the expansion of the basis that describes the system studied. So, basically to produce the results obtained in this work, it is necessary to consider two basic things, a model Hamiltonian and the basis of the problem, which requires their specific ingredients to be properly employed. This chapter, therefore, is structured around these aspects and concludes with a discussion of the practical implementation of these theories.

3.1 Model Hamiltonian

In this work, the model we use is framed by a model Hamiltonian, which varies based on the specific interactions we need to consider. It includes the usual kinetic and potential energy components like a common problem given in undergraduate modern physics books, but additional interactions depend on the particular system and technique in use. Therefore, the next sections will detail the construction of the model Hamiltonian for this study, focusing specifically on examining covalence effects in the

XAS of transition metal oxides.

3.1.1 Multiplet Calculations

In order to perform calculations using X-ray absorption spectroscopy at the $L_{2,3}$-edge of $3d$ transition metals, it is necessary to consider transitions like $2p^6 3d^n \rightarrow 2p^5 3d^{n+1}$. Furthermore, to provide an accurate description of the absorption spectra of these compounds, it is essential to consider the $3d$-$3d$ and $2p$-$3d$ interactions. Both interactions define the ground state (GS) $(2p^6 3d^n)$ and separate the final state (FS) $(2p^5 3d^{n+1})$ in various configurations. It is possible to write the atomic multiplet Hamiltonian in a more general way like [32]:

$$\hat{H}_{atomic} = \hat{H}_{average} + \hat{H}_{multiplet}. \tag{3.1}$$

Here, $\hat{H}_{average}$ accounts for the kinetic energy and electron-nucleus interactions and is considered a constant. In essence, it represents the system's average energy or its "center of gravity" within the multiplet. The multiplet separation, on the other hand, is governed and addressed by $\hat{H}_{multiplet}$, which can be expressed as [32]:

$$\hat{H}_{multiplet} = \hat{H}_{dd} + \hat{H}_{p\vec{L}\cdot\vec{S}} + \hat{H}_{pd} + \hat{H}_{CF}, \tag{3.2}$$

where $\hat{H}_{dd}$ represents the $3d - 3d$ Coulomb interactions, $\hat{H}_{p\vec{L}\cdot\vec{S}}$ represents the spin-orbit coupling of the $2p$ core hole, playing a crucial role in the separation of the $2p_{3/2}$ and $2p_{1/2}$ contributions at the XAS spectrum [51]. $\hat{H}_{pd}$ includes the Coulomb and exchange interactions involved in the $2p - 3d$ transition. Lastly, $\hat{H}_{CF}$ is responsible for the crystal field effect exerted by the local environment in which the cluster is situated. Figure 17 presents the effect of each of the contributions of $\hat{H}_{multiplet}$.

In the top curve, there is only $\hat{H}_{dd}$. In the second curve, the spin-orbit coupling $\hat{H}_{p\vec{L}\cdot\vec{S}}$ is included. It separates the $Fe\ 2p$ level into the contributions $Fe\ 2p_{3/2}$ and $Fe\ 2p_{1/2}$ [50]. The third curve introduces the $\hat{H}pd$ term, while the fourth and final curve reflects the complete $\hat{H}_{multiplet}$, which includes the crystal field term. Notably, this last effect is sensitive to the chemical environment, because it is the one where crystal field effects are being introduced.

The calculations were carried out using the script language *Quanty* [57]. To address the Coulomb and exchange contributions, the Slater Integrals [58, 59] (F and G, as elaborated later), were deliberately reduced to 80% of their ab initio values, as is customary in this field, to account for intra-atomic screening and electronic correlation effects [44]. Now, the following sections will delve into the theories responsible for explaining the effects present in the multiplet calculations and extend the discussion about what are the "ingredients" necessary to compose the model Hamiltonian.

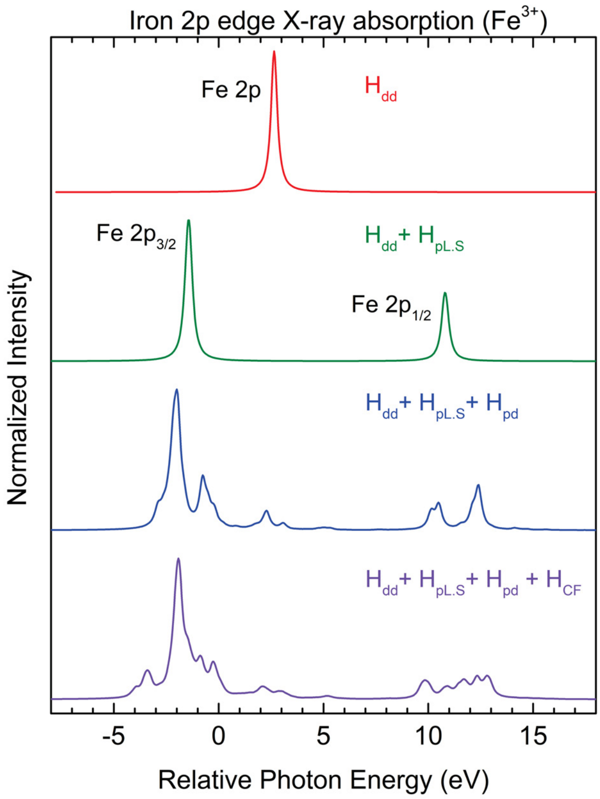

Figure 17 – Multiplet calculation for the iron ion of valency Fe^{3+} $(3d^5)$. Each graph panel shows the effects of each contribution of the multiplet Hamiltonian $\hat{H}_{multiplet}$.

3.1.2 Atomic Multiplet Theory

The atomic multiplet theory is the description of the atomic structure with quantum mechanics. The main idea is to solve the Schrodinger equation for a N-electron atom, given by:

$$\hat{H}_N \left|\psi\right\rangle = E_N \left|\psi\right\rangle , \tag{3.3}$$

where the Hamiltonian $\hat{H}_N$ is given by [32]:

$$\hat{H}_N = \sum_{i}^{N} \frac{\hat{P}_i^2}{2m} - \sum_{i}^{N} \frac{Ze^2}{|\hat{r}_i|} + \sum_{pairs} \frac{e^2}{\hat{r}_{ij}} + \sum_{i}^{N} \xi\left(\hat{r}_i\right) \hat{L}_i \cdot \hat{S}_i. \tag{3.4}$$

Here, the first two terms contribute to the result as an average energy, or $\hat{H}_{av}$. The e-e interaction and spin-orbit terms define the relative energy of the different terms within the specific configuration. When dealing with valence electrons, particularly in light elements, spin-orbit coupling can often be neglected in favor of pure LS-coupling. To obtain what is important for this work, it is required to evaluate the matrix elements of the electron-electron interaction. There is a more detailed process to obtain the required results, which is presented in Appendix B for reference. For now, let us attain to the important considerations. To get to the desired conclusions of this theory, it is possible to make use of the two-electron state characterization to be able to write in a more manageable way the e-e matrix elements, providing the following equation:

$$\langle \psi_i;\psi_j| \frac{e^2}{r_{ij}} |\psi_p;\psi_q\rangle = \langle \psi_i;\psi_j| \sum_{k=0}^{\infty} \frac{e^2 r_<^k}{r_>^{k+1}} P_k\left(\cos\Omega\right) |\psi_p;\psi_q\rangle \,, \tag{3.5}$$

where the indexes i, j, p and q represent the states of electrons 1 and 2. The sum represents an expansion of the original e-e interaction term, $\frac{e^2}{r_{ij}}$, in terms of Legendre polynomials (P_k), with $r_<$ and r_k being the distance of electrons 1 and 2 (r_1 and r_2) and Ω the angle between their distances.

It is possible to separate this solution into radial and angular parts. The real interest lies in the radial part, where, through the use of the Slater-Condon (S-C) Integrals [43] and some other approximations (some present in Appendix B), the desired result is obtained in the form of the equation.

$$\langle \psi_i;\psi_j| \frac{e^2}{r_{ij}} |\psi_p;\psi_q\rangle = \sum_{k=0}^{\infty} \left[\overbrace{f_k F^K}^{Direct} + \overbrace{g_k G^k}^{Exchange} \right] . \tag{3.6}$$

Due to the fact that transition metals have a valence state of d^n, which has an orbital angular momentum $l = 2$, the possible values of the k index of the Slater-Condon integrals F and G are $k = 0, 2, 4$ for the direct term and $k = 1, 3$ for the exchange term, respectively. It is common to express the matrix elements for the e-e repulsion in terms of the normalized S-C parameters, or even in terms of the Racah parameters [32], which are a simplified version of the S-C parameters, since they are defined as linear combinations of the normalized S-C parameters. The relation between each parameter mentioned can be seen in the following.

$Slater - Condon$	$Normalized\ S - C$	$Racah$
F^0	$F_0 = F^0$	$A = F_0 - 49F_4$
F^2	$F_2 = \frac{F^2}{49}$	$B = F_2 - 5F_4$
F^4	$F_4 = \frac{F^4}{441}$	$C = 35F_4$

It is more convenient to express the results in terms of the cubic harmonic basis rather than the spherical harmonic basis, since the first describes, in a more useful way, chemical orbitals. Because of that, it is possible to write either the normalized Slater-Condon or Racah parameters using the Kanamori parameters [60, 61]. This new set of parameters is also useful due to the fact that they describe in a good way the multiplet effects present in the e-e interaction [62].

$$\begin{aligned} u &= A + 4B + 3C, \\ u' &= A - B + C, \\ j &= \frac{5}{2}B + C. \end{aligned} \tag{3.7}$$

$$\begin{aligned} u &= F_0 + 4F_2 + 36F_4, \\ u' &= F_0 - F_2 - 9F_4, \\ j &= \frac{5}{2}F_2 + \frac{45}{2}F_4. \end{aligned} \tag{3.8}$$

Where u corresponds to the intra-orbital repulsion, u' is the inter-orbital repulsion and j the intra-atomic exchange. Finally, it is possible to define the average e-e repulsion energy U using any set of parameters, where, in this work specifically, the forms considering the normalized S-C or Racah parameters were used:

$$U = A - \frac{14}{9}B + \frac{7}{9}C, \tag{3.9}$$

or

$$U = F_0 - \frac{14}{9}F_2 - 14F_4. \tag{3.10}$$

3.1.3 Crystal Field Theory

The crystal field determines the energy states of the crystal orbitals together with their hybridization to the electronic states of nearby ions. In crystal field theory, the interaction of a local atom with its environment is given approximately by an effective potential, as can be seen in the Appendix C. This potential does not quite exist in solids, but can be seen as a description of the effective fields that depict the bounded states of an atom. The electronic states depend strongly on not just the electron-electron interaction but also in the crystal field and the hybridization of the metal's d orbitals and oxygen's $2p$ orbitals, in the case of oxides. In summary, crystal field theory allows one to find the energy eigenstates of the d orbitals of a TM, as in this case, when they are under the influence of a crystal field and a given symmetry, which is exposed in Appendix C as well. The main idea here is to solve Schrodinger's equation for the following Hamiltonian [32]:

$$\hat{H} = \hat{H}_{Atomic} + \hat{H}_{CF}. \tag{3.11}$$

The term $\hat{H}_{Atomic}$ includes the electron's kinetic energy, its interaction with the cores involved, and the Coulomb interaction on site, as explained in the atomic multiplet section. As for the term $\hat{H}_{CF}$, as stated before, it represents the interaction between electrons and the ligand fields that surround the TM also, this term is highly dependent on the symmetry of the system, since it is one of the main components to perform the calculations present in Appendix C. $\hat{H}_{CF}$ is written in terms of a general crystal field potential represented by the following equation.

$$\hat{H}_{CF} = V_{CF}(\vec{r}) = \sum_{l=0}^{\infty} \sum_{m=-l}^{l} r^l q_{lm} Y_{lm}(\theta, \phi) . \tag{3.12}$$

Where, in equation 3.12, r corresponds to the TM electron position, q_{lm} is the term with direct dependence on symmetry and $Y_{lm}(\theta, \phi)$ is a spherical harmonic originated from a Legendre polynomials expansion, with θ and ϕ being the coordinates of $\vec{r}$. In Appendix C there are extensive calculations showing how this potential can be interpreted and employed correctly in the analysis according to the symmetries studied in this work.

But what we use in practice from crystal field theory is the crystal field splitting energy that is given by parameters specific to which symmetry it is being considered. For example, in octahedral symmetry, for transition metals, the splitting is given by a parameter called $10Dq$, as it is extensively shown in Appendices C and D. But, if considering another symmetry, for example, square pyramidal, considering still transition metals, the splitting is given by a set of three parameters: Dq, Ds and Dt [62–64].

3.1.4 Cluster Model

Until now, only a portion of the theory behind this work has been presented. In order to implement this, it is possible to make use of the Cluster Model. This model is capable of including interactions such as electronic correlations or charge fluctuation that occurs when transition metal and oxygen interact with each other. Historically, the Cluster Model is applied to the cluster actually happens the effects and interactions of interest, like the regular MO_6 octahedron present in Figure 18. However, what if the material being studied is composed by more than just TM and O, like a single perovskite, similar to the one presented in Chapter 1 ($LaMnO_3$)? In this case, we are still analyzing the MO_6 cluster and the rare-earth has as main task to establish the oxidation state of the transition metal, in the case of the mentioned perovskite, the lanthanum ensures that the manganese ion will be $3+$.

This analysis encompasses the three oxygen p orbitals (p_x, p_y, p_z) surrounding the metal, as well as the five TM d orbitals $(d_{xy}, d_{xz}, d_{yz}, d_{z^2}, d_{x^2-y^2})$, culminating in a total of 23 orbitals. The p orbitals are described through a linear combination of atomic orbitals, yielding in six molecular orbitals that exhibit $A_{1g}, T_{1g}, T_{2u}, T_{1u}, T_{2g}$ and E_g symmetries [65, 66], as it is showcased in Appendices C and D. However, it is worth noting that only two of these symmetries interact with the TM ions, T_{2g} and E_g, as elucidated in Appendix D. This distinction gives rise to "four" symmetries characterized by mixed TM and oxygen contributions, categorized into bonding (predominantly $2p$ character) and anti-bonding (predominantly TM d character) molecular orbitals bearing T_{2g} and E_g

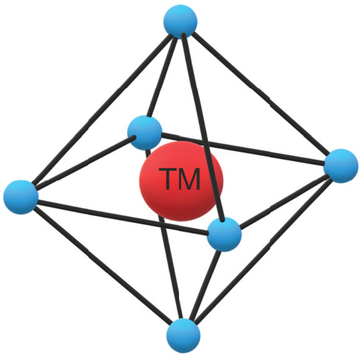

Figure 18 – Octahedral cluster used to picture the main idea of the cluster model.

symmetries [65]. While the model explicitly includes these four symmetries, it is crucial to acknowledge that all other orbitals exclusively featuring oxygen $2p$ character can be effectively addressed using the independent particles approximation. This framework is visually represented in Figure 19:

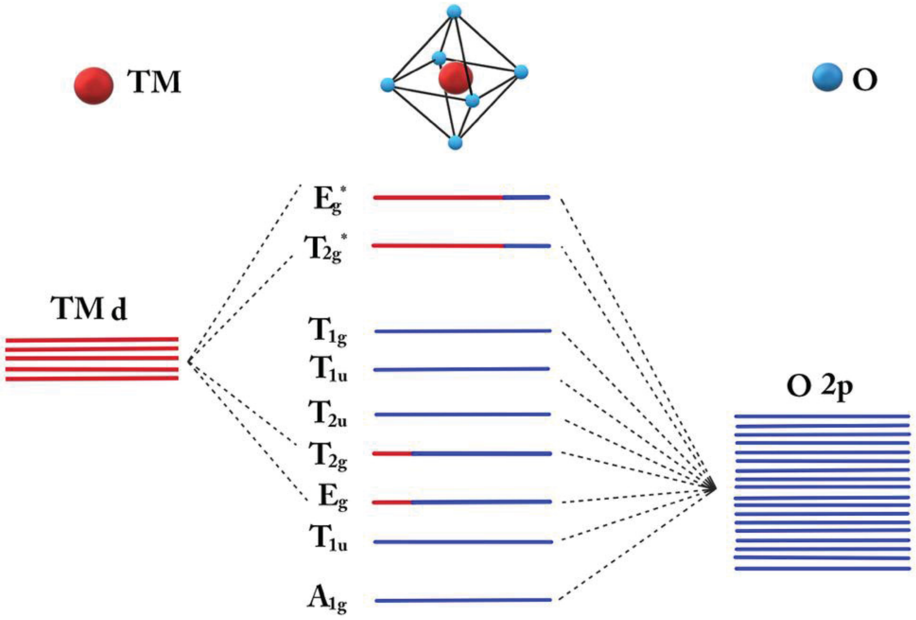

Figure 19 – Diagram illustrating the emergence of molecular orbitals resulting from the interaction between $TM\ d$ and $O\ 2p$ orbitals within a TMO_6 octahedron. In particular, it presents orbitals characterized by T_{2g} and E_g symmetries, exemplifying the interplay between $TM\ d$ and $O\ 2p$ character in these selected orbitals.

The break of degeneracy within the $TM\ d$ orbitals into only T_{2g} and E_g symmetries originates from the consideration of specific symmetries, primarily driven by the influence of crystal field effects. A simplified analysis of this phenomenon can be seen from the interaction between the $5\ d$ orbitals of the TM and the $3\ p$ oxygen orbitals, as illustrated in Figure 20.

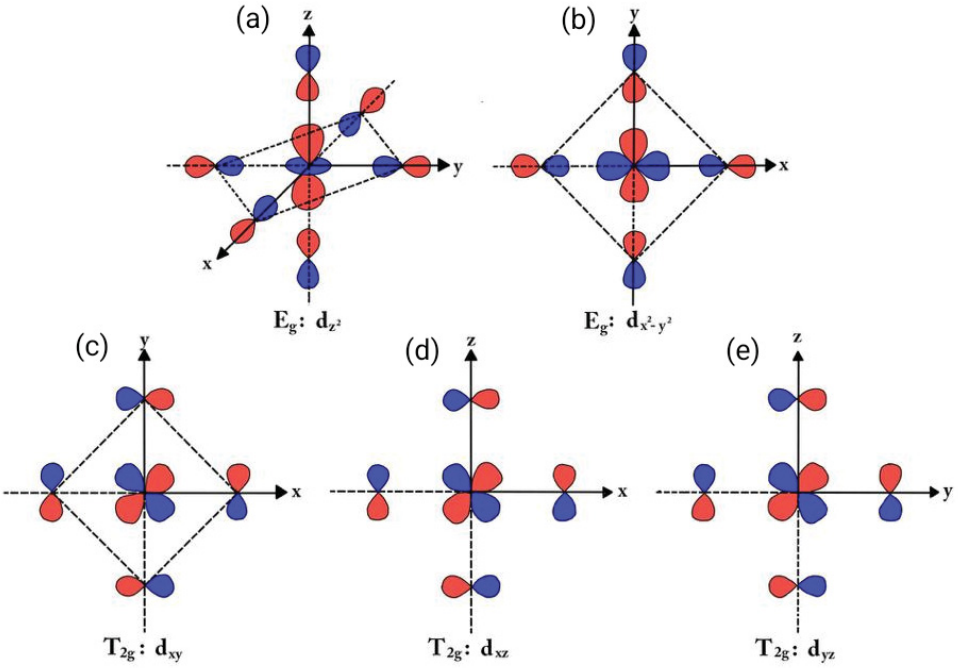

Figure 20 – Scheme depicting the origin of the bonding molecular orbitals T_{2g} and E_g, elucidating which kind of bonding is formed by each orbital. (a)-(b) Orbitals aligned directly to oxygen orbitals assume the σ-character and are related to the E_g symmetry. (c)-(d)-(e) On the other hand, orbitals aligned between oxygen p orbitals have π-character and are related to the T_{2g} symmetry.

In particular, orbitals bearing E_g symmetry, namely $d_{x^2-y^2}$ and d_{z^2}, align themselves with the direction of oxygen orbitals, thus assuming a σ character. On the contrary, orbitals characterized by T_{2g} symmetry, specifically $d_{xy}, d_{xz},$ and d_{yz}, direct themselves between oxygen p orbitals, resulting in a π character, as depicted in Figure 20. Furthermore, it is essential to emphasize that each orbital that contributes to the E_g symmetry experiences an increase in energy of $+6Dq$, while those that contribute to T_{2g} exhibit a decrease of $-4Dq$. Consequently, there exists a substantial energy difference of $10Dq$ between the two states, a phenomenon known as crystal field unfolding, which can be better visualized with the calculations present in Appendices C and D. But a diagram illustrating this splitting is presented in Figure 21.

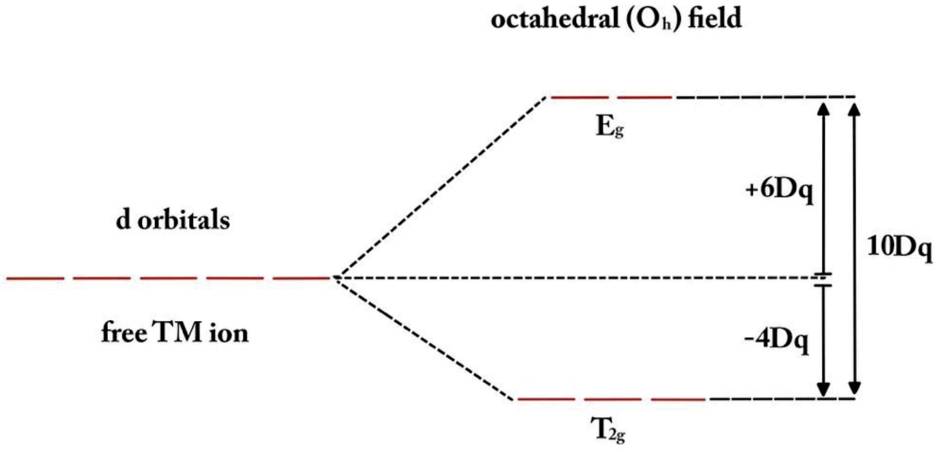

Figure 21 – Diagram that visually represents the crystal field unfolding within the d level of transition metals in octahedral symmetry.

The cluster model has long served as a tool for gaining deeper insight into experimental spectra. Additionally, it has proven to be highly effective in clarifying electronic correlations within the studied systems. Historically [67], the simple cluster model has been used for only one octahedron of the form MO_6. This model is elegantly described through a model Hamiltonian, making use of Second Quantization techniques to represent its core principles.

$$\begin{split}\hat{H}_{cluster} = \sum_{i,\sigma} \epsilon^d_{i,\sigma}\hat{d}^\dagger_{i,\sigma}\hat{d}_{i,\sigma} + \sum_{i,\sigma}\epsilon^p_{i,\sigma}\hat{p}^\dagger_{i,\sigma}\hat{p}_{i,\sigma} + \sum_{i,\sigma} T_i\left(\hat{d}^\dagger_{i,\sigma}\hat{p}_{i,\sigma} + \hat{p}^\dagger_{i,\sigma}\hat{d}_{i,\sigma}\right) \\ + \sum_{i,i',\sigma,\sigma'}\left(U - J\delta_{\sigma,\sigma'}\right)\hat{d}^\dagger_{i,\sigma}\hat{d}_{i,\sigma}\hat{d}^\dagger_{i',\sigma'}\hat{d}_{i',\sigma'}.\end{split} \tag{3.13}$$

In this equation, the indices i and σ represent the orbital index and spin component, respectively. The operators $\hat{d}^\dagger_{i,\sigma}$ and $\hat{d}_{i,\sigma}$ create and annihilate d electrons with energies $\epsilon^d_{i,\sigma}$, while $\hat{p}^\dagger_{i,\sigma}$ and $\hat{p}_{i,\sigma}$ do the same for p electrons with energies $\epsilon^p_{i,\sigma}$. The first term in the Hamiltonian accounts for the number of d electrons with energy $\epsilon^d_{i,\sigma}$, and the second term represents the number of p electrons with energy $\epsilon^p_{i,\sigma}$. The third term describes the hybridization between TM d and O $2p$ orbitals, denoted by T_i. This hybridization depends only on the symmetries T_{2g} and E_g and is computed accordingly. Hybridization terms can be written as T_σ and T_π, which are characterized as renormalizations of the Slater-Koster two-center integrals [68], $pd\sigma$ and $pd\pi$, and can be expressed as:

$$T_\sigma = \sqrt{3}\,pd\sigma, \tag{3.14}$$

$$T_\pi = 2\,pd\pi, \tag{3.15}$$

$$T_\pi \approx -\frac{1}{2}T_\sigma. \tag{3.16}$$

The last term in the Hamiltonian accounts for the number of electron pairs in the d band, adding a Coulomb repulsion energy U to each pair and subtracting J (intra-atomic exchange energy) for each pair of electrons with aligned spins. Now, it is necessary to know how to implement this.

3.2 Basis

Up to this point, our discussion has focused on atomic and crystal field effects. The next step is to understand how to effectively describe the system under study, integrating covalence into our model. To do that, the configuration interaction method enters the scene, as is presented in the following.

3.2.1 Configuration Interaction Method

To accurately account for charge transfer effects, the cluster model can be solved by employing the Configuration Interaction (CI) method [28, 29, 69]. This method involves expanding the ground state wave function beyond the ionic approximation, allowing for the possibility of electron transfer between the ligand oxygen and the transition metal. To illustrate this, consider a configuration beyond the ionic state in which an $O\ 2p$ electron transitions to a t_{2g} or e_g orbital of the TM. This transition gives rise to the $\left|d^{n+k}\underline{L}^k\right\rangle$ state, where k can assume values of 1, 2, and so on, while maintaining octahedral symmetry. As an illustrative example, let us examine the GS wave function for the $|d^6\rangle$ state:

$$|\Psi_{GS}\rangle = \alpha\left|d^6\right\rangle + \beta\left|d^7\underline{L}\right\rangle + \gamma\left|d^8\underline{L}^2\right\rangle + \delta\left|d^9\underline{L}^3\right\rangle + \epsilon\left|d^{10}\underline{L}^4\right\rangle, \tag{3.17}$$

where, $\underline{L}$ denotes a hole in the $O\ 2p$ band. In addition to representing the GS wave function, $|\Psi_{GS}\rangle$ is considered as the basis that describes the system being studied. Since one of the objectives of this work is to analyze the covalence influence, the way used to include this effect is to expand the basis, including new electronic configurations (ECs) until reaching the desired outcome or stop point. For example, if it is only considered 1 electronic configuration, the corresponding basis would be represented only by $\alpha\,|d^6\rangle$, which corresponds to the ionic state where there is no interaction between TM and O. If the number of electronic configurations is augmented, the basis will be expanded considering the corresponding new states that describe the system. For example, if there are 3 ECs, the basis will correspond to $\alpha\,|d^6\rangle + \beta\,|d^7\underline{L}\rangle + \gamma\left|d^8\underline{L}^2\right\rangle$. It is possible to add as many ECs as necessary to achieve the desired end, which in the case of this work is the convergence of the Ground State energy of each material studied.

Finally, the essential parameters [70] of the model can be expressed as follows: the Coulomb repulsion energy U; the charge transfer energy Δ required to transfer one electron from the $O\ 2p$ orbital to an orbital with the same symmetry of the TM; the matrix element of hybridization T_i between p and d electrons. All of these are defined as [71]:

$$U = E\left(d^{n+1}\right) + E\left(d^{n-1}\right) - 2E\left(d^{n}\right), \tag{3.18}$$

$$\Delta = E\left(d^{n+1}\underline{L}\right) - E\left(d^{n}\right) = \epsilon^{d}_{i,\sigma} - \epsilon^{p}_{i,\sigma} + nU, \tag{3.19}$$

$$T_i = \frac{1}{\sqrt{N_i - n}} \left\langle d^{n}_{i} \right| \hat{H}_{cluster} \left| d^{n+1}_{i}\underline{L}_i \right\rangle . \tag{3.20}$$

In these expressions, $E(\zeta)$ represents the energy associated with the configuration ζ, ϵ^d and ϵ^p denote the energies present in the Hamiltonian 3.13, and N_i represents the total number of electrons residing in the i orbital. With all the "ingredients", the only thing lacking is how to implement them computationally.

3.3 Implementation

To implement the cluster model in this work, extensive calculations were required using computational implementation. There are two main programs used in this process; the first was used to obtain results regarding X-ray absorption spectroscopy of the $2p$-edge of the compounds explored in the next chapter, and the second program takes care of the oxygen $1s$-edge of the systems studied. In this chapter, there will be an overview on how the programs work. More details on how some key features were implemented, such as specific ways to account for covalence and symmetry effects, are presented in Appendix E.

3.3.1 Programs used

The first program employed is *Quanty* [57], a Lua-based script language that enables users to address quantum mechanical problems using second quantization. It supports various applications, such as quantum chemistry such as post-Hartree-Fock, LDA^{++} schemes by implementing self-consistent fields, configuration interaction, coupled cluster, and more [72–77]. Therefore, *Quanty* is a very powerful tool, since it is possible to include the full multiplet effects in the calculations made with it, obtaining results that can very much resemble what really happens in the experiments and, with that, achieve very accurate representations of the experimental results. To perform accurate calculations with *Quanty*, fundamental components must be considered. Exemplifications of how they are written in the code are given in Appendix E. The second program employed to implement the cluster model in this thesis has developed using *MATLAB* [78]. Although not as intricate as *Quanty*, the code is robust, providing valuable results, particularly by incorporating covalence effects, despite its current state lacking full multiplet effects.

3.3.2 Parameters

Before proceeding, it is necessary to know the parameters used to obtain the results presented in this thesis. Tables 1 and 2 present the parameters used in the cluster model calculations for the $TM\ 2p$ and $O\ 1s$ edges, respectively. These values were obtained by theoretical reproduction of experimental spectra retrieved from the literature. Originally, they were retrieved from a list of references [37, 39, 41, 64, 65, 71, 79–82], but as the simulations were performed, some adjustments had to be made to correctly reproduce the experiments, as will be seen in Chapter 5. More precisely, the average e-e repulsion energy, crystal field, charge transfer energy, and hybridization parameters were adjusted accordingly to the necessary. The indices (I) and (F) are related to the ground and excited states, since it is possible to separate them in the codes, as was shown previously. Each set of parameters is connected to its rightful transition metal, where it is indicated which material had its experimental data reproduced. In particular, the Slater-Condon parameters ($F^2_{(p/d)d}$, $F^4_{(p/d)d}$, G^1_{pd} and G^3_{pd}) present in Table 1 are in their original form, but, to perform the calculations, they were reduced to 80% of their atomic values to account for inherent charge screening effects, as mentioned in earlier sections. In the case of Table 2, there is the presence of the Racah parameter (B and C), which were also reduced by 80% and it is worth noting the absence of spin-orbit coupling parameters in this table, because of the fact that, in this case, it was not possible to account for the full multiplet effects due to the nature of the code utilized.

Analyzing the values of the parameters in Tables 1 and 2, it is possible to see that all compounds except CoO are in the charge transfer regime ($\Delta < U$), while this exception is in the Mott-Hubbard regime ($\Delta > U$) [52], as explained in Chapter 2.4. Furthermore, high values of $pd\sigma$ indicate strong covalence between $TM\ 3d$ - $O\ 2p$, which is consistent with the results presented. The final step before presenting the results obtained is to present the systems used and their interesting characteristics.

$L_{2,3} - edge\ XAS$	U_{dd}	$F^2_{dd}(I)$	$F^4_{dd}(I)$	$F^2_{dd}(F)$	$F^4_{dd}(F)$	$F^2_{pd}(F)$	$G^1_{pd}(F)$	$G^3_{pd}(F)$	$\zeta_d(I)$	$\zeta_d(F)$	$\zeta_p(F)$	$10Dq$	Ds	Ds_∞	Dt	β	Δ	$pd\sigma$
V^{5+} (V_2O_5)	5.500	0.0000	0.000	0.0000	0.000	7.460	5.661	3.226	0.000	0.047	4.652	0.900	0.200	——	0.040	——	0.700	2.7000
Mn^{2+} (MnO)	7.000	10.316	6.413	11.155	6.943	6.321	4.604	2.617	0.040	0.053	6.847	0.600	——	——	——	——	6.500	-1.0970
Mn^{3+} $(LaMnO_3)$	7.500	11.415	7.148	12.210	7.649	6.988	5.176	2.944	0.046	0.059	6.846	0.800	——	——	——	——	4.500	-1.7898
Mn^{4+} $(SrMnO_3)$	7.800	12.416	7.820	13.177	8.300	7.657	5.774	3.287	0.052	0.066	6.846	1.800	——	——	——	——	2.000	-1.5011
Fe^{2+} (FeO)	7.000	10.966	6.815	11.780	7.328	6.793	5.001	2.844	0.052	0.067	8.201	1.300	——	——	——	——	6.000	-1.0970
Fe^{3+} $(LaFeO_3)$	7.500	12.043	7.535	12.819	8.024	7.446	5.564	3.165	0.059	0.074	8.200	1.200	——	——	——	——	2.500	-1.3856
Fe^{4+} $(SrFeO_3)$	7.800	13.030	8.198	13.777	8.668	8.102	6.151	3.502	0.066	0.082	8.200	0.900	——	——	——	——	0.000	-1.3279
Co^{2+} (CoO)	5.300	11.605	7.210	12.396	7.708	7.260	5.394	3.068	0.066	0.083	12.249	2.100	——	——	——	——	5.500	-1.3279
Co^{3+} $(LiCoO_2)$	5.500	12.664	7.917	13.422	8.395	7.899	5.948	3.385	0.074	0.092	9.747	1.200	——	——	——	——	2.000	-1.6743
Co^{4+} $(SrCoO_3)$	7.500	13.640	8.573	14.373	9.035	8.545	6.526	3.716	0.082	0.101	9.147	1.000	——	——	——	——	-2.000	1.1547
Mn^{3+} $(Sr_2Mn_{0.7}Mo_{0.3}O_3)$	7.500	11.415	7.148	12.210	7.649	6.988	5.176	2.944	0.046	0.059	6.846	0.800	——	0.254	——	1.105	4.500	-1.7898
V^{5+} (V_2O_5)	5.500	0.0000	0.000	0.0000	0.000	7.460	5.661	3.226	0.000	0.047	4.652	0.900	0.200	——	0.040	——	0.700	2.7000

Table 1 – Parameters utilized to calculate the $TM\ 2p$-edge XAS of each compound studied. All values are presented in eV, except by the distortion parameter β, which is dimensionless.

$O\ K-edge\ XAS$	U_{dd}	$B(I)$	$C(I)$	$B(F)$	$C(F)$	$10Dq$	Ds	Ds_{∞}	Dt	β	Δ	$pd\sigma$
$Mn^{2+}\ (MnO)$	7.000	0.1378	0.5090	0.1489	0.5510	0.600	———	———	———	———	6.500	-1.0970
$Mn^{3+}\ (Mn_2O_3)$	7.500	0.1519	0.5673	0.1625	0.6071	0.800	———	———	———	———	4.500	-1.7898
$Mn^{4+}\ (SrMnO_3)$	7.800	0.1647	0.6206	0.1748	0.6587	1.800	———	———	———	———	2.000	-1.5011
$Fe^{2+}\ (FeO)$	7.000	0.1465	0.5409	0.1573	0.5816	1.000	———	———	———	———	6.000	-1.0970
$Fe^{3+}\ (LaFeO_3)$	7.500	0.1603	0.5980	0.1706	0.6368	1.200	———	———	———	———	2.500	-1.3856
$Fe^{4+}\ (SrFeO_3)$	7.800	0.1730	0.6506	0.1829	0.6879	0.900	———	———	———	———	0.000	-1.3279
$Co^{2+}\ (CoO)$	5.300	0.1551	0.5722	0.1656	0.6117	2.100	———	———	———	———	5.500	-1.3279
$Co^{3+}\ (LiCoO_2)$	5.500	0.1687	0.6283	0.1787	0.6663	1.200	———	———	———	———	2.000	-1.6743
$Co^{4+}\ (SrCoO_3)$	7.500	0.1812	0.6804	0.1909	0.7171	1.000	———	———	———	———	-2.000	1.1547
$Mn^{3+}\ (Sr_2Mn_{0.7}Mo_{0.3}O_3)$	7.500	0.1519	0.5673	0.1625	0.6071	0.800	———	0.254	———	1.105	4.500	-1.7898
$V^{5+}\ (V_2O_5)$	5.500	0.0000	0.0000	0.0000	0.0000	0.900	0.200	———	0.040	———	0.700	2.7000

Table 2 – Parameters utilized to calculate the $O\ 1s$-edge XAS of each compound studied. All values are presented in eV, except for the distortion parameter β, which is dimensionless.

CHAPTER 4

Studied Systems

This chapter provides a brief exploration of the physical properties exhibited by the compounds chosen for this study. Given that one of the focal points of this research is to analyze the symmetries exhibited by each material, this chapter separates them based on their specific symmetry properties. For each symmetry group, in addition to the general overview of their physical characteristics, the materials can present many different and very interesting properties, but here we will only give a brief overview of the most notorious ones for each TMO, serving also as a motivation for this research.

4.1 Octahedral (O_h) symmetry

4.1.1 Manganese - *Mn*

Manganese displays a wide range of valence states, spanning from $3d^5$ $(2+)$ to $3d^0$ $(7+)$. This study, however, concentrates on valence states within the range from $2+$ to $4+$. Starting with MnO, where the manganese ion has a nominal valence of $2+$ and can be visually represented by Figure 22.

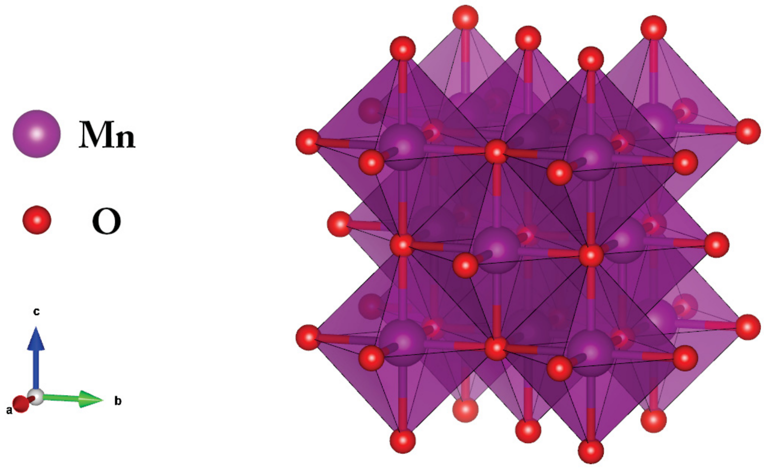

Figure 22 – Crystalline structure of the material MnO, where the manganese ion has an oxidation state of $2+$ and presents the octahedral symmetry. This is a cubic rocksalt crystal structure and is characterized by the space group $Fm\overline{3}m$. Figure made using the *Vesta* software [83].

MnO is a halide with a rocksalt crystal structure and crystallizes in the cubic $Fm\overline{3}m$ space group [84]. Notably, this compound exhibits a strong ionic character [4, 70]. MnO exhibits antiferromagnetic ordering [85], and Mn^{2+} ion presents a high-spin state with a ground state configuration given by $t^3_{2g\uparrow}e^2_{g\uparrow}$ [71]. There is a brief discussion in Appendix E about what a high or low-spin state is.

In the case of the $3+$ valence state, two materials were considered, one for the TM $2p$-$edge$ XAS and another for the O K-$edge$ XAS, namely $LaMnO_3$ and Mn_2O_3, respectively. Starting with the lanthanum perovskite, $LaMnO_3$ presented in Figure 23. This material adopts an orthorhombic crystal structure with the space group $Pnma$ [84, 86, 87]. The orthorhombic distortion arises due to the electron configuration of the Mn atom ($t^3_{2g\uparrow}e_{g\uparrow}$ in a high-spin state), leading to a symmetry-breaking effect, while the Mn^{3+} ions retain an octahedral-like structure [86, 88]. $LaMnO_3$ exhibits characteristics of an A-type antiferromagnetic insulator, [70, 86, 89].

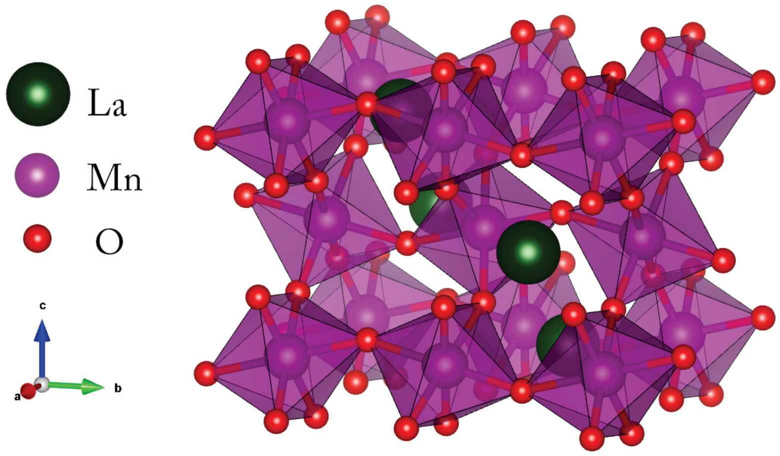

Figure 23 – Crystalline structure of the material $LaMnO_3$, where the manganese ion has an oxidation state of $3+$ and presents the octahedral symmetry. This is an orthorhombic crystal structure and is characterized by the space group $Pnma$. Figure made using the *Vesta* software [83].

Now, for the second material considered for the Mn^{3+} ion, manganese trioxide (Mn_2O_3), which can be seen in Figure 24.

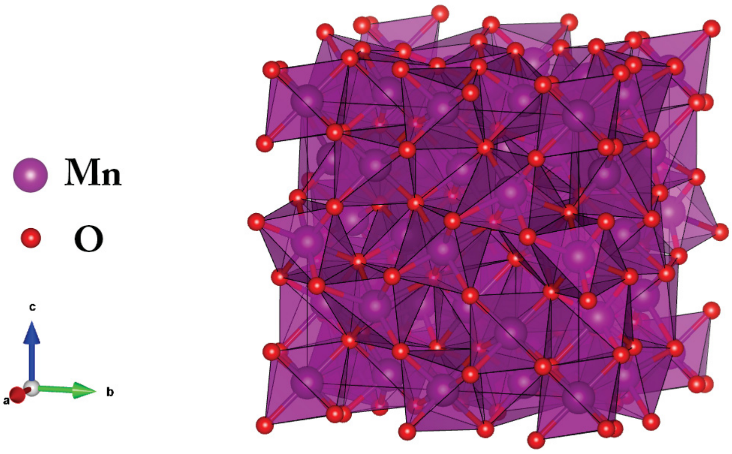

Figure 24 – Crystalline structure of the material Mn_2O_3, where the manganese ion has an oxidation state of $3+$ and presents the octahedral symmetry. This is a cubic bixbite crystal structure and is characterized by the space group $Ia\overline{3}$. Figure made using the *Vesta* software [83].

Mn_2O_3 is stabilized in the body-centered cubic bixbite phase, characterized by the space group $Ia\overline{3}$ [90, 91]. It undergoes a ferromagnetic transition at $43\ K$ and shifts to an antiferromagnetic state at approximately $80\ K$ [90, 92]. Furthermore, Mn_2O_3 exhibits a valence band configuration of $3d^4$ with a high-spin state ($t^3_{2g\uparrow}e_{g\uparrow}$) [4, 93].

When exploring the valence state of $4+$, we turned to another perovskite compound, $SrMnO_3$. This material presents a cubic structure at high temperatures that is formed by corner-sharing MnO_6 octahedra as shown in Figure 25 [94, 95].

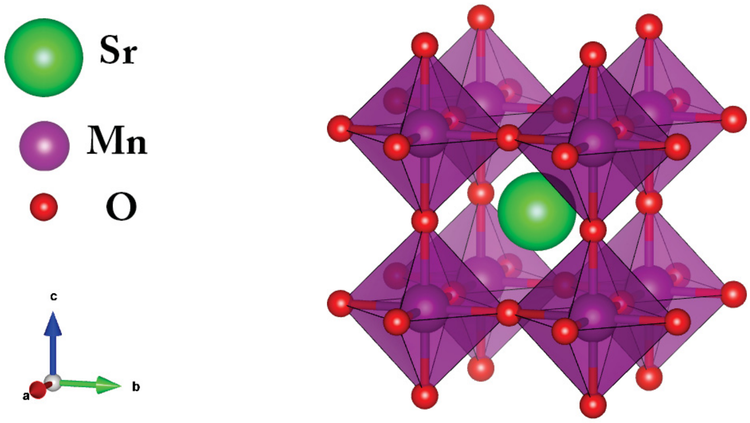

Figure 25 – Crystalline structure of the material $SrMnO_3$, where the manganese ion has an oxidation state of $4+$ and presents the octahedral symmetry. This is a cubic crystal structure, and it is characterized by the space group $Pm\overline{3}m$. Figure made using the *Vesta* software [83].

It is characterized by the space group $Pm\overline{3}m$ and features a high-spin state with a $t_{2g\uparrow}^3$ electron configuration [71, 96]. Furthermore, cubic $SrMnO_3$ exhibits the properties of a G-Type antiferromagnetic insulator [42, 94, 97, 98].

4.1.2 Iron - *Fe*

Iron oxides play a crucial role in various technological applications, such as catalysis and data storage [44, 99, 100] and have been widely studied in recent decades. Similarly to manganese, this study examines the oxidation states of iron, specifically $2+$, $3+$ and $4+$. Starting with the $2+$ oxidation state, we explore iron monoxide (FeO). FeO possesses a cubic rocksalt crystal structure, characterized by the space group $Fm\overline{3}m$ under ambient pressure [44, 101, 102], as illustrated in Figure 26.

Furthermore, FeO exhibits characteristics of an antiferromagnetic insulator [44, 101]. Its ground state is described as having a $3d^6$ configuration, which can transition between a high-spin state ($t_{2g\uparrow}^3 t_{2g\downarrow} e_{g\uparrow}^2$) and a low-spin state ($t_{2g\uparrow}^3 t_{2g\downarrow}^3$). This spin state transition is induced by a substantial increase in external pressure applied to the FeO sample, resulting in the electron transition from e_g to t_{2g} orbitals and the pairing of these d-electrons [101, 103].

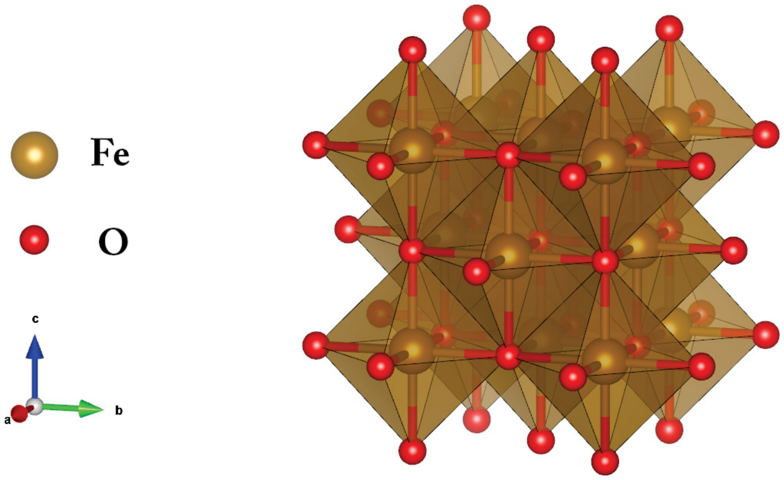

Figure 26 – Crystalline structure of the material FeO, where the iron ion has an oxidation state of $2+$ and presents the octahedral symmetry. This is a cubic rocksalt crystal structure and is characterized by the space group $Fm\overline{3}m$. Figure made using the *Vesta* software [83].

Regarding the $3+$ valence state, it was examined the lanthanum perovskite $LaFeO_3$, which is depicted in Figure 27. This material, at ambient conditions, adopts an orthorhombic crystalline structure in the space group $Pnma$ [104–106]. $LaFeO_3$ is classified as a G-type antiferromagnetic insulator perovskite [107, 108]. Also, the Fe^{3+} ion adopts a high-spin state configuration ($t^3_{2g\uparrow}e^2_{g\uparrow}$) [104].

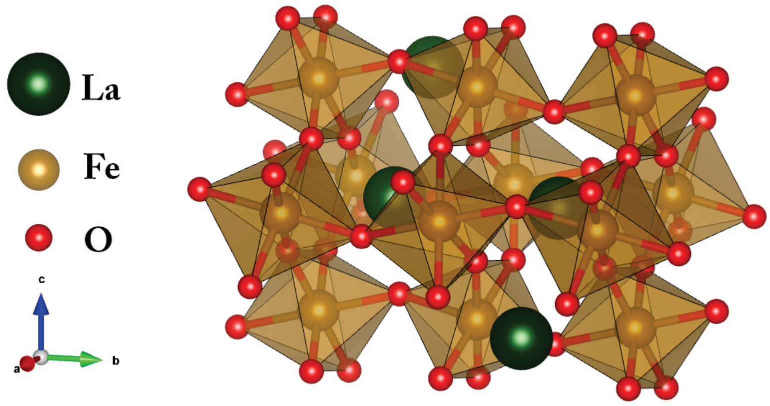

Figure 27 – Crystalline structure of the material $LaFeO_3$, where the iron ion has an oxidation state of $3+$ and presents the octahedral symmetry. This is an orthorhombic crystal structure and is characterized by the space group $Pnma$. Figure made using the *Vesta* software [83].

For the $4+$ valence state, much like in the manganese case, we examined a strontium perovskite with the chemical formula $SrFeO_3$, illustrated in Figure 28.

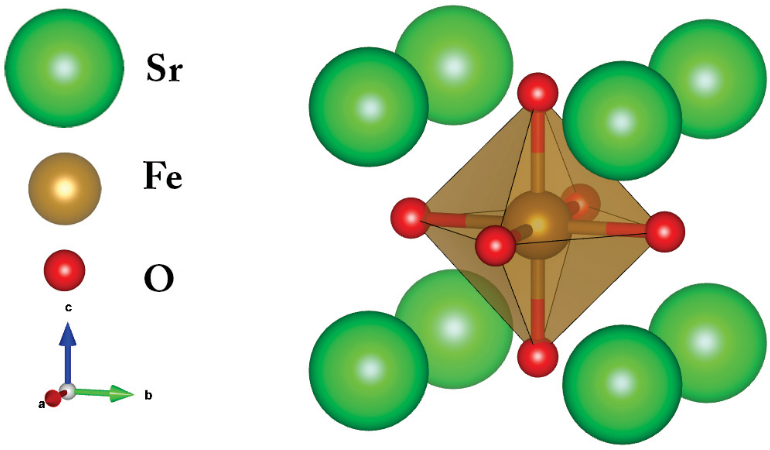

Figure 28 – Crystalline structure of the material $SrFeO_3$, where the iron ion has an oxidation state of $4+$ and presents the octahedral symmetry. This is a cubic crystal structure, and it is characterized by the space group $Pm\overline{3}m$. Figure made using the *Vesta* software [83].

The material $SrFeO_3$ assumes a cubic crystal structure with the space group $Pm\overline{3}m$ and exhibits a G-type antiferromagnetic ordering [107, 109]. $SrFeO_3$ demonstrates strong covalent bonding, and its band gap is negligible, in other words, it is closed, as was shown in Chapter 2.4. This is a clear behavior caused by the compound being in the Negative Charge Transfer regime, which means that its ground state is mostly covalent and contains considerable $O\ 2p$ hole character [41, 56]. Its ground state configuration is $3d^5$, featuring a high-spin state ($t^3_{2g\uparrow}e_{g\uparrow}$) [37].

4.1.3 Cobalt - *Co*

Cobalt oxides exhibit not only intriguing structural and physical properties but is also found in crucial applications, exemplified by the widely used compound $LiCoO_2$ in lithium battery production [110–112]. This investigation, like the previous cases, investigates the oxidation states of $2+$, $3+$, and $4+$ for cobalt.

Starting with the $2+$ valence state, represented by cobalt monoxide (CoO), this material adopts a cubic rocksalt structure with the space group $Fm\overline{3}m$ at $300\ K$ [113]. A visual representation is provided in Figure 29.

Cobalt monoxide is characterized as an antiferromagnetic material and exhibits insulating properties, specifically as a Mott insulator [114–116]. The ground state configuration of CoO is $3d^7$ with a high-spin state ($t^3_{2g\uparrow}t^3_{2g\downarrow}e_{g\uparrow}$) [71].

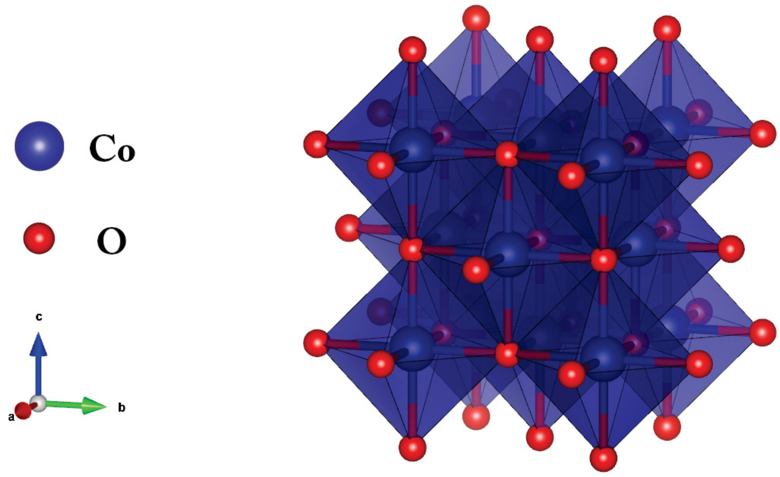

Figure 29 – Crystalline structure of the material CoO, where the cobalt ion has an oxidation state of $2+$ and presents the octahedral symmetry. This is a cubic rocksalt crystal structure and is characterized by the space group $Fm\overline{3}m$. Figure made using the *Vesta* software [83].

Moving to the $3+$ valence state, the lithium perovskite $LiCoO_2$ was investigated, displaying rhombohedral symmetry with the space group $R\overline{3}m$ [117]. Figure 30 visually represents this material.

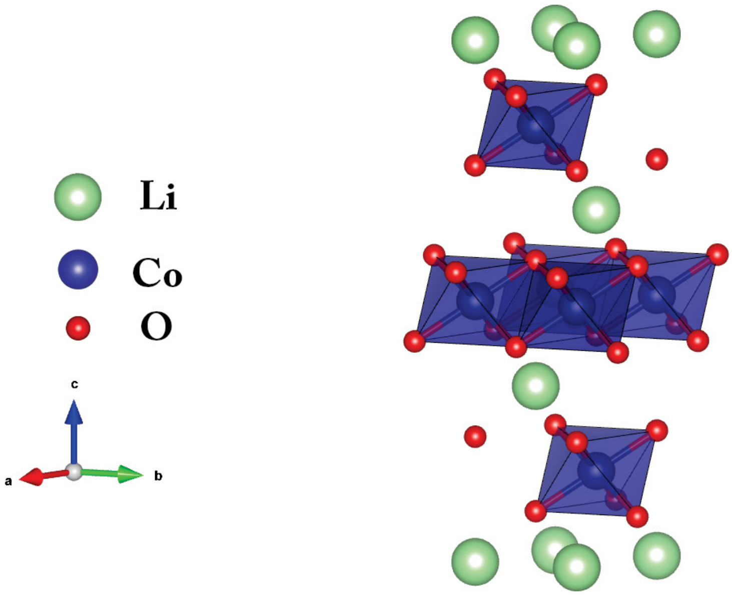

Figure 30 – Crystalline structure of the material $LiCoO_2$, where the cobalt ion has an oxidation state of $3+$ and presents the octahedral symmetry. This is a rhombohedral crystal structure and is characterized by the space group $R\overline{3}m$. Figure made using the *Vesta* software [83].

$LiCoO_2$ exhibits antiferromagnetic order. It functions as a wide gap semiconductor [117] and shares Mott insulator characteristics with cobalt in the $2+$ oxidation state [118]. Finally, $LiCoO_2$ has a strongly mixed ground state that makes it strongly covalent and, in this material, the cobalt ion presents a low-spin valence state of $3d^6$ ($t^3_{2g\uparrow}t^3_{2g\downarrow}$) [71].

Finally, the $4+$ oxidation state is explored through the strontium perovskite $SrCoO_3$, which crystallizes in a cubic structure with space group $Pm\overline{3}m$ and exhibits ferromagnetic order [41, 110, 119–121]. Figure 31 provides a visual representation of the crystal structure.

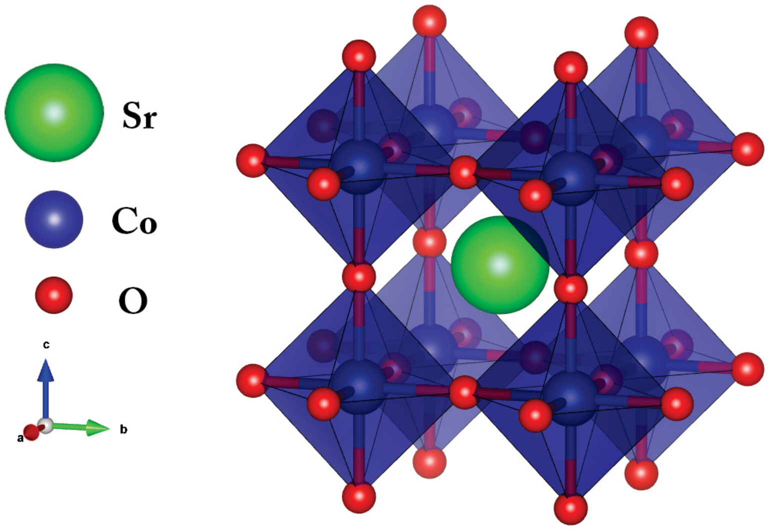

Figure 31 – Crystalline structure of the material $SrCoO_3$, where the cobalt ion has an oxidation state of $4+$ and presents the octahedral symmetry. This is a cubic crystal structure and is characterized by the space group $Pm\overline{3}m$. Figure made using the *Vesta* software [83].

$SrCoO_3$ is metallic and, similarly to $SrFeO_3$, it operates in the Negative Charge Transfer regime [41]. Although an ionic perspective suggests a high-spin or low-spin ground state for the Co^{4+} ion, experimental evidence indicates an intermediate spin state $t_{2g}^4 e_g$, which can be specifically described by a high-spin Co^{3+} state ($3d^6 : t_{2g\uparrow}^3 t_{2g\downarrow} e_{g\uparrow}^2$) with an oxygen hole $\underline{L}$ [41, 80, 110].

4.2 Tetragonal (D_{4h}) symmetry

4.2.1 *$SrMn_{0.7}Mo_{0.3}O_3$*

The compound focused in this work originates from the study of the perovskite $SrMn_{1-x}Mo_xO_3$ [42, 122], where the value of x varied from 0.0 to 0.75. In this thesis, we work only with the case where $x = 0.3$. $SrMn_{0.7}Mo_{0.3}O_3$ is a double perovskite of the type $ABB'O_3$. At room temperature, it exhibits a single-phase cubic perovskite structure with space group $Pm\overline{3}m$. As predicted in a previous study [42], this material demonstrates insulating behavior and is characterized by a high-spin state with a d^4 electron configuration. Furthermore, the manganese ion is encountered to be in the $3+$ oxidation state. A visualization of the crystalline structure of this material can be seen in Figure 32.

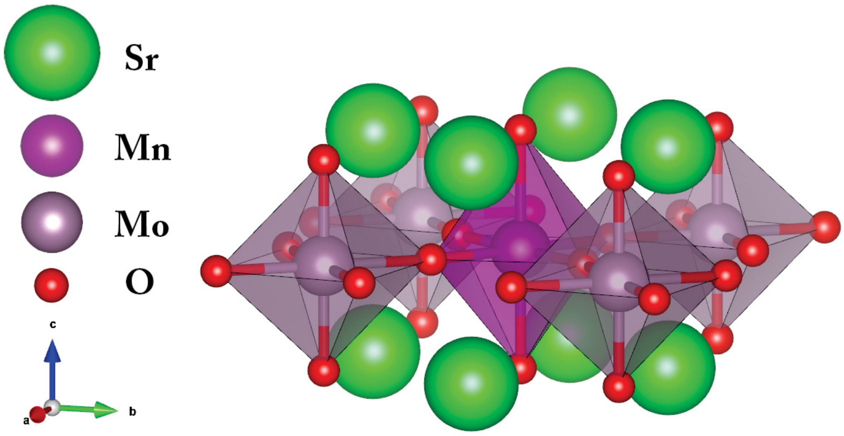

Figure 32 – Schematic of the crystalline structure of the material $SrMn_{0.7}Mo_{0.3}O_3$, where the manganese ion has an oxidation state of $3+$ and presents the tetragonal symmetry. It is possible to visualize the distorted manganese octahedral in the center of the image, which occurs only for this double perovskite in this specific molybdenum concentration. This is a single-phase cubic crystal structure and is characterized by the space group $Pm\overline{3}m$. Figure made using the *Vesta* software [83].

As mentioned above, for this study a concentration of Mo of $x = 0.3$ was chosen. In this specific case, the double perovskite exhibits a distorted octahedral behavior, giving rise to a D_{4h} symmetry, which is the interest of this work on this material. The extent of distortion is approximately 1.11 times the regular lattice distance. This distortion is attributed to the Jahn-Teller effect, which is more likely to impact a molecule of this type due to the presence of an odd number of electrons in the e_g orbital. A schematic representation of the distortion in the Mn octahedral cluster under consideration can be seen in Figure 33 [42].

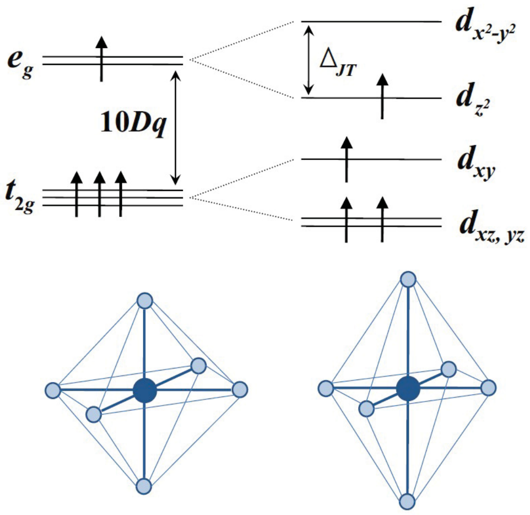

Figure 33 – Schematic illustrating the Jahn-Teller effect acting on an MnO_6 octahedron with perfect O_h symmetry (on the left) and transforming it into a distorted octahedron with D_{4h} symmetry (on the right). This distortion results in the splitting of the t_{2g} and e_g orbitals.

4.3 Square pyramidal (C_{4v}) symmetry

4.3.1 V_2O_5

V_2O_5 is a diamagnetic insulator at room temperature [123]. This material plays a crucial role in heterogeneous catalysis, with widespread applications in various chemical reactions, including partial oxidation reactions and selective reduction of NO$_x$ [123]. In its crystalline form, V_2O_5 adopts an orthorhombic structure with the space group $Pmmn$ [64, 123–125]. The ground state of V_2O_5 exhibits a pronounced covalent character, predominantly manifesting the $3d^1\underline{L}$ ($^1A_1$) configuration, where $\underline{L}$ represents a ligand hole.

Transition metal oxides typically consist of BO_6 blocks with octahedral local symmetry. However, many of these compounds exhibit distortions within their octahedral units. V_2O_5 is a notable example, as the VO_6 block in this material deviates significantly from the octahedral symmetry, resulting in a strongly distorted octahedra. This distortion is especially evident in the elongation of one of the apical oxygen ions, leading to a notably weakened $V-O$ interaction, as visually depicted in Figure 34.

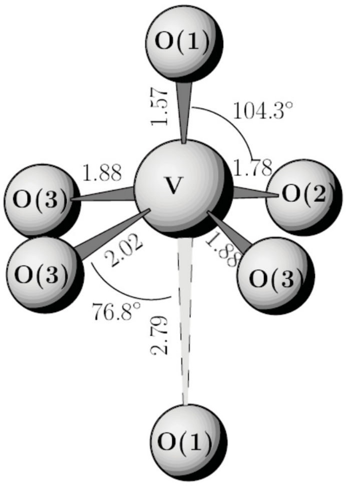

Figure 34 – Illustration of the strongly distorted octahedral structure around the V ion of V_2O_5, showing why it is possible to consider it as a square pyramid in C_{4v} symmetry [123].

Hence, a more appropriate description of the compound utilizes a VO_5 square-based pyramid as a fundamental block cell, allowing characterizing V_2O_5 with C_{4v} symmetry, as shown in Figure 35 [126]. The resulting reduction in symmetry leads to distinct energy level splitting in the crystal field, as visually demonstrated in Figure 36.

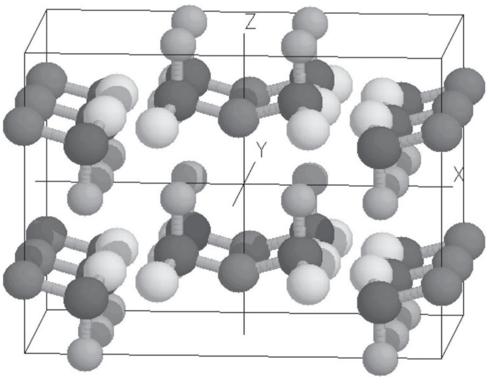

Figure 35 – Schematic of the crystalline structure of the material V_2O_5, where the vanadium atoms are the black ones and oxygen atoms are the light, medium and dark gray [126]. The vanadium ion has an oxidation state of $5+$ and presents a square pyramidal symmetry. This is an orthorhombic crystal structure and is characterized by the space group $Pmmn$.

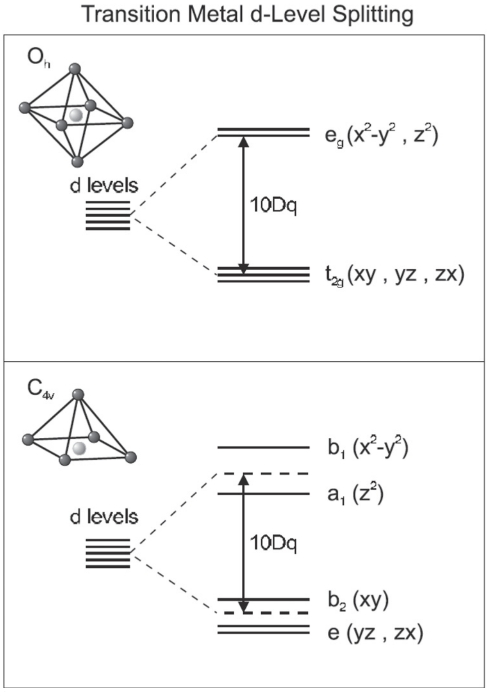

Figure 36 – Splitting of the transition metal d levels in O_h and C_{4v} symmetries [64].

Now that all systems studied, the necessary theory, and the basics of computation implementation are presented, it is time to showcase the results obtained for this thesis.

CHAPTER 5

Results

This chapter unveils the theoretical findings and conducts a meticulous experimental comparison to substantiate the central theme of this study: the potential impact of covalence and symmetry lowering effects on X-ray absorption spectroscopy (XAS). It is structured into two main sections, delineating the TM $L_{2,3}$-edge XAS results and the O K-edge XAS results, respectively. A similar organization of the results regarding each TM studied mirroring the preceding chapter is also employed.

The chapter features two types of results:

1. Comparison with experimental data extracted from the literature [37–42, 64, 127–131], offering a visual representation of how the identified effects can influence the targeted technique;
2. Theoretical results derived solely from the executed calculations, encompassing ground state and theoretical spectra data obtained for each TM studied.

5.1 *TMs* $L_{2,3}$-edge X-ray absorption spectroscopy

This section delves into the outcomes obtained regarding the $L_{2,3}$ or $2p$ edge of the transition metal oxides studied. This analysis not only encompasses covalence effects, but also takes into account various symmetries inherent in the system. The spectra presented here are classified into L_3 $(2p_{3/2})$ and L_2 $(2p_{1/2})$ regions, due to the influence of the $2p$ core-hole spin-orbit coupling effects [51]. To conclude, a thorough examination of the ground state of each system is conducted to perform a more robust analysis about the effects studied by this thesis.

The calculations were carried out with the parameters outlined in Table 1 of Chapter 3, employing the numerical convergence of the ground state energy as the convergence criterion used to obtain the theoretical data. This criterion will be discussed and explained in more detail in subsequent sections. This approach was adopted under the assumption that given the consistency of these parameters, any change in values would be correspondingly manifest in the spectra. Such constancy is demonstrated throughout this chapter. The calculated spectra incorporate a Gaussian broadening of $0.1\ eV$ to ensure a comprehensive visualization of all peaks associated with potential final states, facilitating an analysis of spectrum evolution with increasing covalence between transition metal and oxygen. Along with it, it was considered a Lorentzian lifetime broadening of $\Gamma = 0.2\ eV$ ($2p_{1/2}$ region) and $\Gamma = 0.4\ eV$ ($2p_{3/2}$ region).

5.1.1 Experimental comparison

Let us start with results that take into account the transition metal oxides that manifest the octahedral symmetry. Figures 37–39 present a comparative analysis between calculated and experimental spectra for manganese, iron, and cobalt. The experimental data, obtained from various references [37–41, 127, 128], were plotted within the original energy range and normalized intensity. Calculations for these comparisons utilize the methodology previously outlined, with a rightward rigid shift applied to align theoretical with experimental spectra. The graphs display two theoretical spectra, along with their corresponding experimental spectra, for each oxidation state of the transition metals studied in this work. The materials considered for the experimental data are indicated in each graph. The theoretical results consist of the first electronic configuration that corresponds to the ionic state (as explained in Chapter 3.2), described by $|\Psi_I\rangle = \alpha\,|d^n\rangle$. In this case there is no interaction between TM and O and, as a consequence, no presence of covalence (depicted by the blue lines), and the electronic configuration at which convergence was achieved for both ground state results (discussed in the next section). The second theoretical data is described by the consideration of a, let us say, full basis. In this case, the maximum number of ECs is included until achieving the convergence mentioned. These simulated spectra are denominated, respectively, as ionic and fully-converged spectra, with the latter being considered to be more accurate in replicating the experimental spectra.

The first comparison between theoretical and experimental spectra is related to the manganese series [37, 38, 127] and is illustrated in Figure 37. The materials considered are MnO, $LaMnO_3$, and $SrMnO_3$, representing the oxidation states $2+$,

$3+$, and $4+$ of the manganese ion, respectively. The first thing to notice in Figure 37 is the big evolution of the spectral shape when comparing ionic (blue) and fully-converged (red) spectra in all three cases. This is more discernible and pronounced in the higher oxidation state of manganese (Mn^{4+}) where not only there is a greater difference between theoretical data but also a greater displacement of the relative to the energy axis, almost $1\ eV$ from the ionic to the converged one. This difference can be explained by the interactions that each spectrum takes into account. The ionic ones are purely TM spectra, containing only atomic interactions (exchange and Coulomb), spin-orbit coupling and crystal field effects. For the converged ones, the covalence is introduced into the calculations where, by definition (fully converged $\rightarrow$ accounts for the full multiplet effects), the covalence is included. Here, charge transfer and hybridization between TM and O are present. A notable agreement is evident between the calculated and experimental spectra for all three cases. The structures in both L_3 ($2p_{3/2}$) (between $640\ eV$ and $647\ eV$) and L_2 ($2p_{1/2}$) (between $650\ eV$ and $656\ eV$) peaks align with those observed in the experimental data. The separation between (around $649\ eV$) peaks induced by spin-orbit coupling is accurately replicated in the calculations, even in the more covalent case of Mn^{4+}, and the more subtle structures present in all experimental data are well captured by the theoretical results. There is a discernible trend in manganese, indicating an increase in the number of electronic configurations for a more accurate representation of the experimental data (5, 6, and 6 ECs, respectively) as the oxidation state increases. This trend reinforces the significance of the covalence effects previously discussed in the analysis of the results.

Figure 38 presents the comparison between theoretical and experimental data [37, 128] for the iron series. The materials considered are FeO, $LaFeO_3$ and $SrFeO_3$, formally corresponding to the nominal valences $2+$, $3+$, and $4+$ of iron. Like in the manganese case, the evolution of the spectral shape is similarly present here, including the more pronounced displacement to the left of the theoretical spectra (by around $1\ eV$) related to the energy axis from the ionic to the converged spectrum. In this case, there is good agreement between theoretical and experimental spectra in all three cases studied. The structures present in both $2p_{3/2}$ (between $706\ eV$ and $714\ eV$) and $2p_{1/2}$ (between $718\ eV$ and $726\ eV$) regions, along with the spin-orbit separation (around $718\ eV$) are well reproduced. Again, the trend of increasing the covalence between TM and O is observed, where the number of electronic configurations to achieve the converged (4, 5 and 6 ECs) spectra increases as the oxidation state of iron is also increased.

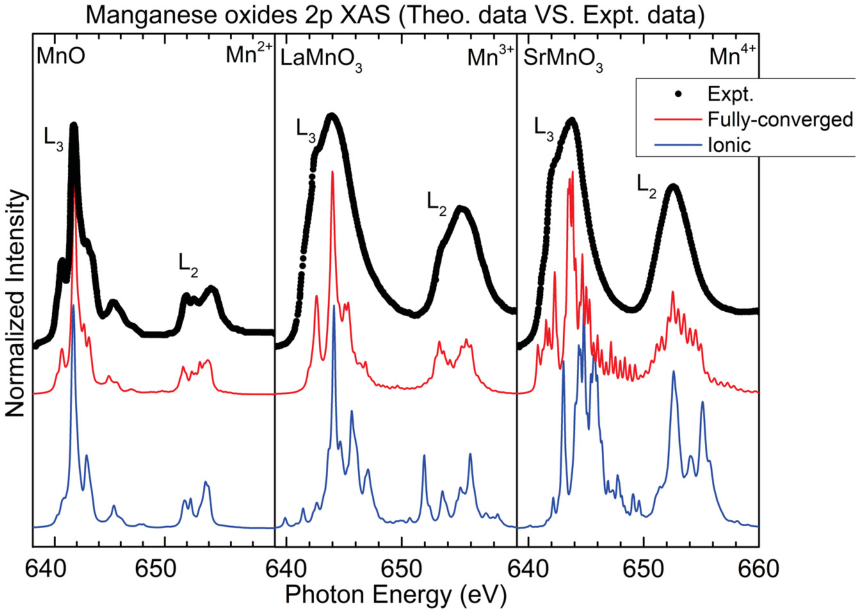

Figure 37 – Comparison of calculated and experimental X-ray absorption spectra for the manganese series (Mn^{2+}, Mn^{3+}, and Mn^{4+}). Experimental data were collected from MnO [127], $LaMnO_3$ [37], and $SrMnO_3$ [38] representing the oxidation states $2+$, $3+$, and $4+$ of manganese.

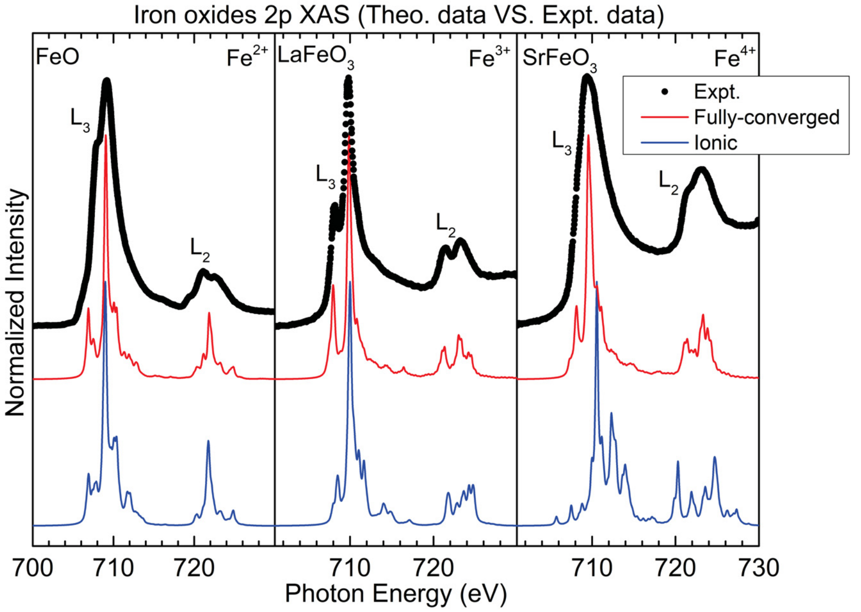

Figure 38 – Comparison of calculated and experimental X-ray absorption spectra for the iron series (Fe^{2+}, Fe^{3+}, and Fe^{4+}). Experimental data were obtained from FeO [128], $LaFeO_3$ [37], and $SrFeO_3$ [37] corresponding to the nominal valences $2+$, $3+$, and $4+$ of iron.

The experimental [39–41] validation for the cobalt $2+$, $3+$ and $4+$, respectively represented by CoO, $LiCoO_2$ and $SrCoO_3$ is illustrated in Figure 39. Similar to the previous transition metals, the evolution of the spectral format when comparing the spectra without covalence and those where the covalence is included is present as well. This includes the dislodging of the theoretical spectra from ionic to converged to the left of the energy axis, in response to the increase of the oxidation state of cobalt. Like the previous cases, the theoretical calculations present a positive reproduction of the experimental data for the three cases, even smaller structures present in the experimental results are well obtained in both L_3 (between $772\ eV$ and $782\ eV$) and L_2 (between $792\ eV$ and $798\ eV$) regions. This is accompanied by a good acquisition of the spin-orbit coupling separation (between the two regions mentioned before). The consistent trend of increasing covalence between TM-O is observed in both cases to the fully-converged spectra (3, 4, and 5 ECs). This emphasizes the importance of accounting for covalence to achieve a more accurate representation of the experimental data by theoretical results.

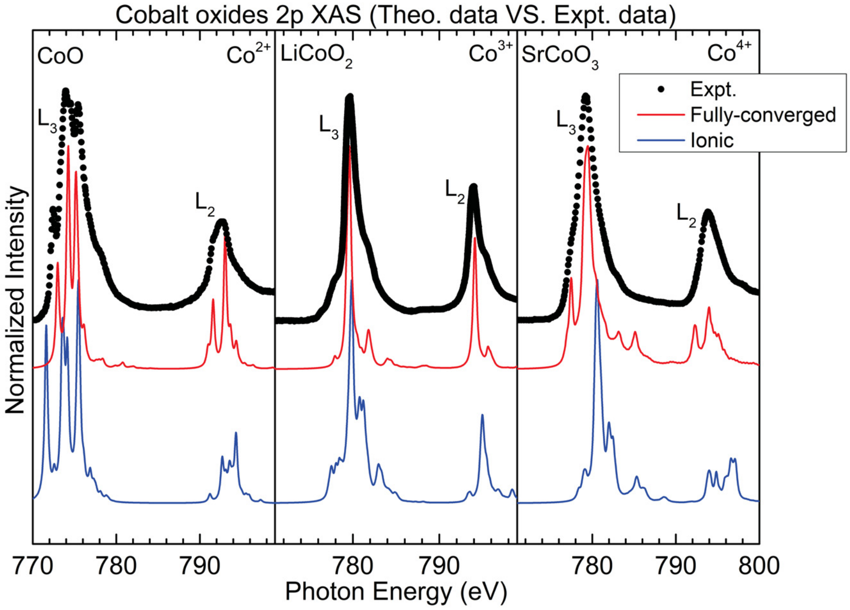

Figure 39 – Comparison of calculated and experimental X-ray absorption spectra for the cobalt series (Co^{2+}, Co^{3+}, and Co^{4+}). Experimental data were collected from CoO [39], $LiCoO_2$ [40], and $SrCoO_3$ [41] representing the nominal valences $2+$, $3+$, and $4+$ of cobalt.

At last, Figure 40 illustrates the evolution of the number of electronic configurations required to achieve more accurate representations of the experimental spectra for all oxidation states of each transition metal oxide studied in this work that manifest octahedral symmetry. This visual representation confirms the previously identified tendency and emphasizes its significance as a necessity. The increase in the number of electronic configurations is essential to conduct a proper analysis using the XAS technique. Also, the covalence contribution is more visible and accentuated in higher oxidation states for all 3 cases treated until now, imposing that the higher the oxidation state, the more covalent the material is, and, as a consequence, the larger the covalence influence in the results presented.

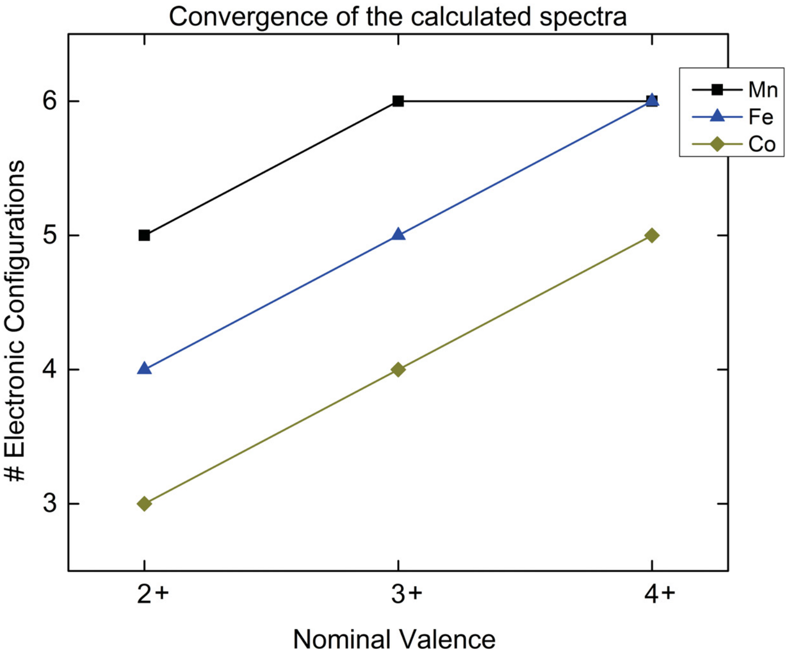

Figure 40 – Evolution of the number of electronic configurations required to achieve visual and real representations of experimental spectra for all oxidation states of the transition metal oxides studied.

With all that has been discussed until now, let us dive into the experimental comparison in which the TM cluster has a different symmetry from the expected octahedral. Here, we present the comparison between the calculated and experimental spectra [42] with respect to the tetragonal symmetry of Mn^{3+}, represented by the double perovskite $SrMn_{0.7}Mo_{0.3}O_3$ [42]. Similarly to the octahedral cases, the calculations were performed following the procedure presented at the beginning of Section 5.1. The plot was generated considering the original energy range and normalized intensity, with a right rigid shift applied to the energy axis of the theoretical spectra until the alignment with the experimental one. Figure 41 illustrates this comparison, and Figure 42 provides a direct comparison between the tetragonal and octahedral results. The initial observation reveals striking similarities between both the octahedral and tetragonal experimental spectra, since they relate to the same transition metal (Mn^{3+}) with identical oxidation states. The primary distinctions lie in the L_3 peak (between $640\ eV$ and $647\ eV$), particularly in the region around $640\ eV$, where the intensity of the structures is slightly smaller in the D_{4h} case. Additionally, the D_{4h} spectra exhibit a slight leftward shift compared to the octahedral spectra for all three spectra, which already manifests an effect of the symmetry reduction. Nonetheless, these differences do not diminish the fact that the calculations exhibit good agreement with the experimental results, affirming the correctness of the implementation. The consideration of atomic and spin-orbit coupling effects, along with the crucial incorporation of symmetry effects, had been performed accurately. Similarly to the O_h case, achieving an accurate representation of the experimental data requires 6 electronic configurations. This reiterates that, despite the symmetry reduction, covalence effects persist in these results.

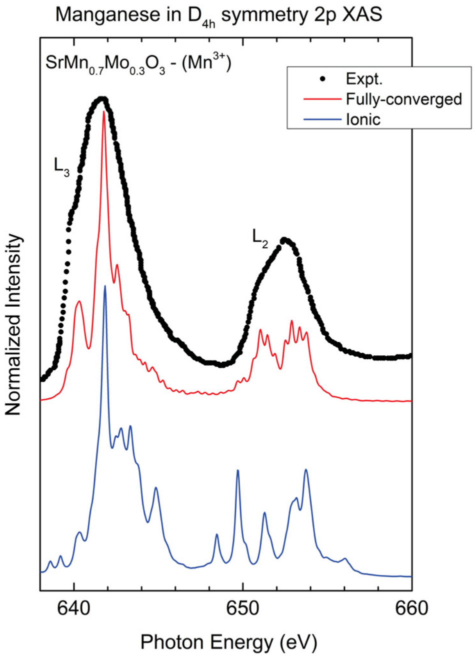

Figure 41 – Comparison between calculated and experimental spectra for the tetragonal symmetry of Mn^{3+}, represented by the double perovskite $SrMn_{0.7}Mo_{0.3}O_3$ [42]

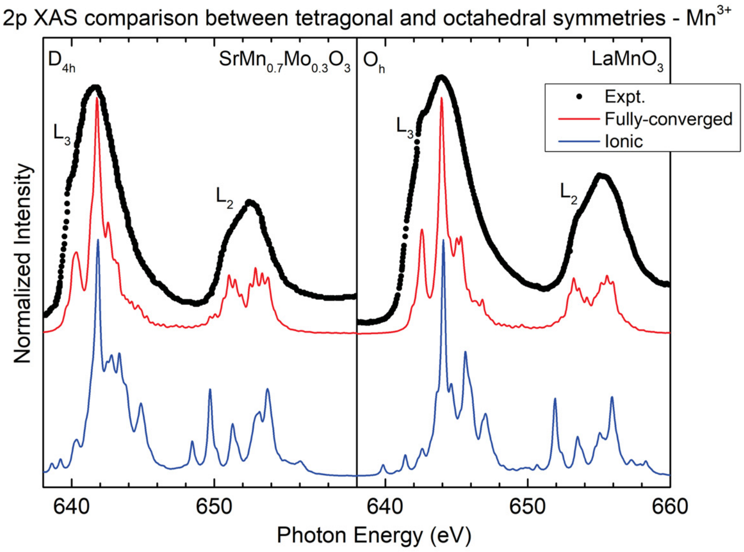

Figure 42 – Explicit comparison between calculated spectra for D_{4h} and O_h symmetries for Mn^{3+} represented by $LaMnO_3$ [37] and $SrMn_{0.7}Mo_{0.3}O_3$ [42].

Now, lets see if the results for last TM studied in this section can reiterate the arguments given until now about the covalence effects. Subsequently, the comparison between calculated and experimental spectra [64] is presented, with respect to the square pyramidal symmetry of V^{5+} represented by vanadium pentoxide (V_2O_5) in its metallic phase [64]. Similarly to previous symmetries, the calculations and the plot follow the same line of thought. Figure 43 illustrates this comparison, accompanied by Figure 44, which explicitly compares C_{4v} and O_h results for the vanadium ion. A notable point is the absence of experimental O_h data due to the fact that V_2O_5 does not exhibit this symmetry, as discussed in Chapter 4. The octahedral calculations are included as a reference to visualize the potential spectral format and understand the impact of the symmetry change in the results, which is why the graph caption for O_h is in quotation marks. Regarding the square pyramidal results, despite the experimental data having a certain proportion of intensities very similar in both L_3 and L_2 structures caused by the effects of the experiment. A good agreement between theoretical and experimental spectra is evident, along with the clear difference between ionic (blue) and fully-converged (red) for both symmetries. There is also another aspect to consider, the left shift from ionic to converged spectra in both cases is considerably bigger than in previous cases, showcasing the high covalent aspect of V^{5+}, which makes the simulations much more sensible to the introduction of the covalence factor. The $V\ 2p_{3/2}$ (between $516\ eV$ and $521\ eV$) and $V\ 2p_{1/2}$ (between $523\ eV$ and $528\ eV$) peaks are well reproduced and the spin-orbit effect (around $522\ eV$) is well taken into account. When comparing the symmetries, the O_h results bear some resemblance to the actual symmetry of the material. However, for both ionic and fully-converged spectra, the V $2p_{1/2}$ region exhibits fewer structures in the O_h spectrum compared to the C_{4v} results. Furthermore, in the L_3 region, the first peak at around $517\ eV$ is much more prominent in O_h symmetry, highlighting the direct effects of symmetry reduction. When considering covalence effects, a similar behavior is observed as in the tetragonal case. To accurately reproduce the experimental data, 7 electronic configurations are required, regardless of symmetry. This further emphasizes that covalence effects persist even in theoretical scenarios, reinforcing their relevance in the understanding of the obtained results.

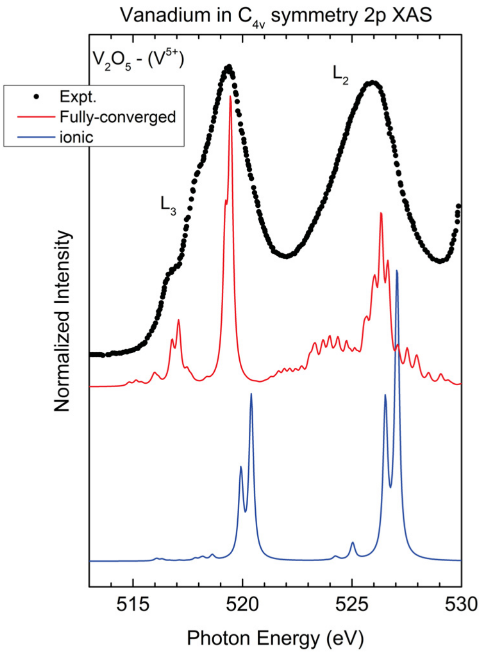

Figure 43 – Comparison between calculated and experimental spectra concerning the square pyramidal symmetry of V^{5+}, represented by vanadium pentoxide V_2O_5 in its metallic phase [64].

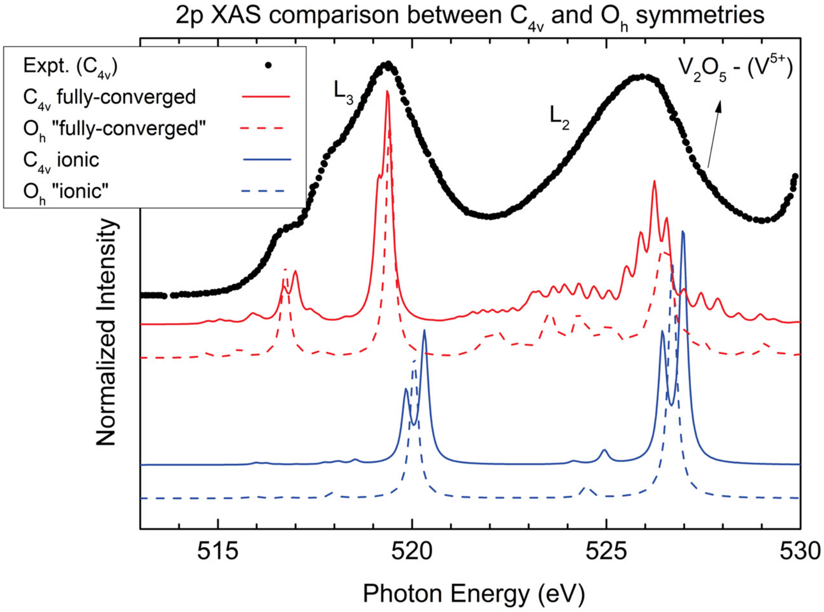

Figure 44 – Explicit comparison between calculated spectra for C_{4v} and O_h symmetries for V^{5+} in vanadium pentoxide V_2O_5 [64].

Now, in the following section, results regarding the ground state and theoretical spectra calculated for each TMO studied until now will be presented.

5.1.2 Ground state and theoretical details

Next in this discussion is the results concerning GS and the theoretical details of the TM $2p$-edge XAS. Here, the analysis will encompass results like the ground state electronic composition, along with numerical results regarding information about the GS energy, $3d$ electrons, and the spin state. Along with it, there will be a discussion regarding theoretical spectra calculated considering the procedure exposed in the beginning of the $L_{2,3}$ section. Starting with Figure 45, which presents the calculated contributions of the configurations to the ground state of each transition metal in octahedral symmetry. The configurations are shown with the $d_{TM}^{n+m}\underline{L}^{p+m}$ notation, with n and p being the initial number of TM and oxygen electrons and m taking values of 1, 2, 3 etc. In particular, an increase in nominal valence reveals a trend towards a covalent GS configuration, specifically $d^{n+1}\underline{L}$. This trend is pronounced for Mn^{4+}, Fe^{4+}, Co^{3+} and Co^{4+} where approximately 50% or more of the GS is characterized by this configuration, with the second most prevalent being d^n. This tendency intensifies in more covalent compounds, marked by higher oxidation states and lower initial state valence. For other materials, the dominant contribution comes from the d^n configuration, which represents more than 53% of the contribution. Notably, an increase in nominal valence requires an increase in the number of configurations required to accurately describe the GS. This variation is more conspicuous in highly covalent compounds, but remains significant in less covalent compounds, as shown in Table 3 for the iron series. It is possible to observe that in the table with more details what was discussed previously. In Fe^{2+} (less covalent), the GS is mainly described by the d^n configuration (ionic character). However, as the nominal valence increases, increasing the covalent factor of the TM, not only it is necessary to include more configurations to describe the GS, but also the GS becomes more covalent as well. Until reaching the highest oxidation sate (Fe^{4+}), the GS becomes covalent, described mainly by the $d^{n+1}\underline{L}$ configuration. Similarly to Fe^{4+}, in materials like Mn^{4+} and Co^{4+}, a discernible need for a bigger number of configurations to describe their GS is evident as well, underscoring their high covalency, and reinforcing the fact that they are in the Negative Charge Transfer regime, characterized by their covalent GS. This is shown in Figure 45 by the peaks present above the $d^{n+1}\underline{L}$ configuration.

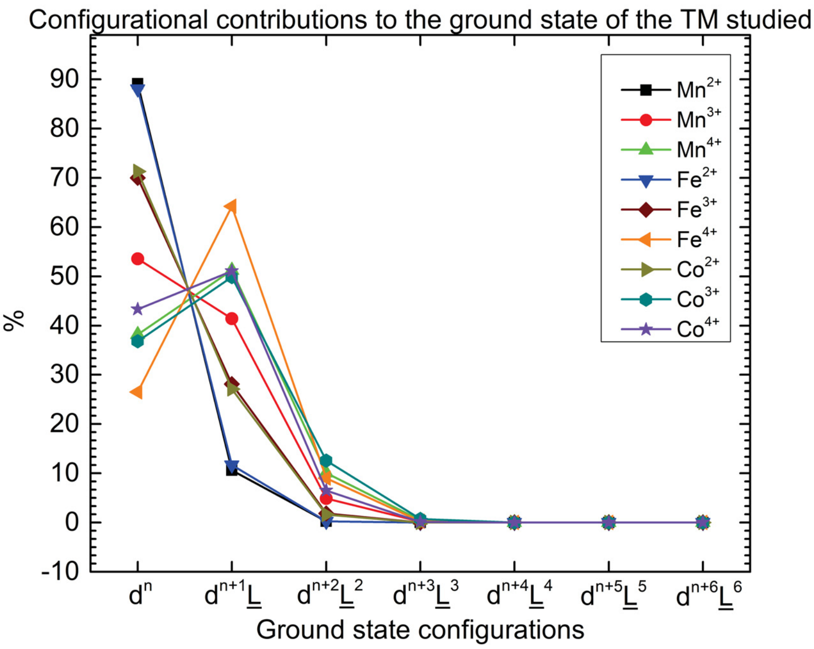

Figure 45 – Calculated contributions of various electron configurations to the ground state of each transition metal in octahedral symmetry.

Fe^{2+}		Fe^{3+}		Fe^{4+}	
$Config.$	$\%$	$Config.$	$\%$	$Config.$	$\%$
d^6	88.02	d^5	70.01	d^4	26.54
$d^7\underline{L}$	11.71	$d^6\underline{L}$	28.11	$d^5\underline{L}$	64.19
$d^8\underline{L}^2$	0.27	$d^7\underline{L}^2$	1.85	$d^6\underline{L}^2$	9.00
$d^9\underline{L}^3$	$1.45 \cdot 10^{-3}$	$d^8\underline{L}^3$	$2.89 \cdot 10^{-2}$	$d^7\underline{L}^3$	0.27
		$d^9\underline{L}^4$	$1.30 \cdot 10^{-4}$	$d^8\underline{L}^4$	$2.30 \cdot 10^{-3}$
				$d^9\underline{L}^5$	$7.63 \cdot 10^{-6}$

Table 3 – Configurational contributions to the ground state of the iron ions, namely Fe^{2+}, Fe^{3+} and Fe^{4+} in octahedral symmetry.

The next result to be analyzed is the GS magnetic momentum of each TM studied. The momenta values were obtained through the value of S^2, calculated using Quanty [57], where the formula $\mu_{calculated} = 2\sqrt{S^2}$ was used in Bohr Magneton units and the number of ECs capable of reaching the convergence of these values was considered. To make an analysis of covalence effects, the expected magnetic momentum, which is equivalent to the momentum related to the ionic configuration, was calculated according to the spin configuration that describes the GS by considering the spin alignment and estimation of the value of S. To do this, the equation $\mu_{ionic} = 2\sqrt{S(S+1)}$ was used, giving the result, as in the previous case, in Bohr Magneton units [132]. Thus, the values of μ_{ionic}, $\mu_{calculated}$ are presented in Table 4, along with the spin configuration and the value of S considered for each compound presented in Chapter 4.

Comparing the values of ionic and calculated μ, presented in Table 4, it is

$Transition\ Metals$	$Spin\ Config.$	S	$\mu_{ionic}\ (\mu_B)$	$\mu_{calculated}\ (\mu_B)$
$Mn^{2+}\ (MnO)$	$t^3_{2g\uparrow}e^2_{g\uparrow} \rightarrow HS$	$5/2$	5.92	5.81
$Mn^{3+}\ (LaMnO_3/Mn_2O_3)$	$t^3_{2g\uparrow}e_{g\uparrow} \rightarrow HS$	2	4.90	4.97
$Mn^{4+}\ (SrMnO_3)$	$t^3_{2g\uparrow} \rightarrow HS$	$3/2$	3.87	4.25
$Fe^{2+}\ (FeO)$	$t^3_{2g\uparrow}t_{2g\downarrow}e^2_{g\uparrow} \rightarrow HS$	2	4.90	4.78
	$t^3_{2g\uparrow}t^3_{2g\downarrow} \rightarrow LS$	0	0.00	
$Fe^{3+}\ (LaFeO_3)$	$t^3_{2g\uparrow}e^2_{g\uparrow} \rightarrow HS$	$5/2$	5.92	5.61
$Fe^{4+}\ (SrFeO_3)$	$t^3_{2g\uparrow}e_{g\uparrow} \rightarrow HS$	2	4.90	5.30
$Co^{2+}\ (CoO)$	$t^3_{2g\uparrow}t^3_{2g\downarrow}e_{g\uparrow} \rightarrow HS$	$1/2$	1.73	1.92
$Co^{3+}\ (LiCoO_2)$	$t^3_{2g\uparrow}t^3_{2g\downarrow} \rightarrow LS$	0	0.00	1.49
$Co^{4+}\ (SrCoO_3)$	$t^3_{2g\uparrow}t_{2g\downarrow}e^2_{g\uparrow} \rightarrow IS$	$3/2$	3.87	5.28

Table 4 – Mean spin (S) value, ionic and calculated magnetic momentum ($\mu\ (\mu_B)$) values considering the spin states ordering of each transition metal studied.

possible to see that no material has an equal momentum value to the ionic one, indicating a direct effect of the covalence present in the TM-O cluster. Clearly, none of the values are equal due to the presence of all interactions considered in the calculations. However, these values can be used to verify what was discussed in Chapter 4, which makes it possible to see if the transition metal ions respect the spin configuration imposed by the materials being studied by this research. Furthermore, it is noticed that in cases where the material is less covalent, the difference between the values is lower, but still present, which is illustrated in Figure 46. The graph presents a direct comparison between the ionic and calculated values of the magnetic momenta showcased in Table 4. They are given as a function of the transition metal considered. The bigger difference between the momenta values for more covalent compounds is well represented here, as well as the small, but still visible difference in less covalent TMs.

Now, let us examine, in more detail, two peculiar cases– the ions Fe^{2+} and Co^{4+}. The first has a GS that can suffer a spin transition, as explained in Chapter 4, but according to the calculations performed, this compound can be said to be in a high-spin state, since the obtained μ is very close to the ionic in this spin state. As for Co^{4+} which present a peculiar behavior of an intermediate-spin state, the difference between the calculated and expected values is considerable compared to the other TMs. However, if compared to an ion with a high-spin configuration like Fe^{2+}, the calculated momentum ($\mu_{calculated} = 5.28\ (\mu_B)$) is considerably close to the expected ($\mu_{expected} = 4.90\ (\mu_B)$). That is why it can be said that Co^{4+} GS can be described by a high-spin state Co^{3+} with an oxygen hole $\underline{L}$. There are two more GS results that can be analyzed. The ground state mean energy and the $3d$ band electron count. Figure 47 offers a comprehensive visualization of the behavior exhibited by all materials calculated under octahedral symmetry, revealing their relative ground state mean energy and the $3d$ band electron count. The relative energy and number of $3d$ electrons are related to the ionic state of each material, or just 1 EC.

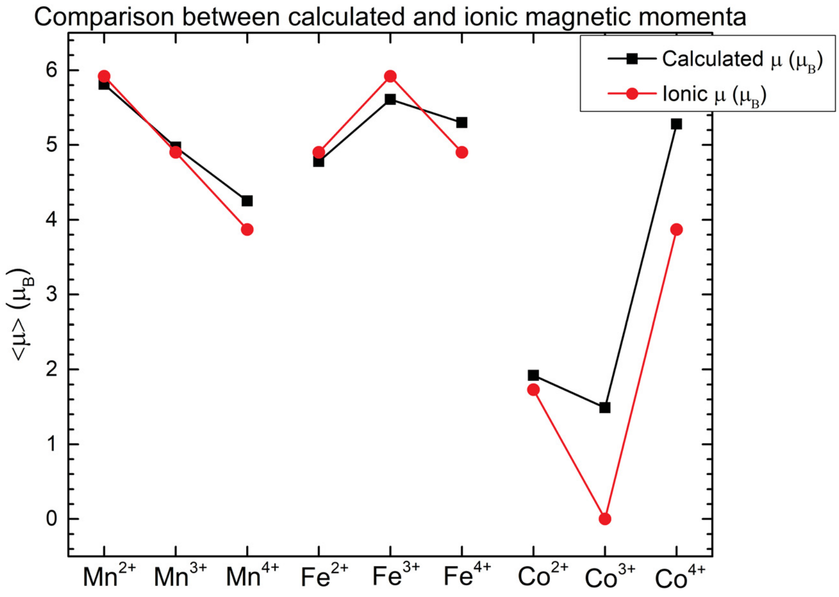

Figure 46 – Comparison between ionic and calculated magnetic momenta for the TMs with O_h symmetry.

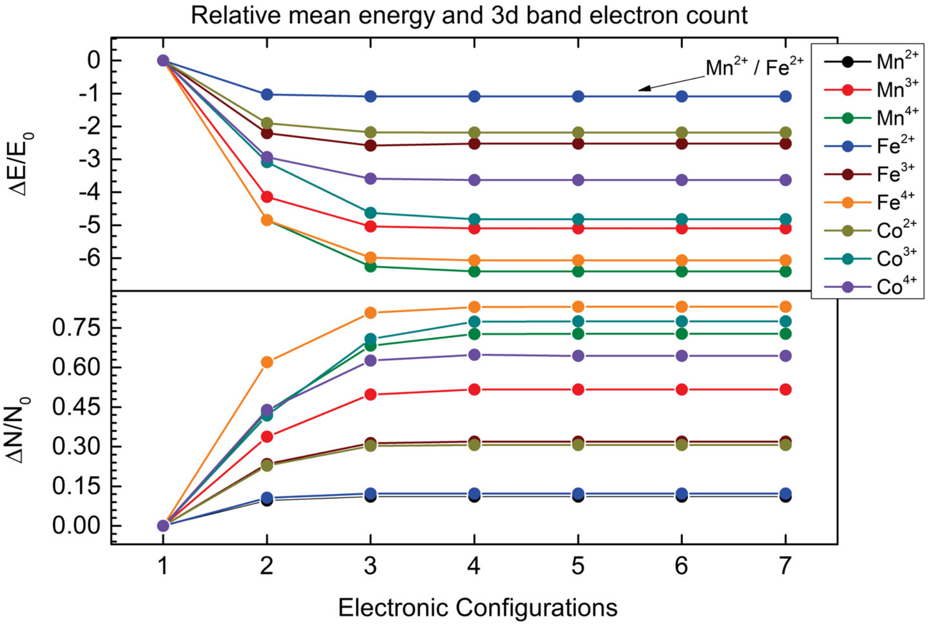

Figure 47 – Convergence analysis of the ground state relative mean energy, related to the ionic state, and $3d$ band electron count. Both were calculated for each material that manifests O_h symmetry.

The graph is intentionally structured to illustrate a significant trend: as the oxidation state of a transition metal increases, there is a proportional amplification in the variation of calculated values, necessitating a higher number of ECs for convergence. The chosen cutoff of 7 ECs stems from the highest number required to achieve convergence in both mean values and calculated spectra. Although considering more than 6 ECs for the highest covalent transition metal (Mn^{4+} or Fe^{4+}) may not have physical relevance, it proves insightful. This not only serves as a validation check for the employed program, but also allows for an exploration of how mean values converge relative to expectations. So, in order to obtain the convergence of these values, it was required, for the manganese series, 5, 6 and 6 ECs are needed. For Iron, 4, 5 and 6 EC and, lastly, for cobalt, 3, 4 and 5. These numbers are given for the respectively nominal valences of $2+$, $3+$ and $4+$. The tendency to increase, or at least to keep, a high number of electronic configurations, and, as a consequence, the GS being predominately covalent is present here. This gives further evidence that the covalence included in the calculations does play a crucial role in the effects that need to be accounted for for the correct interpretation of the results regarding X-ray absorption spectroscopy.

Following the discussion in Section 5.1.1 a valid question arises. Is it really necessary to consider so many electronic configurations to correctly describe the property effects of interest of this thesis? For that, Figure 48 is presented. This graph showcases the variation of mean energy and number $3d$ band electron count between ionic (black lines) intermediate (green lines) and fully-converged (red lines) configurations, accordingly to the increase of the oxidation state of each transition metal characterized by the octahedral symmetry. The intermediate configuration was calculated using 2 electronic configurations (which is the first configuration to include the covalence into the calculation, which we named as covalence first approximation).

There are two main aspects to analyze here, the first is the abrupt variation of energy and $3d$ electrons as the metal's nominal valence is augmented and covalence is included. The other is the clear difference between values related to the ionic and converged configurations. The higher displacement mentioned above for Figure 47 is better visualized here, mainly for the more covalent cases. Starting from the fact that the ionic configuration is the ideal scenario where there are no interactions but only the ones related to the TM, and the fully-converged configuration theoretically includes all interactions to be accounted for by the implemented cluster model. As already mentioned in the experimental comparison section, the latter is the more accurate calculation to represent the experimental data and what is actually happening to the studied material under the influence of the XAS technique. It would be possible to question whether the configurations between the two presented duos could be enough to perform the analysis of the influence of covalence, here is where the intermediate configuration plays its role in the visualization. Even in less covalent compounds where the difference between the values is smaller, the results of Figures 47 and 48, when put together, make it possible to state that covalence indeed plays a pivotal role in the interpretation of the XAS technique. Because of this, answering the first proposed question yes, it is necessary to add the extra ECs, even in less covalent cases, because without this, whatever small the hybridization between TM and O orbitals is, it is still very important to account for to make the theoretical predictions more close to what is really happening to the studied sample and better understanding what is really going on with it.

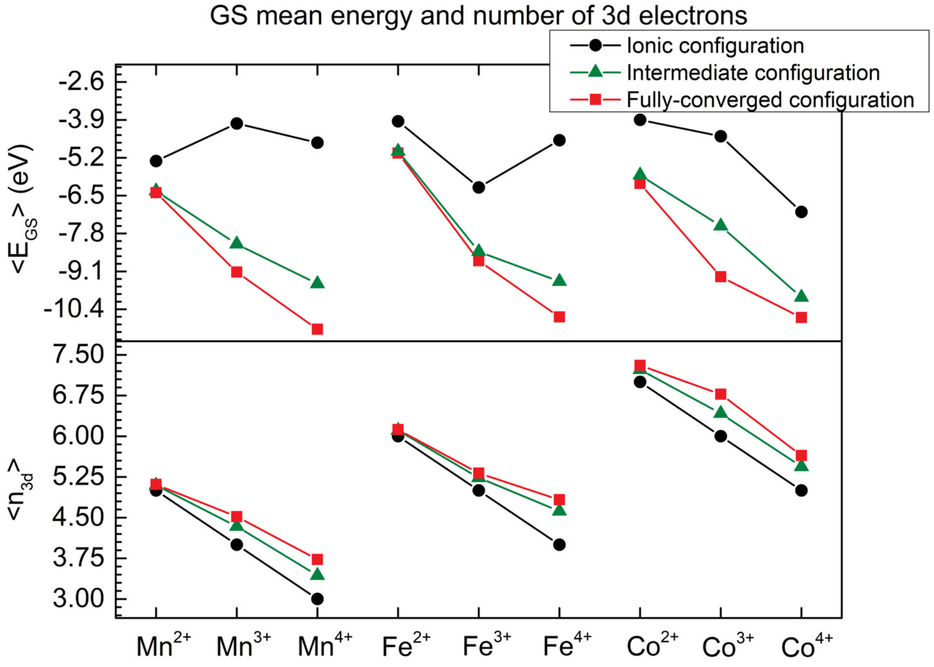

Figure 48 – Illustration of the difference of the ground state mean energy and $3d$ band electron count for the O_h TMs, between the ionic and fully-converged configurations.

With this, the discussion about the ground state results regarding the transition metals with O_h symmetry is finished. Now let us delve into results containing the calculated XAS spectra for Mn, Fe, and Co. After that, a discussion about the theoretical results regarding reduced symmetries will be done.

The next set of results encompassed by Figures 49–51 provides an in-depth analysis of the $2p$ X-ray absorption spectra, which were calculated utilizing the Quanty implementation [57] and the same procedure explained in the beginning of this Chapter. The graphs were plotted against the average energy related to the configuration energy; a rigid shift along the intensity axis was applied to enhance the clarity of spectral shape evolution. Also, the L_3 and L_2 peaks are indicated in each graph as well.

Firstly, Figure 49 displays the $2p$ X-ray absorption spectra calculated for the manganese ions, namely Mn^{2+}, Mn^{3+}, and Mn^{4+}. The evolution of the L_3 ($2p_{3/2}$) and L_2 ($2p_{1/2}$) peaks, spanning $-5\ eV$ to $2\ eV$ and $7\ eV$ to $13\ eV$, respectively, is discernible as the number of electronic configurations increases. The variation in spectral shape becomes more pronounced with higher nominal valences. Although the difference in shape between the ionic spectrum and subsequent configurations is less conspicuous for lower oxidation states, it remains noteworthy. Additionally, a distinct displacement is observed from the ionic spectra to the first instance of covalence in the three cases, becoming more visible as the nominal valence increases. Here, the whole spectrum suffers a leftward displacement in relation to the energy axis, until achieving the correct shape with three electronic configurations. This displacement is accompanied by a chemical shift resulting from increased oxidation state. The shift is more pronounced in the case of Mn^{4+}, underscoring the impact of covalence of the ion. Moreover, as the oxidation state rises, there is a tendency to increase the number of electronic configurations required for convergence, and notably, it takes more configurations to achieve even a first visual glimpse of the fully-converged spectrum.

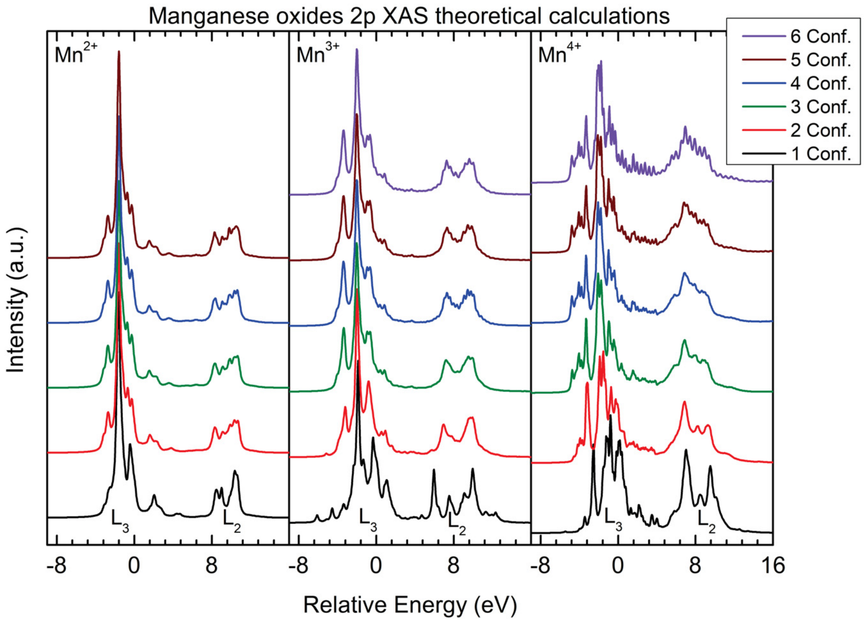

Figure 49 – $L_{2,3} - edge$ X-ray absorption spectra calculated for manganese ions, specifically Mn^{2+}, Mn^{3+} and Mn^{4+}, using *Quanty* [57].

The $2p$ X-ray absorption spectra for the iron series, covering Fe^{2+}, Fe^{3+}, and Fe^{4+}, are presented in Figure 50. Similar to manganese, the L_3 ($2p_{3/2}$) and L_2 ($2p_{1/2}$) peaks, in the region of $-6\ eV$ to $2\ eV$ and $7\ eV$ to $15\ eV$, respectively, become more pronounced as the number of ECs is increased. This evolution is particularly noticeable in the spectra related to the higher oxidation state (Fe^{4+}). Additionally, the displacement from ionic spectra until reaching the correct position in energy to the left of the energy axis (approximately $1\ eV$ leftward) is observed in the iron results, accompanied by a chemical shift caused by the increase in nominal valence. These shifts become more discernible as the nominal valence increases, underscoring the influence of the covalent aspect of the system. There is a need, similar to that of manganese, to increase the number of electronic configurations required for convergence. It takes more configurations to achieve the fully-converged spectra with the increase in nominal valence.

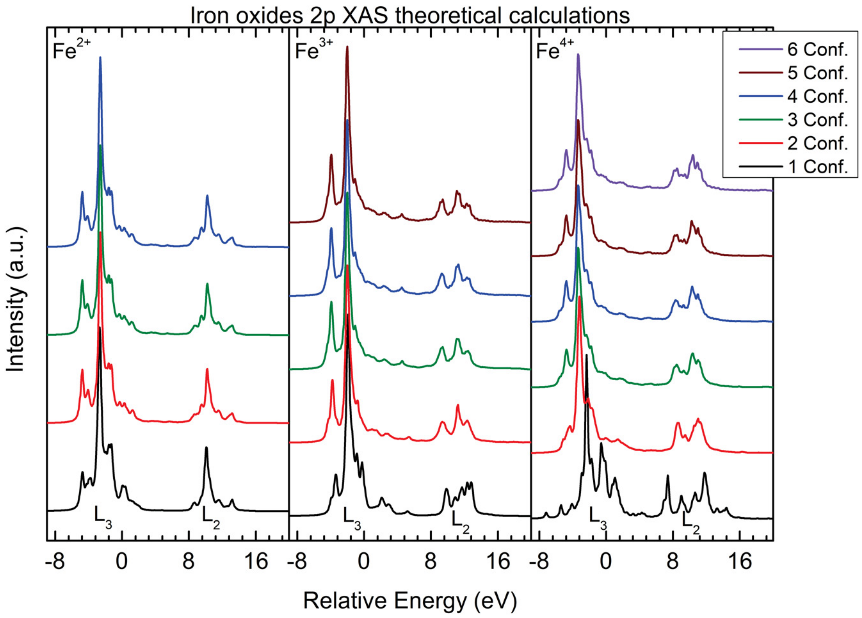

Figure 50 – $L_{2,3} - edge$ X-ray absorption spectra calculated for iron ions, specifically Fe^{2+}, Fe^{3+} and Fe^{4+}, using *Quanty* [57].

Lastly, for the O_h TM studied, Figure 51 presents the $2p$ X-ray absorption spectra for the cobalt series, encompassing Co^{2+}, Co^{3+}, and Co^{4+}. Similar to the two previous cases, analogous effects are evident in these theoretical calculations. This includes the evolution of both L_3 ($2p_{3/2}$) and L_2 ($2p_{1/2}$) peaks and their structures, ranging from -10 eV to 1 eV and 10 eV to 16 eV, respectively. The spectral shape changes are less apparent for less covalent materials (lower oxidation state) and more pronounced for more covalent ones (higher oxidation state), with a tendency to increase the number of electronic configurations for spectral convergence as the nominal valence is increased. Notably for cobalt, which is less covalent than the others, as showed in Figure 45, changes in the calculated spectra are less evident, but still significant. This provides further evidence that even when the effects are less apparent, covalency remains a crucial factor to consider in the study.

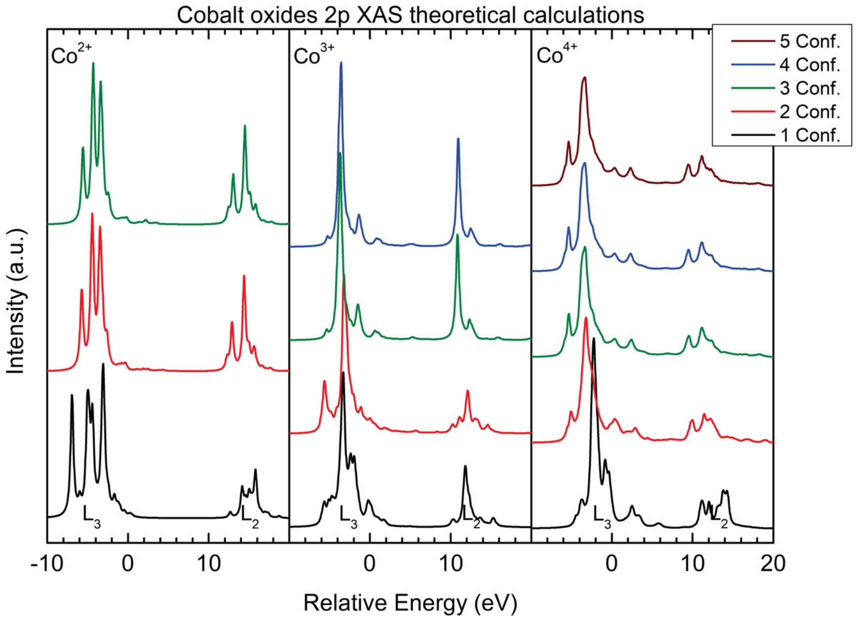

Figure 51 – $L_{2,3} - edge$ X-ray absorption spectra calculated for cobalt ions, specifically Co^{2+}, Co^{3+} and Co^{4+}, using *Quanty* [57].

The analysis of these theoretical results underscores the clear influence of covalence, evident not only in the inclusion of more TM-O interactions but also in the metal atom itself through an increase in oxidation state. This is manifested more substantially in the variations of the spectral format, where it becomes necessary to include more electronic configurations to achieve a representation converging to the actual spectrum. Now, the subsequent discussion will delve into the covalence effect in conjunction with different symmetry considerations.

Now, analyzing the GS results considering the TMs with reduced symmetries, namely Mn^{3+} and V^{5+}, Figure 52 displays the computed contributions of the configurations to the ground state of manganese $3+$ in tetragonal symmetry and vanadium $5+$ in square pyramidal symmetry. The notation used is the same as in the octahedral case, $d_{TM}^{n+m}\underline{L}^{p+m}$. Starting with manganese, it should be noted that, compared to the octahedral case with the same oxidation state of Mn^{3+}, the D_{4h} case exhibits a slight decrease in covalent contributions, rendering it marginally less covalent than its predecessor. However, the primary GS contributions, mainly d^n orbitals, remain consistent, accounting for more than 50% in both symmetries. While V^{5+} predominantly exhibits covalent configurations in both considered symmetries, particularly $d^{n+1}\underline{L}$ and $d^{n+2}\underline{L}^2$, accounting for at least 70% of the GS configuration, when only around 16% is attributed to d^n. This result is very consistent with the one obtained in [52, 64], except for the small difference that can be attributed to the fact that in the reference the calculations were performed without considering full multiplet effects. The evolution of the contribution values respects the tendency imposed previously with the augmentation of the oxidation state for the same atom, but no other material expressed the same diffusion of the GS contribution as here presented by V^{5+}. It is important to remember that in this specific case, the O_h results are only for reference; however, they are not less important, since it is possible that regardless of a real or fake scenario, the vanadium ion still presents covalent behavior.

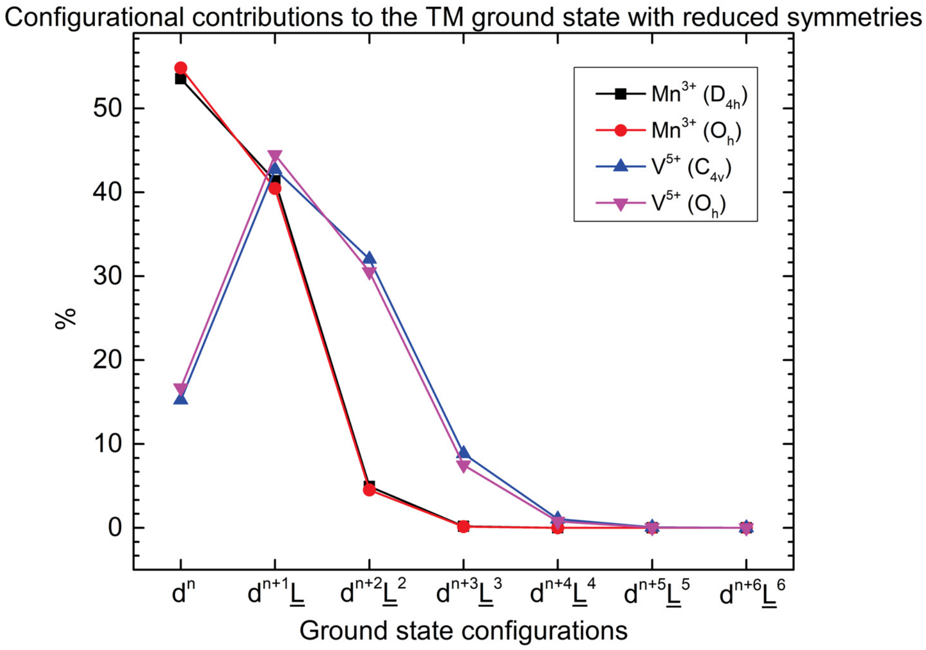

Figure 52 – Calculated contributions of various electron configurations to the ground state of Mn^{3+} in the D_{4h} symmetry and V^{5+} in the C_{4v} symmetry, comparing with O_h data.

Now, with respect to the magnetic momenta analysis for these two TMs, a similar graph to the one in Figure 46 is presented in Figure 53. However, in this case, as in the previous analysis on GS contributions, the comparison was made not only between calculated and ionic μ, but also between symmetries. An aspect to note in the Mn^{3+} results is that, compared to the O_h case, both results are very close. Although, in tetragonal symmetry, it increases slightly making it more distant from the ionic value for Mn^{3+}, $\mu_{expected} \approx 4.90\ (\mu_B)$. This contributes to the state that the symmetry lowering affects the results regarding the XAS technique despite of the symmetry considered, even though, when considering the same material the symmetry effects need to be accounted for as well. In the case of V^{5+}, since it is characterized by an initial configuration d^0 in both symmetries, its ionic expected magnetic momentum is 0. However, as the covalence is included in the system, it develops a magnetic momentum. Due to this, it is possible to, again, state how important it is to consider properly the covalence effects. Also, this reinforces the big difference between ionic and fully-converged spectra that was seen in the experimental comparison of V^{5+}, in Figure 43.

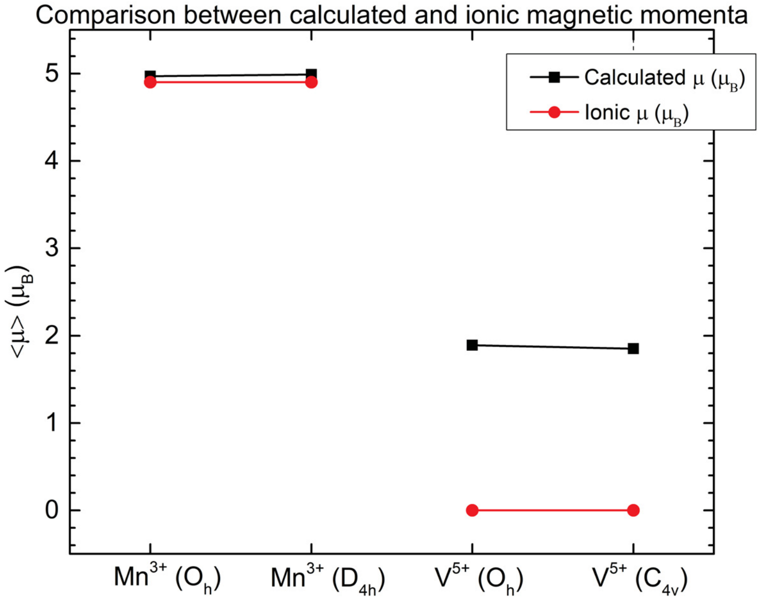

Figure 53 – Comparison between ionic and calculated magnetic momenta for Mn^{3+} and V^{5+} comparing these values between tetragonal and square pyramidal symmetries to octahedral results.

A graphical representation akin to Figure 47, portraying the evolution of relative GS energy and $3d$ electron count values for the reduced symmetries, is presented in Figure 54. This comparison aims to elucidate how varying symmetries, coupled with covalent aspects, can impact the ground state of different transition metal oxides. In particular, calculations for O_h symmetry are included for both compounds, despite V^{5+} not possessing this specific symmetry as detailed in Chapter 4. It is evident that even with a symmetry reduction, the variations in energy and $3d$ electrons are analogous but not identical, as different effects are considered in each calculation. For instance, if V^{5+} had all six oxygen atoms in its cluster, the GS energy would be even lower than observed. Similarly, for the manganese case, the difference in energy between symmetries is not significant, but the O_h case has a lower GS energy, consistent with the octahedral V^{5+}. This pattern is echoed in the $3d$ electrons results, where the difference between symmetry outcomes is less pronounced than in the energy case, yet the octahedral values stand out. Establishing a connection between the symmetry and covalence effects, for a more covalent compound such as V^{5+}, the variation in both mean values as the number of electronic configurations increases is more substantial. Achieving convergence requires more electronic configurations for V^{5+} compared to manganese, although the number of configurations required remains consistent with symmetry reduction: six electronic configurations for both symmetries for Mn^{3+} and seven electronic configurations for both symmetries for V^{5+}.

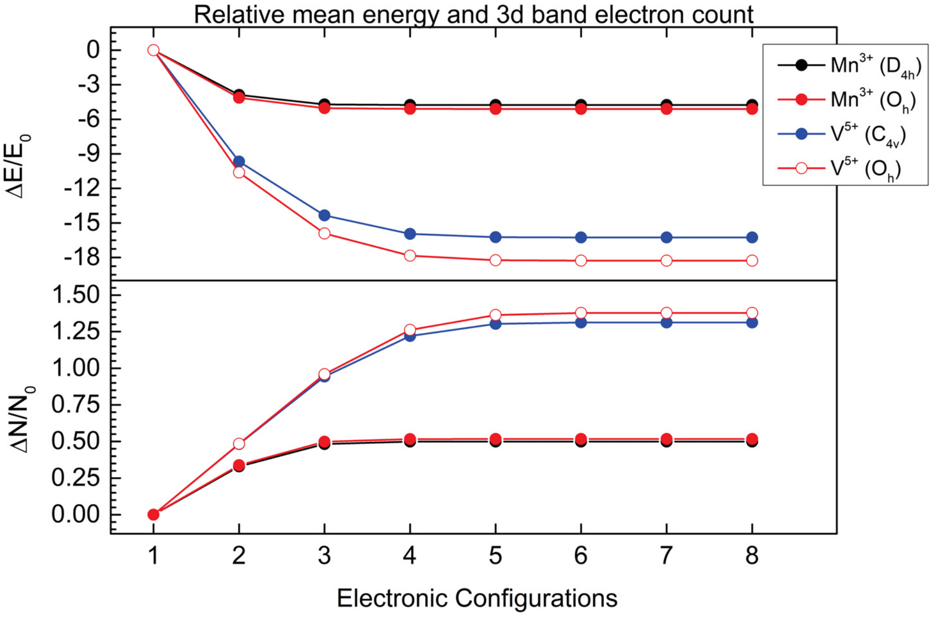

Figure 54 – Convergence analysis of the ground state relative mean energy, related to the ionic state, and $3d$ band electron count. Both were calculated for Mn^{3+} and V^{5+} in their related lowered symmetries D_{4h} and C_{4v}, respectively. Including also octahedral calculations for covalence and symmetry effects visualization.

In a similar line, though used in the O_h discussion, Figure 55 illustrates the variation of the mean energy and $3d$ band electron count between the ionic, intermediate and fully-converged configurations. This was done taking into account the symmetry lowering effect in both TMs. An obvious aspect to note is that the initial number of $3d$ electrons (ionic state) is the same. This is due to the fact that this characteristic does not change regardless of the symmetry, since it is the same TM ion. Another thing to extract from Figure 55 is the not so great variation in energy and $3d$ electrons for Mn^{3+} as the symmetry is reduced, compared to the vanadium ion. This can be extended when comparing the values of the ionic, intermediate and converged configuration for each TM. This not only showcases the effects, even if smaller ones, of the symmetry lowering into the calculations, but also highlighting the influence of covalence in high oxidation ions, like it was shown for Mn^{4+}, Fe^{4+} and Co^{4+}, for example. However, to be clear, in less covalent materials, the effects treated can be smaller, but still not negligible. With this, the plea that extra electronic configurations, especially the one related to the fully-converged state, are of most importance to accurately study the effects of covalence into the results regarding the XAS technique when applied to transition metal oxides, regardless of the symmetry they manifest. This makes it possible to better understand their electronic structure in a more in-depth way.

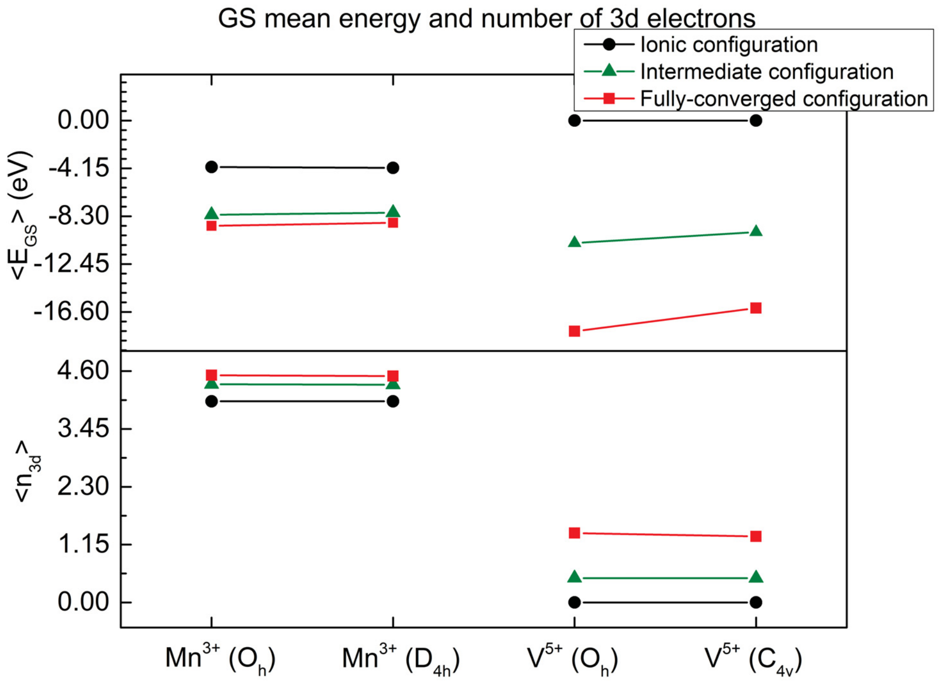

Figure 55 – Illustration of the difference of the ground state mean energy and $3d$ band electron count for Mn^{3+} and V^{5+}, between the ionic and fully-converged configurations. Along with the comparison between O_h symmetry and reduced cases.

Starting the analysis regarding the theoretical XAS calculated considering the reduced symmetries treated by this research, there is Figure 56. The calculations presented in the graph follow the parameters of Table 1, with a Gaussian broadening of $0.1\ eV$. The spectral shape in Figure 56 reveals a more pronounced evolution in the L_3 (from $-4\ eV$ to $2\ eV$) peaks compared to the L_2 (from $6\ eV$ to $11\ eV$) peaks. The leftward shift in energy is evident not only in the overall $2p_{3/2}$ region but also in its individual structures, leading to a convergence pattern. Although this shift is present in the $2p_{1/2}$ peaks as well, it is less prominent. A similar shape evolution is observed in the octahedral symmetry for the same material. Despite the similarities in spectra due to the common material, distinctions emerge, such as fewer structures at the $2p_{3/2}$ peak and the appearance of new features in $2p_{1/2}$, as demonstrated before, in the experimental comparison. These differences are clear effects of the altered symmetry considered in this analysis. By comparing the evolution of the spectra as the covalence between the transition metal and oxygen increases in different symmetries, a consistent rate of change is observed in both cases. Furthermore, it is required, as in the O_h case, 6 electronic configurations to achieve spectrum convergence. This indicates that, despite the symmetry change, covalence effects persist in both results at a similar rate.

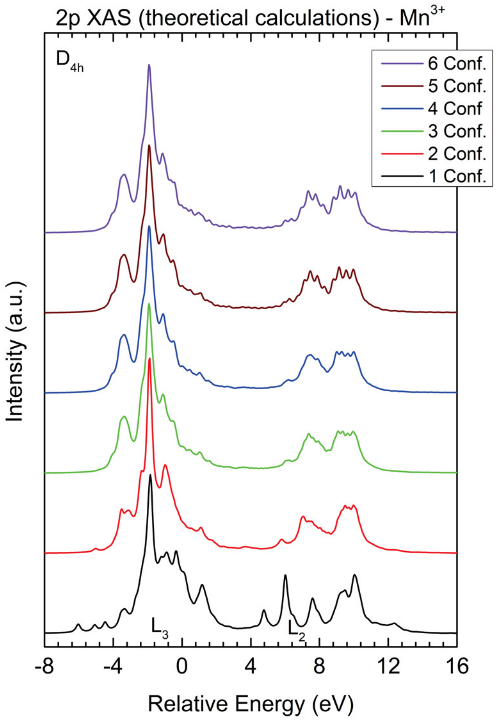

Figure 56 – $L_{2,3}$-edge X-ray absorption spectra calculated for the tetragonal Mn^{3+}, using *Quanty* [57].

The last discussion of this section details the X-ray absorption spectra calculated using *Quanty* [57], focusing on the square pyramidal symmetry for V^{5+}. The cluster model calculations follow the same procedure as used in the previous simulations presented throughout this section. The spectral shape shown in Figure 57 exhibits different characteristics. In particular, the intensity of the L_2 peak in the ionic spectrum (from $4\ eV$ to $8\ eV$) is particularly pronounced compared to other results. However, as one progresses to the second spectrum and beyond, the intensities of the peaks gradually diminish. Similarly to other cases, a leftward shift in energy is observed as the number of electronic configurations increases by about $1\ eV$. However, consistent with expectations for a material with a higher oxidation state, the number of electronic configurations needed to achieve the final converged spectrum is 7 ECs. This heightened requirement for additional electronic configurations underscores the significant covalent aspect of V^{5+}, which contributes to the increased presence of covalence effects in the calculated results.

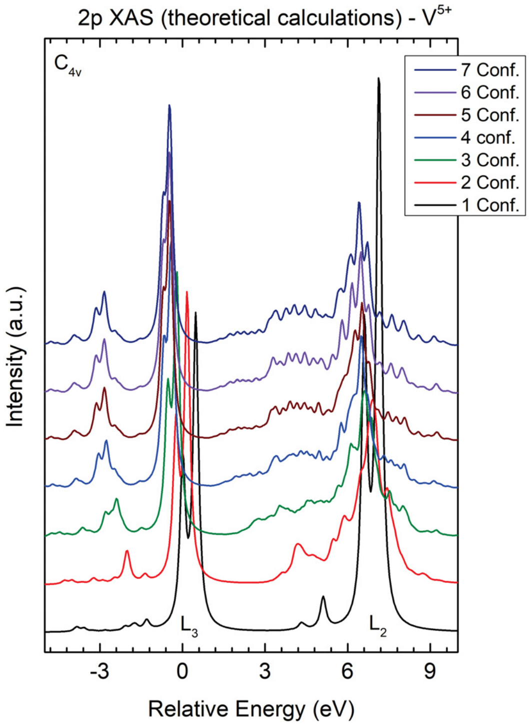

Figure 57 – X-ray absorption spectra calculated for the square pyramidal symmetry of V^{5+}, using *Quanty* [57].

After this extensive discussion, it is already possible to draw some conclusions. The main information is the clear influence of covalence on the results with respect to the TMs $2p$-edge, regardless of the symmetry they present. Now, let us see if the observed behaviors in the $2p$-edge repeat to another portion of the electronic structure being analyzed, the O $1s$-edge.

5.2 *O K*-edge X-ray absorption spectroscopy

This section delves into the outcomes obtained regarding the O K or $1s$ edge X-ray absorption spectroscopy of the transition metal oxides studied. Like in the previous sections, the analysis not only encompasses covalence effects but also accounts for possible symmetry effects that can occur considering each system. The O $1s$ XAS maps, in the first approximation, the O $2p$ character of the unoccupied portion of the electronic structure of the system. These, in their instance, are covalently mixed with different states of the TM via hybridization [130, 133]. Unlike the $2p$-edge XAS, the spectra present here are not divided by the peaks, since it is only related to the TM d states. The structures present in the results correspond to the TM $3d$ states more precisely, as the transition metals studied here belong to the $3d$ series of the periodic table. Also, the peaks present in the spectra have their separation given by crystal field effects; because of this, it is possible to identify the orbital contributions in the spectra intensities.

With the goal of establishing a comparison between the calculations performed and the $O\ 1s$ absorption spectra to reinforce the arguments of the previous section, the calculations were made ignoring full multiplet effects, considering only transitions such as $d^n \rightarrow d^{n+1}$, without considering $O\ 2p$ effects. Although it is a calculation of the transition metals, the results should present the same structures as the oxygen absorption spectra. This is made by considering a $TM\ 2p$ hole that does not interact with the d states and does not possess spin-orbit coupling. This procedure is already well known [134, 135]. However, it is important to point out that the intensities generated by these calculations come from dipole transition matrix elements between the TM $2p \rightarrow 3d$, so the relation between the resulting intensities will not be the same as the absorption spectra related to transitions of the oxygen's $1s \rightarrow 2p$.

The calculations present in the analysis of the $O\ 1s$-edge were computed using the implementation of *MATLAB* [78] and carried out with the parameters described in Table 2 of Chapter 3. The maximum number of electrons required to fill the d band of each metal, determined by its oxidation and valence states, served as a stopping criterion. In other words, the maximum number of electronic configurations was employed for each case. The majority of spectra feature a Lorentzian broadening of $\Gamma = 0.5\ eV$, except for isolated cases of Fe^{2+} and Co^{4+} that incorporate $\Gamma = 0.9\ eV$, representing one of the effects caused by the absence of full multiplet effects.

5.2.1 Experimental comparison

The following results take into account the transition metal oxides that manifest the octahedral symmetry. Due to this, the structures present in the spectra are related to the contributions attributed to orbitals t_{2g} and e_g. Figures 58–62 showcase the comparison between the calculated and experimental spectra. The experimental data, obtained from a series of references [37, 39, 41, 129–131], were plotted within the original energy range and normalized intensity. The theoretical spectra were adjusted to align with the experimental measurements with a rigid rightward shift in relation to the energy axis.

However, it was done something different here from the $2p$-edge. In the previous section, an experimental comparison was made considering two types of theoretical spectra, the ionic and fully-converged. Although fully converged was maintained in the present section, also obeying the same electronic configuration used in the $2p$-edge discussion, where the following assumption was made: Given the consistency of the parameters and the study made throughout the $L_{2,3}$-edge, any change in values should reflect in the spectra. Since the spectra is designated as fully-converged, it should not change with extra ECs, which will be shown further in this section.

What has changed is the ionic spectrum. Since the ionic configuration is defined as the configuration in which there is no interaction between TM and O, it should not generate an $O\ 1s$ XAS spectrum. This is what happens, in fact, as will be shown in the theoretical details. Because of this, it becomes obvious that the covalence is of extreme importance for studying the $O\ 1s$-edge, as without it it would not be possible to obtain an absorption spectrum. So, to account for this, the experimental comparison is made by the comparison between experimental data with the fully-converged spectrum and the spectrum obtained considering the first configuration that makes it possible to include covalence into the calculations, or 2 ECs, denoted as *Covalence* 1^{st} *approx.*, or covalence first approximation. This is the same configuration used in the previous edge to explain why it is so important to consider extra electronic configurations to perform a more accurate study of the XAS technique.

Figure 58 presents the comparison between theoretical and experimental spectra [129, 130] for the manganese series is presented. The materials considered are MnO, Mn_2O_3, and $SrMnO_3$, representing the oxidation states $2+$, $3+$, and $4+$ of manganese, respectively. Despite the fact that the considered implementation does not consider full multiplet effects, the obtained results exhibit, in general, good agreement with the experimental data for both manganese oxides. Although the experimental spectrum of MnO appears somewhat rugged, there is an overall good agreement between the calculated and experimental data. The intensities of the structures related to the t_{2g} $(532\ eV)$ and e_g $(534\ eV)$ contributions in each graph are well reproduced. However, smaller peaks are not as well reproduced in the visual spectra as expected by their definition. It is important to note that, due to the exclusion of full multiplet effects in these calculations, not even the fully-converged spectra can fully replicate some subtle structures present in the experimental results, as seen in the case of MnO.

Concerning the covalence effects included into the calculations, when only the spectra related to the fully converged configuration are compared with the covalence first approximation, their difference becomes more and more discernible as the oxidation state of the manganese ion is increased. This already demonstrates a clear influence of covalence onto the results regarding the $O\ 1s$ edge XAS. However, when comparing them with the experimental data, a similar analysis to the one made in the $TM\ 2p$-edge can be done. For the less covalent compound, where the difference between theoretical spectra is less pronounced, it is more difficult to make such an affirmation regarding the covalence effects. But, as the nominal valence increases, it becomes visual that the spectra obtained considering ECs smaller than the converged one could not be able to reproduce the experimental data.

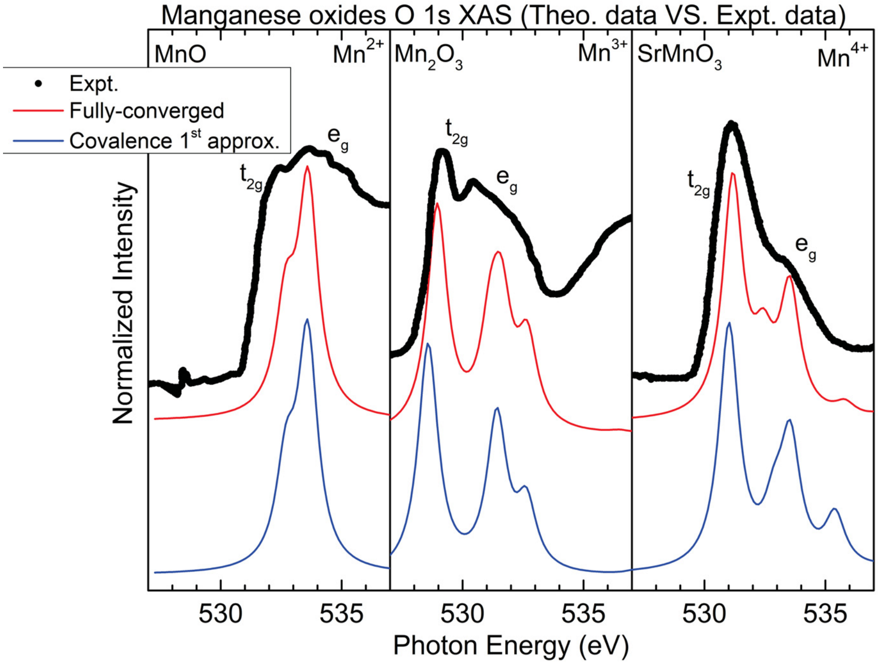

Figure 58 – Comparison of theoretical and experimental $O\ 1s$ X-ray absorption spectra for manganese ions (MnO [129], Mn_2O_3 [129] and $SrMnO_3$ [130]).

The comparison between theoretical and experimental data [37, 131] for the iron series is showcased in Figure 59. The materials considered are FeO, $LaFeO_3$ and $SrFeO_3$, formally corresponding to the nominal valences $2+$, $3+$, and $4+$ of iron. Similarly to manganese, the results are mostly positive in reproducing the $Fe\ 3d$ portion of the $O\ 1s$-edge XAS in all three cases, even with the lack of full multiplet effects. The major structures of t_{2g} $(530\ eV)$ and e_g $(532\ eV)$ peaks of the experimental spectra are better captured by the calculations of the fully-converged configuration.

Now, when comparing the fully-converged (red lines) and covalence first approximation (blue lines) spectra, like in the manganese series, their difference becomes more apparent as the oxidation state is increased. Like, for Fe^{2+} they are very similar, but for Fe^{4+} the blue one presents a very different format, where even the intensities of the peaks do not resembling the ones present in the red line. This again shows how the covalence can affect the outcomes of the employed technique, reinforcing the arguments proposed so far.

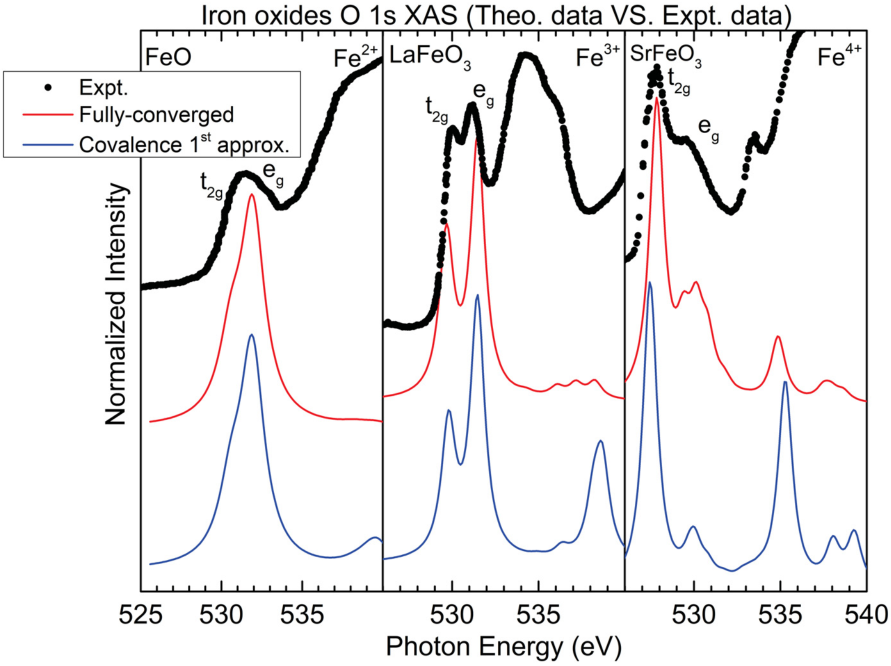

Figure 59 – Comparison of theoretical and experimental $O\ 1s$ X-ray absorption spectra for iron ions (FeO [131], $LaFeO_3$ [37] and $SrFeO_3$ [41]).

As for the cobalt series, the comparison between theoretical and experimental data [39, 41] of the $O\ 1s$ edge XAS is presented in Figure 60. The materials considered are CoO, $LiCoO_2$, and $SrCoO_3$, formally corresponding to the nominal valences $2+$, $3+$, and $4+$ of cobalt. Like in the previous metals, there is a good reproduction of the experimental data considering the position of the t_{2g} $(528\ eV)$ and e_g $(530\ eV)$ peaks and their format, showing that the implementation was well computed. Finally, comparing the two theoretical spectra, as in the two previous cases, for the less covalent ion (Co^{2+}) both theoretical spectra are very similar; however, as the oxidation state increases, they become more different, again proving the clear influence of not only the covalent aspect of each ion as the nominal valence is increased, but also the first approximation onto the calculations performed.

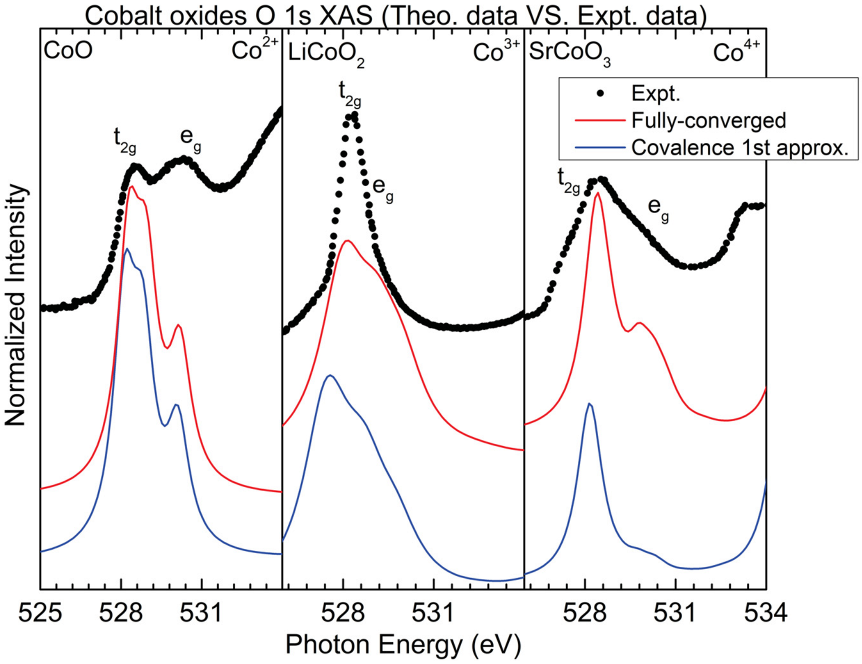

Figure 60 – Comparison of theoretical and experimental $O\ 1s$ X-ray absorption spectra for cobalt ions (CoO [39], $LiCoO_2$ [39] and $SrCoO_3$ [41]).

The consistency observed in the results presented in this section, similar to those in previous sections regarding the $TM\ 2p$-edge, underscores the parallel behavior and analogous analysis related to covalence. This consistent pattern further strengthens the arguments put forth in this work, emphasizing that covalence can indeed exert an influence on the outcomes of the X-ray absorption technique, irrespective of the specific portion of the electronic structure under analysis.

Now, let us examine whether symmetry reduction can affect the $O\ K$-edge, and be affected by covalence effects, similarly to the $TM\ L_{2,3}$-edge. The following results, presented in Figures 61 and 62, are related to the tetragonal and square pyramidal symmetries, as was mentioned in Chapter 4, they present the same unfolding of the states under crystal field effects, so as a consequence, the structures present in the spectra are related to contributions attributed to the orbitals e, b_2, a_1 and b_1.

Like in the previous section, let us start with Mn^{3+} in the D_{4h} symmetry. Unfortunately, no experimental $O\ K$-edge measurements are available for the compound $SrMn_{1-x}Mo_xO_3$ or, at least, for the specific molybdenum concentration required to exhibit the desired symmetry in the manganese cluster. As a result, only a visual comparison between the spectra of tetragonal and octahedral symmetries, in contrast to the experimental $O\ 1s$ data of $LaMnO_3$, is presented here in Figure 61. It is clearly visible the symmetry lowering effects when comparing side-by-side these results.

Although the intensities are more pronounced in the D_{4h} results, the energy positions of the e, b_2, a_1 and b_1 (around $529\ eV$ for the first two and $532\ eV$ for the last two) peaks closely resemble those of the octahedral symmetry (e_g and t_{2g}).

Also, when comparing between fully-converged (red lines) and covalence first approximation (blue lines) spectra, the D_{4h} spectra also present a small displacement, similar to O_h, in relation to the energy axis leftwards. Furthermore, they have differences in structure and format considering the a_1 and b_1 peaks mainly. Again, showing the influence of covalence on the results, which will be of great importance when, eventually, experimental data become available. It is worth noting the contrast with a similar comparison made for the $2p$ XAS of V^{5+}, where the reference O_h was very similar to the square pyramidal results, along with the experimental data. In the case of the $O\ 1s$ XAS of Mn^{3+}, this is not the case; the tetragonal results can be similar to the O_h ones, but they have their distinct differences caused by the symmetry reduction effects.

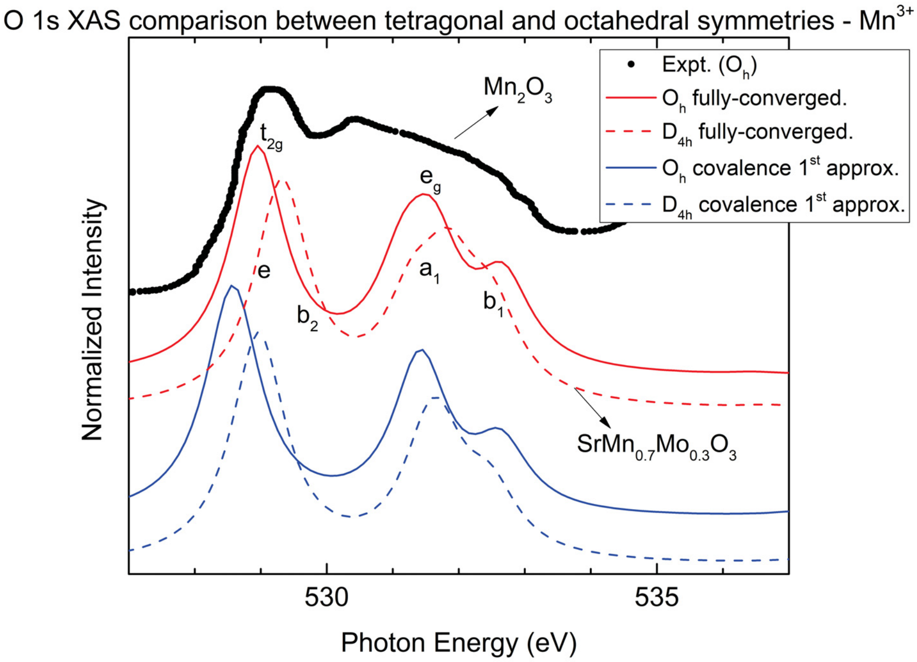

Figure 61 – Visual comparison between calculated $O\ 1s$ X-ray absorption spectra for tetragonal (no expt. data) and octahedral (Mn_2O_3 [129]) symmetries of Mn^{3+}.

At last, Figure 62 presents the comparison between the calculated and experimental spectra [64] with respect to the square pyramidal symmetry of V^{5+} as exemplified by vanadium pentoxide (V_2O_5) in its metallic phase [64]. One noticeable aspect of this comparison is the inversion of peak intensities in the calculated spectra, primarily attributed to the absence of full multiplet effects. Given the d^0 valence state of the material, the calculations are particularly sensitive to the parameter values. Despite the intensity discrepancy and also, lacking of the effects disregarded onto the implementation, the fully-converged spectrum exhibits good agreement in terms of energy positions with the experimental data be it with relation to the e and b_2 or a_1 and b_1 (around $530\ eV$ for the first two and $533\ eV$ for the last two) structures. When observing covalence effects, as on the $TM\ 2p$-edge, the high discrepancy between theoretical spectra can be attributed to the high covalent aspect of V^{5+}. In the first approximation spectrum (blue line), the peaks related to e, b_2, a_1 and b_1 are almost totally overlapped, making it not only discrepant in terms of the intensities, when compared to the experimental one, but also with the energy of the two regions. This once again underscores the persistent influence of covalence, regardless of changes in symmetry or technique, and reinforces what was already discussed in the $L_{2,3}$ section. It is noted that the covalence effects are not only considerably important when analyzing different types of spectra, but also necessary to perform more accurate reproductions of experimental data regarding the XAS technique, when applied to TMOs.

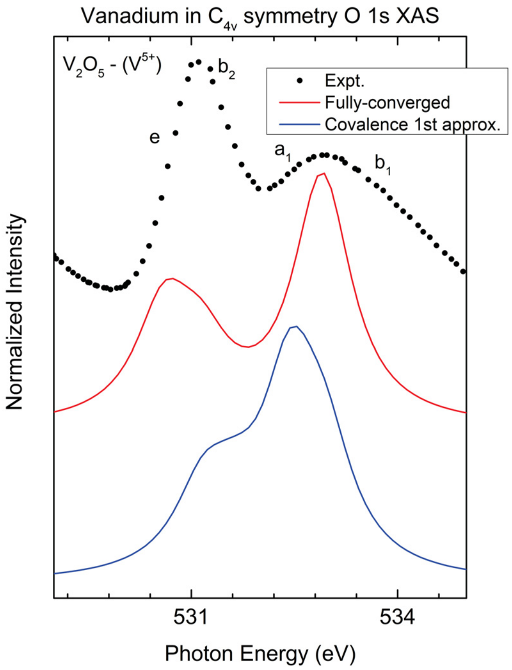

Figure 62 – Comparison between calculated and experimental (V_2O_5 [64]) $O\ 1s$ X-ray absorption spectra for V^{5+} in the square pyramidal symmetry.

5.2.2 Theoretical details

Following a similar organization used in the $TM\ L_{2,3}$-edge section, lets examine the results regarding theoretical details concerning the $O\ 1s$-edge XAS. This part of the discussion delves into the analysis of the $O\ 1s$ X-ray absorption spectra, computed using the MATLAB implementation [78] (refer to Chapter 2 and Appendix E for detailed methodology). The calculations presented in Figures 63–57 were carried out using the procedure explained at the beginning of the section. The spectra were plotted against the average energy related to the configuration energy, with a rigid shift along the intensity axis applied to enhance the clarity of the spectral shape evolution.

Figure 63 illustrates the $O\ 1s$ X-ray absorption spectra calculated for manganese ions, specifically Mn^{2+}, Mn^{3+}, and Mn^{4+}. The evolution of structures corresponding to the t_{2g} (around $-43\ eV$) and e_g (around $-41\ eV$) orbitals contributions is observable. One notable aspect is that their separation is not precisely equal to the crystal field parameter, attributable to the inclusion of covalence. Due to the implementation on which (refer to Appendix E) the local symmetry directly influences this. This observation provides additional evidence of the impact of covalence on the spectra. Another noteworthy point is that spectra related to the ionic state exhibit null intensities, indicating that there is no interaction between the transition metal and oxygen, aligning with expectations for this configuration. Additionally, similar to the $TM\ 2p$ X-ray absorption spectra, there is a discernible trend where an increase in the nominal valence corresponds to an increase in the number of electronic configurations capable of visually producing a spectrum with the approximated correct shape.

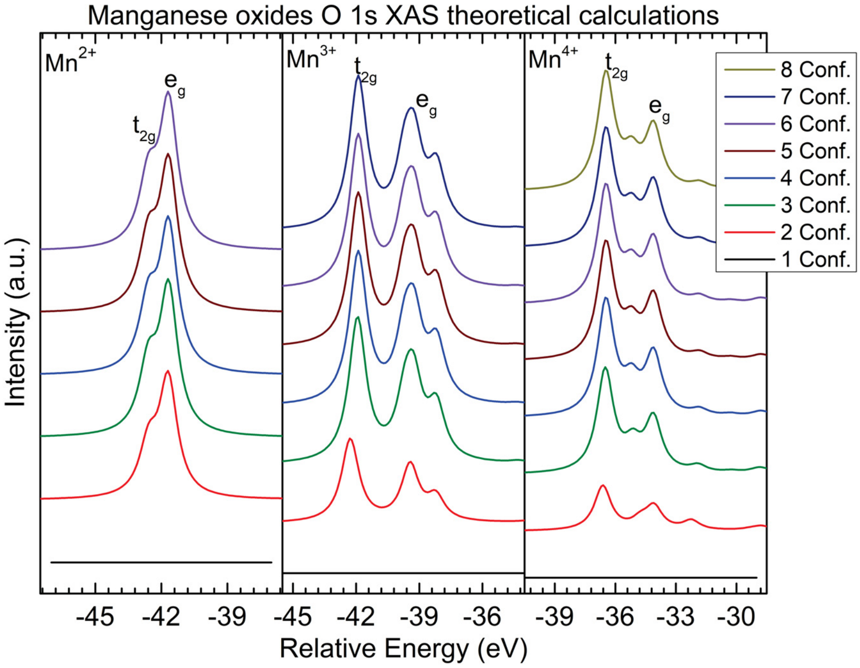

Figure 63 – $O\ 1s$ X-ray absorption spectra calculated for manganese ions (Mn^{2+}, Mn^{3+} and Mn^{4+}) using the *MATLAB* [78] implementation.

The $O\ 1s$ X-ray absorption spectra calculated for iron ions, namely Fe^{2+}, Fe^{3+} and Fe^{4+} are illustrated in Figure 64. Similarly to manganese, the evolution of the t_{2g} (around $-50\ eV$) and e_g (around $-52\ eV$) structures is evident as the number of electronic configurations increases. The ionic spectra also exhibit null intensity, consistent with expectations. Furthermore, the observed trend of requiring a higher number of electronic configurations for visual convergence as the nominal valence increases is repeated for iron as well.

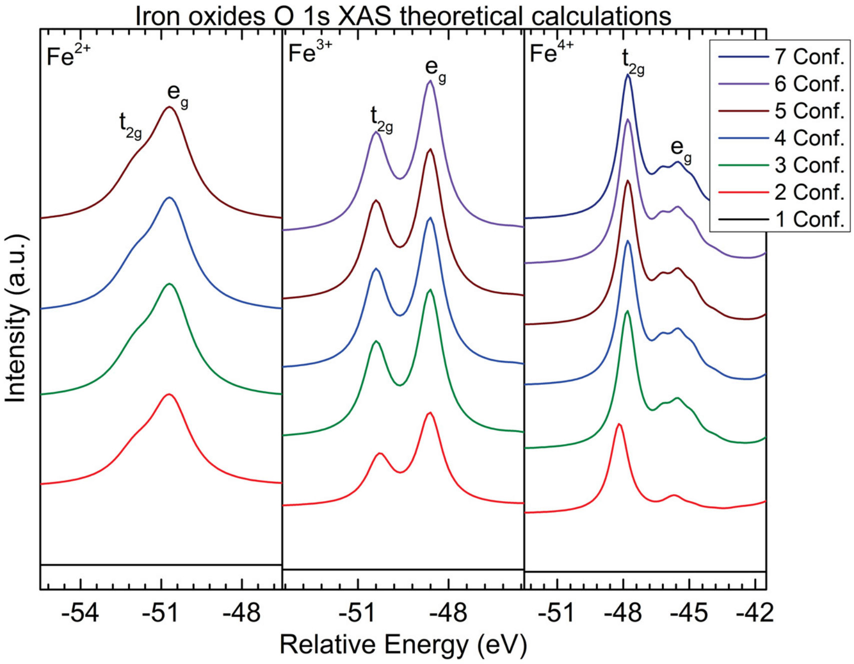

Figure 64 – $O\ 1s$ X-ray absorption spectra calculated for iron ions (Fe^{2+}, Fe^{3+} and Fe^{4+}) using the *MATLAB* [78] implementation.

For the cobalt series, the $O\ 1s$ X-ray absorption spectra calculated for Co^{2+}, Co^{3+}, and Co^{4+} are presented in Figure 65. In line with the previous systems, the results for the ionic state in the three oxidation states exhibit null intensities, consistent with expectations. The clear evolution of the spectral shapes related to t_{2g} (around $-45\ eV$) and e_g (around $-43\ eV$) orbitals as the oxidation state increases is evident. Furthermore, the convergence of the spectra is achieved only with an increase in the number of electronic configurations as the nominal valence rises. This reiterates the impact of the covalent aspect on the results, mirroring observations made in the $2p$ section.

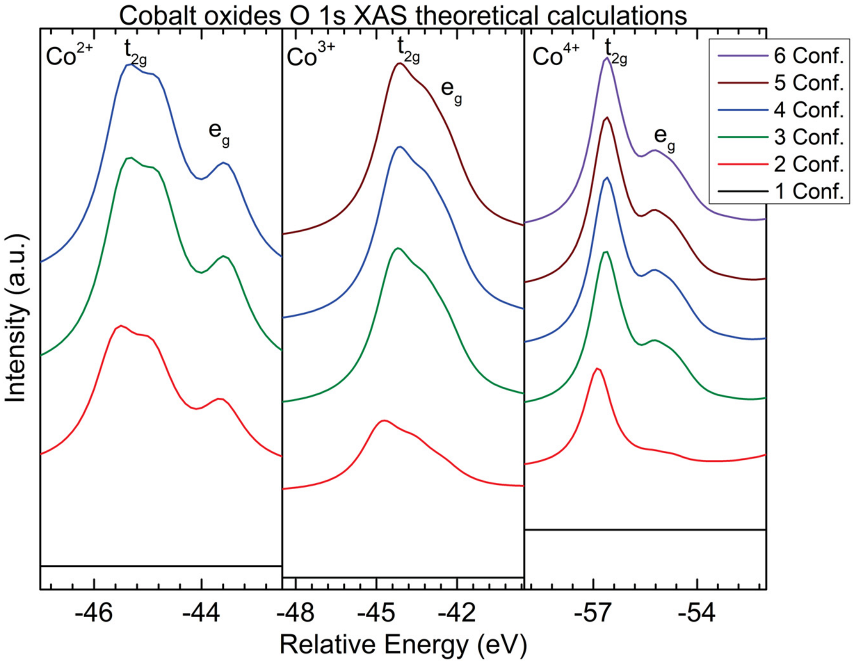

Figure 65 – $O\ 1s$ X-ray absorption spectra calculated for cobalt ions (Co^{2+}, Co^{3+} and Co^{4+}) using the *MATLAB* [78] implementation.

The examination of these theoretical results emphasizes once more the substantial influence of covalence, observed not only in the incorporation of more TM-O interactions but also in the metal atom itself through an elevation in the oxidation state. This corroborates the findings from the $L_{2,3}$ edge results, giving greater strength to the conclusions to be drawn. In the following, let us check if the theoretical observation made in the $2p$-edge can be brought to another portion of the ES. Starting with the analysis of the $O\ 1s$ XAS of Mn^{3+} in tetragonal symmetry. The cluster model calculations follow the same procedure presented for the O_h TM. Figure 66 reveals a spectral format and shape evolution similar to the octahedral case (Figure 63). Once again, the ionic spectrum is null, aligning with expectations. However, notable differences between O_h and D_{4h} symmetries arise in the structures related to the contributions a_1 and b_1 (around $-39\ eV$) in tetragonal symmetry and e_g (around $-41\ eV$) in the octahedral one. This variance in the theoretical spectra becomes more apparent compared to the $L_{2,3}$-edge results, emphasizing the sensitivity to symmetry changes. Another aspect is that it shows the clear degeneracy breaking shown in Figure 33. Where the e_g orbital was separated into a_1 and b_1 and t_{2g} separated into e and b_2 (around $-42\ eV$) in the D_{4h} symmetry. Examining the evolution of the spectra as the covalence between the transition metal and oxygen intensifies, a consistent rate of change, akin to the $2p$-edge of these materials, is evident. The spectrum related to 3 electronic configurations closely resembles those related to 6 or 7, indicating that, regardless of the symmetry alterations in the specific electronic structure segment analyzed, the covalence effects persist in both sets of results.

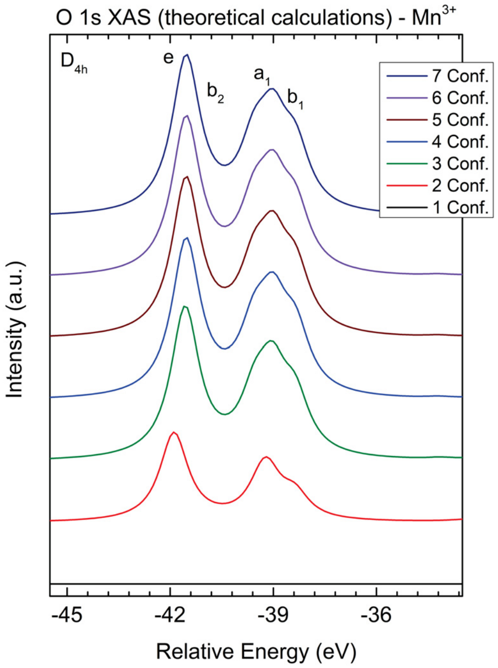

Figure 66 – $O\ 1s$ X-ray absorption spectra calculated for Mn^{3+} ion considering the tetragonal (D_{4h}) symmetry using the *MATLAB* [78] implementation.

Finally, let us examine the $O\ 1s$ XAS theoretical spectra of the vanadium ion, V^{5+}, which manifests square pyramidal symmetry (C_{4v}). Like in previous cases, the cluster model calculations were, as well, computed using the *MATLAB* [78] implementation and the same procedure as used in the previous simulations. Figure 67, as expected, shows that the ionic state spectrum is null. In line with expectations for a material with a higher oxidation state, a higher number of electronic configurations is required not just to initiate convergence toward the spectral format considering both structures related to e and b_2 or a_1 and b_1 (around $-7\ eV$ and $-5\ eV$, respectively), but also to achieve convergence as well. This underscores the persistence of covalence effects, regardless of the symmetry or the specific portion of the electronic structure under analysis.

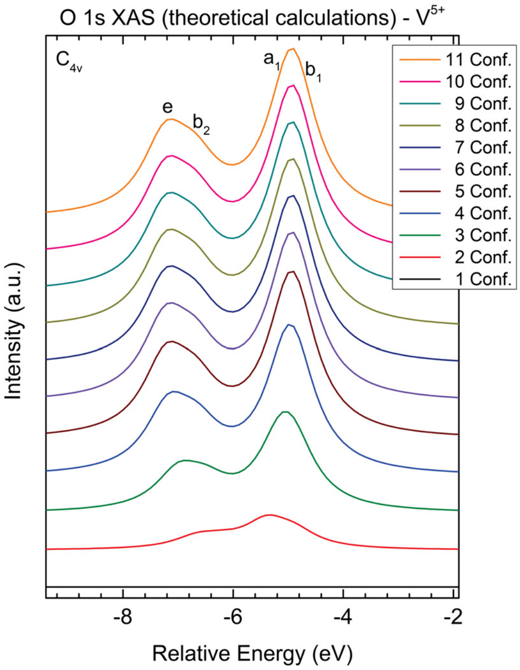

Figure 67 – $O\ 1s$ X-ray absorption spectra calculated for V^{5+} ion considering the square pyramidal (C_{4v}) symmetry using the *MATLAB* [78] implementation.

Through the analysis of this theoretical results it was possible to observe that, indeed, covalence have a clear influence under the outcomes of the XAS technique, regardless of symmetry considered (which have its own effects on the results) and portion of the electronic structure studied. What is interesting to note from this last analysis is that the assumption taken in the beginning of the section that the spectra should not change beyond the fully converged one, despite the increase in the number of electronic configurations, was proven to be accurate, since the stopping criterion used in the calculations of the $O\ 1s$ XAS theoretical spectra was the maximum number of ECs possible to consider in relation to the initial value of $3d$ band occupation for each TM studied in this work. Therefore, not only this discussion brought a better understanding of the ES of TMOs, a deep explanation of how covalence can influence the results of the spectroscopy technique used, but also technical aspects of the technique employed.

CHAPTER 6

Conclusions

This thesis delves into the intricacies of X-ray absorption spectroscopy applied to transition metal oxides with a particular focus on the $O\ 1s$ and $TM\ 2p$ edges. Through detailed calculations and comparisons with experimental data, we aimed to unravel the impact of covalence and symmetry effects on the accuracy and reliability of XAS results. Originally, the transition metals studied were only manganese (Mn), iron (Fe) and cobalt (Co), but as interest in reducing symmetry arose, it was necessary to include one more, vanandium (V). It helped to make even more stronger the argumentation on how the covalence and symmetry lowering, even in the same metal, can affect the results of this technique. By implementing the cluster model computationally, it was possible to account for a gamma of effects that can influence the results of X-ray absorption, be it by considering the full multiplet effects in the $2p$-edge, or making an approximation of not so trivial transitions in the $O\ 1s$-edge.

An overarching theme that emerged from the investigations is the undeniable influence of covalence on the XAS spectra of TMOs. Regardless of the oxidation state, symmetry, or the specific electronic structure being analyzed, the inclusion of covalent interactions proved crucial for achieving agreement between theoretical calculations and experimental observations.

The $2p$-edge XAS results underscored the significance of covalence not only in reproducing the experimental spectra accurately. But also, studies of effects on different types of information extracted from the GS of each TM studied. The analysis of the electronic contributions made it possible to verify the covalent (low or high) character of each metal and how the increase in the nominal valence influences this directly. It was also possible to check the data regarding the spin-states of each material in relation to what was introduced in the chapter 4. In addition to this, energy and $3d$ electron count values were used to verify not only the covalent behavior of high oxidation state ions, such as Mn^{4+}, Fe^{4+} and V^{5+}, regardless of the symmetry they present. But to start the study considering the covalence between TM and the ligand O, this helped to prove that this covalence highly influences the outcomes with respect to the XAS technique.

Examining the manganese, iron and cobalt series, along with the vanadium ion results, a consistent trend was revealed: As the oxidation state increased, there was not just a tendency but a necessity to increase the number of ECs to obtain the fully-converged configuration. Although the addition of these extra ECs to the simulation is highly expensive computationally, since this represents an increase on the size of the basis that describes the studied system, it was shown to not be something merely cosmetic. In fact, it is a necessary "evil" for the sake of a more precise study of the properties treated in this thesis.

Moving to the $O\ 1s$ edge, the analysis reinforced the omnipresence of the covalence effect. From manganese to vanadium series, the evolution of the XAS spectra mirrored the $2p$-edge findings. The inclusion of more electronic configurations became imperative to capture the subtle nuances present in the experimental data. Even in reduced symmetry cases, such as tetragonal and square pyramidal, covalence continued to play a pivotal role. In addition to covalence, the study addressed the impact of reduced symmetry on the XAS results. Analyzing Mn^{3+} in tetragonal and V^{5+} in square pyramidal symmetry, distinct changes in spectral structures, intensities, and shifts were observed compared to octahedral symmetry. While these variations were expected, they highlighted the importance of adapting theoretical models to the specific symmetry of the TMO under investigation to properly obtain the desired results.

This investigation sheds light on the nuanced interplay of covalence and symmetry in the XAS of TMOs. Achieving a comprehensive understanding of these materials requires meticulous consideration of both factors. The consistent patterns observed in different transition metals and oxidation states underscore the generalizability of the findings. In conclusion, this study not only enhances the accuracy of theoretical predictions in XAS but also provides valuable insights for interpreting experimental spectra. This work contributes to the ongoing discussion surrounding the intricacies of transition metal oxides and sets the stage for further refinements in theoretical models and experimental techniques such as X-ray absorption spectroscopy.

BIBLIOGRAPHY

1 CHALK, S.; MCEWEN, L. An Exemplar for IUPAC Asset Digitization. **Chemistry International**, v. 39, n. 3, p. 25–30, 2017. DOI: `doi:10.1515/ci-2017-0307`. Available from: https://doi.org/10.1515/ci-2017-0307. Cit. on p. 20.

2 JENSEN, W. B. The place of zinc, cadmium, and mercury in the periodic table. **Journal of Chemical Education**, ACS Publications, v. 80, n. 8, p. 952, 2003. Cit. on p. 20.

3 TABLE, T. P. **Periodic Table of the Elements**. Adapted from source. 2023. Available from: https://www.periodictable.co.za/#google_vignette. Cit. on p. 21.

4 FRATI, F.; HUNAULT, M. O.; DE GROOT, F. M. Oxygen K-edge X-ray absorption spectra. **Chemical reviews**, ACS Publications, v. 120, n. 9, p. 4056–4110, 2020. Cit. on pp. 22, 36, 37, 56, 57.

5 LIAO, Z.; ZHANG, J. Metal-to-insulator transition in ultrathin manganite heterostructures. **Applied Sciences**, MDPI, v. 9, n. 1, p. 144, 2019. Cit. on p. 23.

6 COX, P. A. **Transition metal oxides: an introduction to their electronic structure and properties**. [S.l.]: Oxford university press, 2010. v. 27. Cit. on p. 23.

7 MATTHEISS, L. F. Band Structure and Fermi Surface of ReO_3. **Phys. Rev.**, American Physical Society, v. 181, p. 987–1000, 3 May 1969. DOI:

10.1103/PhysRev.181.987. Available from: https://link.aps.org/doi/10.1103/PhysRev.181.987. Cit. on p. 23.

8 MORIN, F. J. Oxides Which Show a Metal-to-Insulator Transition at the Neel Temperature. **Phys. Rev. Lett.**, American Physical Society, v. 3, p. 34–36, 1 July 1959. DOI: 10.1103/PhysRevLett.3.34. Available from: https://link.aps.org/doi/10.1103/PhysRevLett.3.34. Cit. on p. 23.

9 MATTHEISS, L. F. Energy Bands for KNiF$_3$, SrTiO$_3$, KMoO$_3$, and KTa$_3$. **Phys. Rev. B**, American Physical Society, v. 6, p. 4718–4740, 12 Dec. 1972. DOI: 10.1103/PhysRevB.6.4718. Available from: https://link.aps.org/doi/10.1103/PhysRevB.6.4718. Cit. on p. 23.

10 FUKUSHIMA, A.; IGA, F.; INOUE, I. H.; MURATA, K.; NISHIHARA, Y. Annealing Effects on Transport and Magnetic Properties of Perovskite-Type Vanadium Oxide CaVO$_3$. **Journal of the Physical Society of Japan**, v. 63, n. 2, p. 409–412, 1994. DOI: 10.1143/JPSJ.63.409. Available from: https://doi.org/10.1143/JPSJ.63.409. Cit. on p. 23.

11 MORIN, F. J. Electrical Properties of NiO. **Phys. Rev.**, American Physical Society, v. 93, p. 1199–1204, 6 Mar. 1954. DOI: 10.1103/PhysRev.93.1199. Available from: https://link.aps.org/doi/10.1103/PhysRev.93.1199. Cit. on p. 23.

12 BOCQUET, A. E.; FUJIMORI, A.; MIZOKAWA, T.; SAITOH, T.; NAMATAME, H.; SUGA, S.; KIMIZUKA, N.; TAKEDA, Y.; TAKANO, M. Electronic structure of SrFe^{4+}O$_3$ and related Fe perovskite oxides. **Phys. Rev. B**, American Physical Society, v. 45, p. 1561–1570, 4 Jan. 1992. DOI: 10.1103/PhysRevB.45.1561. Available from: https://link.aps.org/doi/10.1103/PhysRevB.45.1561. Cit. on p. 23.

13 BEDNORZ, J. G.; MÜLLER, K. A. Possible high T$_c$ superconductivity in the Ba-La-Cu-O system. **Zeitschrift fur Physik B Condensed Matter**, v. 64, p. 189–193, June 1986. DOI: 10.1007/BF01303701. Cit. on p. 23.

14 JIN, S.; TIEFEL, T. H.; MCCORMACK, M.; FASTNACHT, R. A.; RAMESH, R.; CHEN, L. H. Thousandfold Change in Resistivity in Magnetoresistive La-Ca-Mn-O Films. **Science**, v. 264, n. 5157, p. 413–415, 1994. DOI: 10.1126/science.264.5157.413. Available from: https://www.science.org/doi/abs/10.1126/science.264.5157.413. Cit. on p. 23.

15 DRUDE, P. Zur elektronentheorie der metalle. **Annalen der physik**, Wiley Online Library, v. 306, n. 3, p. 566–613, 1900. Cit. on p. 24.

16 _______. Zur elektronentheorie der metalle; II. Teil. galvanomagnetische und thermomagnetische effecte. **Annalen der physik**, Wiley Online Library, v. 308, n. 11, p. 369–402, 1900. Cit. on p. 24.

17 WILSON, A. H. The theory of electronic semi-conductors. **Proceedings of the Royal Society of London. Series A, Containing Papers of a Mathematical and Physical Character**, The Royal Society London, v. 133, n. 822, p. 458–491, 1931. Cit. on p. 24.

18 _______. The theory of electronic semi-conductors.-ii. **Proceedings of the Royal Society of London. Series A, Containing Papers of a Mathematical and Physical Character**, The Royal Society London, v. 134, n. 823, p. 277–287, 1931. Cit. on p. 24.

19 BOER, J. H. de; VERWEY, E. J. Semi-conductors with partially and with completely filled 3d-lattice bands. **Proceedings of the Physical Society**, IOP Publishing, v. 49, 4S, p. 59, 1937. Cit. on p. 25.

20 MOTT, N.; PEIERLS, R. Discussion of the paper by de Boer and Verwey. **Proceedings of the Physical Society**, IOP Publishing, v. 49, 4S, p. 72, 1937. Cit. on p. 25.

21 PHYSICS, I. of; PHYSICAL SOCIETY, the. **Proceedings of the Physical Society**. [S.l.]: Institute of Physics and the Physical Society., 1876. v. 1. Cit. on p. 25.

22 MOTT, N. On the transition to metallic conduction in semiconductors. **Canadian journal of physics**, NRC Research Press Ottawa, Canada, v. 34, 12A, p. 1356–1368, 1956. Cit. on p. 25.

23 MOTT, N. F. The transition to the metallic state. **Philosophical Magazine**, Taylor & Francis, v. 6, n. 62, p. 287–309, 1961. Cit. on p. 25.

24 HUBBARD, J.; FLOWERS, B. Proceedings of the Royal Society of London, Series A. **Math. Phys. Sci.**, v. 276, n. 1365, p. 238, 1963. Cit. on p. 25.

25 ANDERSON, P. W. Localized magnetic states in metals. **Physical Review**, APS, v. 124, n. 1, p. 41, 1961. Cit. on p. 25.

26 OKADA, K.; KOTANI, A. Nonlocal screening effects on core-level photoemission spectra investigated by large-cluster models. **Physical Review B**, APS, v. 52, n. 7, p. 4794, 1995. Cit. on p. 25.

27 VAN VEENENDAAL, M.; SAWATZKY, G. Nonlocal screening effects in 2p x-ray photoemission spectroscopy core-level line shapes of transition metal compounds. **Physical Review Letters**, APS, v. 70, n. 16, p. 2459, 1993. Cit. on p. 25.

28 FUJIMORI, A.; MINAMI, F. Valence-band photoemission and optical absorption in nickel compounds. **Physical Review B**, APS, v. 30, n. 2, p. 957, 1984. Cit. on pp. 25, 50.

29 VAN DER LAAN, G.; WESTRA, C.; HAAS, C.; SAWATZKY, G. Satellite structure in photoelectron and Auger spectra of copper dihalides. **Physical Review B**, APS, v. 23, n. 9, p. 4369, 1981. Cit. on pp. 25, 50.

30 WENTZCOVITCH, R. M.; SCHULZ, W. W.; ALLEN, P. B. VO_2: Peierls or Mott-Hubbard? A view from band theory. **Physical review letters**, APS, v. 72, n. 21, p. 3389, 1994. Cit. on p. 25.

31 CARUTHERS, E.; KLEINMAN, L. Energy Bands of Semiconducting VO_2. **Physical Review B**, APS, v. 7, n. 8, p. 3760, 1973. Cit. on p. 25.

32 DE GROOT, F.; KOTANI, A. **Core level spectroscopy of solids**. [S.l.]: CRC press, 2008. Cit. on pp. 25–28, 32–36, 42–45, 124, 125, 132, 141.

33 SPECTROSCOPY. [S.l.: s.n.]. `https://www.pasco.com/products/guides/what-is-spectroscopy`. Accessed: 25/01/2024. Cit. on pp. 26, 27.

34 LINDBERG, C. A.; GRACE, A. The Oxford American college dictionary. **GP Putnam's Sons: New York, NY, USA**, 2002. Cit. on p. 26.

35 CHU, S.; HURST, G. S.; GRAYBEAL, J. D.; STONER, J. O. spectroscopy. In: ENCYCLOPEDIA Britannica. [S.l.: s.n.], Jan. 2024. Cit. on p. 26.

36 HAVERKORT, M. W. Spin and orbital degrees of freedom in transition metal oxides and oxide thin films studied by soft x-ray absorption spectroscopy. **arXiv preprint cond-mat/0505214**, 2005. Cit. on p. 28.

37 ABBATE, M.; GROOT, F. M. de; FUGGLE, J.; FUJIMORI, A.; STREBEL, O.; LOPEZ, F.; DOMKE, M.; KAINDL, G.; SAWATZKY, G.; TAKANO, M., et al. Controlled-valence properties of La$_{1-x}$Sr$_x$FeO$_3$ and La$_{1-x}$Sr$_{x]}$MnO$_3$ studied by soft-x-ray absorption spectroscopy. **Physical Review B**, APS, v. 46, n. 8, p. 4511, 1992. Cit. on pp. 29, 52, 60, 67–70, 73, 91, 93, 94.

38 LEE, H.; KIM, G.; KANG, J.-S.; DABROWSKI, B.; HAN, S.; LEE, S.; HWANG, C.; JUNG, M.; SHIN, H.; LEE, H., et al. Valence states of transition-metal ions in cubic perovskites SrMn$_{1-x}$Fe$_x$O$_3$. **Journal of applied physics**, AIP Publishing, v. 101, n. 9, 2007. Cit. on pp. 29, 67, 68, 70.

39 DE GROOT, F.; ABBATE, M.; VAN ELP, J.; SAWATZKY, G.; MA, Y.; CHEN, C.; SETTE, F. Oxygen 1s and cobalt 2p X-ray absorption of cobalt oxides. **Journal of Physics: Condensed Matter**, IOP Publishing, v. 5, n. 14, p. 2277, 1993. Cit. on pp. 29, 52, 67, 68, 70, 71, 91, 94, 95.

40 MONTORO, L.; ABBATE, M.; ALMEIDA, E.; ROSOLEN, J. M. Electronic structure of the transition metal ions in LiCoO$_2$, LiNiO$_2$ and LiCo$_{0.5}$Ni$_{0.5}$O$_2$. **Chemical Physics Letters**, Elsevier, v. 309, n. 1-2, p. 14–18, 1999. Cit. on pp. 29, 67, 68, 70, 71.

41 ABBATE, M.; ZAMPIERI, G.; OKAMOTO, J.; FUJIMORI, A.; KAWASAKI, S.; TAKANO, M. X-ray absorption of the negative charge-transfer material SrFe$_{1-x}$Co$_x$O$_3$. **Physical Review B**, APS, v. 65, n. 16, p. 165120, 2002. Cit. on pp. 29, 52, 60, 62, 67, 68, 70, 71, 91, 94, 95.

42 LEE, J.; KIM, B.; KIM, B.; MIN, B.; KOLESNIK, S.; CHMAISSEM, O.; MAIS, J.; DABROWSKI, B.; SHIN, H.; KIM, D., et al. Valence-state transition in SrMn$_{1-x}$Mo$_x$O$_3$ (0≤x≤0.5) investigated by soft x-ray absorption spectroscopy. **Physical Review B**, APS, v. 80, n. 20, p. 205112, 2009. Cit. on pp. 29, 30, 58, 62, 63, 67, 72, 73.

43 COWAN, R. D. **The theory of atomic structure and spectra**. [S.l.]: Univ of California Press, 2023. v. 3. Cit. on pp. 30, 44, 131, 132.

44 CROCOMBETTE, J.; POLLAK, M.; JOLLET, F.; THROMAT, N.; GAUTIER-SOYER, M. X-ray-absorption spectroscopy at the Fe $L_{2,3}$ threshold in iron oxides. **Physical Review B**, APS, v. 52, n. 5, p. 3143, 1995. Cit. on pp. 30, 42, 58.

45 VERCAMER, V.; HUNAULT, M. O.; LELONG, G.; HAVERKORT, M. W.; CALAS, G.; ARAI, Y.; HIJIYA, H.; PAULATTO, L.; BROUDER, C.; ARRIO, M.-A., et al. Calculation of optical and K pre-edge absorption spectra for ferrous iron of distorted sites in oxide crystals. **Physical Review B**, APS, v. 94, n. 24, p. 245115, 2016. Cit. on p. 30.

46 ATTWOOD, D. **Soft x-rays and extreme ultraviolet radiation: principles and applications**. [S.l.]: Cambridge university press, 2000. Cit. on p. 32.

47 ULFLUND. **The wavelengths and photon energies of X-rays and a few applications of X-rays**. File:X-ray applications.svg. 2012. Available from: https://en.wikipedia.org/wiki/File:X-ray_applications.svg. Cit. on p. 32.

48 GOEL A, e. a. **Photoelectric effect**. Adapted from source. 2014. Available from: https://radiopaedia.org/articles/29684. Cit. on p. 33.

49 _______. **Compton effect**. Adapted from source. 2014. Available from: https://radiopaedia.org/articles/30308. Cit. on p. 33.

50 CHAN, T.; LIU, R.; GUO, G.; HU, S.-F.; LIN, J.; CHEN, J.; CHANG, C.-R. Effects of B-site transition metal on the properties of double perovskites Sr_2FeMO_6 (M= Mo, W): B 4d–5d system. **Solid state communications**, Elsevier, v. 133, n. 4, p. 265–270, 2005. Cit. on pp. 36, 37, 42.

51 GROOT, F. M. de; ELNAGGAR, H.; FRATI, F.; WANG, R.-p.; DELGADO-JAIME, M. U.; VEENENDAAL, M. van; FERNANDEZ-RODRIGUEZ, J.; HAVERKORT, M. W.; GREEN, R. J.; DER LAAN, G. van, et al. 2p x-ray absorption spectroscopy of 3d transition metal systems. **Journal of Electron Spectroscopy and Related Phenomena**, Elsevier, v. 249, p. 147061, 2021. Cit. on pp. 36, 42, 67.

52 ZAANEN, J.; SAWATZKY, G.; ALLEN, J. Band gaps and electronic structure of transition-metal compounds. **Physical review letters**, APS, v. 55, n. 4, p. 418, 1985. Cit. on pp. 38, 39, 52, 84.

53 ZAANEN, J.; SAWATZKY, G. The electronic structure and superexchange interactions in transition-metal compounds. **Canadian journal of physics**, NRC Research Press Ottawa, Canada, v. 65, n. 10, p. 1262–1271, 1987. Cit. on pp. 38, 39.

54 ASHCROFT, N.; MERMIN, N. **Solid State Physics**. [S.l.]: Cengage Learning, 2011. ISBN 9788131500521. Cit. on p. 38.

55 ZAANEN, J.; SAWATZKY, G. Systematics in band gaps and optical spectra of 3D transition metal compounds. **Journal of solid state chemistry**, Elsevier, v. 88, n. 1, p. 8–27, 1990. Cit. on p. 39.

56 MIZOKAWA, T.; NAMATAME, H.; FUJIMORI, A.; AKEYAMA, K.; KONDOH, H.; KURODA, H.; KOSUGI, N. Origin of the band gap in the negative charge-transfer-energy compound $NaCuO_2$. **Physical review letters**, APS, v. 67, n. 12, p. 1638, 1991. Cit. on pp. 39, 60.

57 HAVERKORT, M.; ZWIERZYCKI, M.; ANDERSEN, O. Multiplet ligand-field theory using Wannier orbitals. **Physical Review B**, APS, v. 85, n. 16, p. 165113, 2012. Cit. on pp. 42, 51, 77, 81–84, 89, 90, 154.

58 SLATER, J. C. The theory of complex spectra. **Physical Review**, APS, v. 34, n. 10, p. 1293, 1929. Cit. on p. 42.

59 CONDON, E. U.; SHORTLEY, G. H. **The theory of atomic spectra**. [S.l.]: Cambridge University Press, 1951. Cit. on p. 42.

60 BRANDOW, B. Electronic structure of Mott insulators. **Advances in Physics**, Taylor & Francis, v. 26, n. 5, p. 651–808, 1977. Cit. on p. 44.

61 KANAMORI, J. Electron correlation and ferromagnetism of transition metals. **Progress of Theoretical Physics**, Oxford University Press, v. 30, n. 3, p. 275–289, 1963. Cit. on p. 44.

62 GRIFFITH, J. S. **The theory of transition-metal ions**. [S.l.]: Cambridge university press, 1961. Cit. on pp. 45, 46, 133, 136.

63 FAZZIO, A.; WATARI, K. **Introdução à teoria de grupos com aplicações em moléculas e sólidos**. [S.l.: s.n.], 2009. Cit. on pp. 46, 146–151, 153.

64 MOSSANEK, R.; MOCELLIN, A.; ABBATE, M.; SEARLE, B.; FONSECA, P.; MORIKAWA, E. Cluster model and band structure calculations of V_2O_5: Reduced V^{5+} symmetry and many-body effects. **Physical Review B**, APS, v. 77, n. 7, p. 075118, 2008. Cit. on pp. 46, 52, 64, 66, 67, 74, 75, 84, 96, 97, 144.

65 VAN ELP, J.; WIELAND, J.; ESKES, H.; KUIPER, P.; SAWATZKY, G.; DE GROOT, F.; TURNER, T. Electronic structure of CoO, Li-doped CoO, and $LiCoO_2$. **Physical Review B**, APS, v. 44, n. 12, p. 6090, 1991. Cit. on pp. 46, 47, 52.

66 VAN ELP, J.; ESKES, H.; KUIPER, P.; SAWATZKY, G. Electronic structure of Li-doped NiO. **Physical Review B**, APS, v. 45, n. 4, p. 1612, 1992. Cit. on p. 46.

67 FUJIMORI, A.; MINAMI, F.; SUGANO, S. Multielectron satellites and spin polarization in photoemission from Ni compounds. **Physical Review B**, APS, v. 29, n. 9, p. 5225, 1984. Cit. on p. 49.

68 SLATER, J. C.; KOSTER, G. F. Simplified LCAO method for the periodic potential problem. **Physical review**, APS, v. 94, n. 6, p. 1498, 1954. Cit. on pp. 49, 161, 163.

69 HUBBARD, J.; RIMMER, D.; HOPGOOD, F. Weak covalency in transition metal salts. **Proceedings of the Physical Society**, IOP Publishing, v. 88, n. 1, p. 13, 1966. Cit. on p. 50.

70 BOCQUET, A.; MIZOKAWA, T.; MORIKAWA, K.; FUJIMORI, A.; BARMAN, S.; MAITI, K.; SARMA, D.; TOKURA, Y.; ONODA, M. Electronic structure of early 3d-transition-metal oxides by analysis of the 2p core-level photoemission spectra. **Physical Review B**, APS, v. 53, n. 3, p. 1161, 1996. Cit. on pp. 50, 56.

71 BOCQUET, A.; MIZOKAWA, T.; SAITOH, T.; NAMATAME, H.; FUJIMORI, A. Electronic structure of 3d-transition-metal compounds by analysis of the 2p core-level photoemission spectra. **Physical Review B**, APS, v. 46, n. 7, p. 3771, 1992. Cit. on pp. 51, 52, 56, 58, 60, 61.

72 DACOSTA, H.; MAOHONG, F. **Rate constant calculation for thermal reactions**. [S.l.]: Wiley Online Library, 2011. Cit. on p. 51.

73 METCALF, R. **Constituent Partitioning Consensus Docking Models and Application in Drug Discovery**. [S.l.]: University of South Florida, 2019. Cit. on p. 51.

74 MAURICE, D.; HEAD-GORDON, M. Analytical second derivatives for excited electronic states using the single excitation configuration interaction method: theory and application to benzo [a] pyrene and chalcone. **Molecular Physics**, Taylor & Francis, v. 96, n. 10, p. 1533–1541, 1999. Cit. on p. 51.

75 PURVIS III, G. D.; BARTLETT, R. J. A full coupled-cluster singles and doubles model: The inclusion of disconnected triples. **The Journal of Chemical Physics**, American Institute of Physics, v. 76, n. 4, p. 1910–1918, 1982. Cit. on p. 51.

76 RAGHAVACHARI, K.; TRUCKS, G. W.; POPLE, J. A.; HEAD-GORDON, M. A fifth-order perturbation comparison of electron correlation theories. **Chemical Physics Letters**, Elsevier, v. 157, n. 6, p. 479–483, 1989. Cit. on p. 51.

77 VAN VOORHIS, T.; HEAD-GORDON, M. Two-body coupled cluster expansions. **The Journal of Chemical Physics**, American Institute of Physics, v. 115, n. 11, p. 5033–5040, 2001. Cit. on p. 51.

78 INC., T. M. **MATLAB version: 9.13.0 (R2022b)**. Natick, Massachusetts, United States: The MathWorks Inc., 2022. Available from: https://www.mathworks.com. Cit. on pp. 51, 91, 97–102, 162.

79 MOSSANEK, R.; ABBATE, M. Cluster model calculations with nonlocal screening channels of metallic and insulating VO_2. **Physical Review B**, APS, v. 74, n. 12, p. 125112, 2006. Cit. on p. 52.

80 POTZE, R.; SAWATZKY, G.; ABBATE, M. Possibility for an intermediate-spin ground state in the charge-transfer material $SrCoO_3$. **Physical Review B**, APS, v. 51, n. 17, p. 11501, 1995. Cit. on pp. 52, 62.

81 SAITOH, T.; BOCQUET, A.; MIZOKAWA, T.; FUJIMORI, A. Systematic variation of the electronic structure of 3d transition-metal compounds. **Physical Review B**, APS, v. 52, n. 11, p. 7934, 1995. Cit. on p. 52.

82 VAN ELP, J.; POTZE, R.; ESKES, H.; BERGER, R.; SAWATZKY, G. Electronic structure of MnO. **Physical Review B**, APS, v. 44, n. 4, p. 1530, 1991. Cit. on p. 52.

83 MOMMA, K.; IZUMI, F. VESTA: a three-dimensional visualization system for electronic and structural analysis. **Journal of Applied crystallography**, International Union of Crystallography, v. 41, n. 3, p. 653–658, 2008. Cit. on pp. 56–63.

84 HORTON, M. K.; MONTOYA, J. H.; LIU, M.; PERSSON, K. A. High-throughput prediction of the ground-state collinear magnetic order of inorganic materials using density functional theory. **npj Computational Materials**, Nature Publishing Group UK London, v. 5, n. 1, p. 64, 2019. Cit. on p. 56.

85 GREENWOOD, N. N.; EARNSHAW, A. **Chemistry of the Elements**. [S.l.]: Elsevier, 2012. Cit. on p. 56.

86 SATPATHY, S.; POPOVIĆ, Z. S.; VUKAJLOVIĆ, F. R. Electronic structure of the perovskite oxides: La$_{1-x}Ca_x$MnO$_3$. **Physical review letters**, APS, v. 76, n. 6, p. 960, 1996. Cit. on p. 56.

87 ELEMANS, J. B.; VAN LAAR, B.; VAN DER VEEN, K.; LOOPSTRA, B. The crystallographic and magnetic structures of La$_{1-x}$Ba$_x$Mn$_{1-x}$Me$_x$O$_3$ (Me= Mn or Ti). **Journal of solid state chemistry**, Elsevier, v. 3, n. 2, p. 238–242, 1971. Cit. on p. 56.

88 GOODENOUGH, J. B. Theory of the role of covalence in the perovskite-type manganites [La, M(II)] MnO$_3$. **Physical Review**, APS, v. 100, n. 2, p. 564, 1955. Cit. on p. 56.

89 WOLLAN, E.; KOEHLER, W. Neutron diffraction study of the magnetic properties of the series of perovskite-type Compounds [(1-x) La, xCa] MnO$_3$. **Physical Review**, APS, v. 100, n. 2, p. 545, 1955. Cit. on p. 56.

90 GHOSH, S. K. Diversity in the family of manganese oxides at the nanoscale: from fundamentals to applications. **ACS omega**, ACS Publications, v. 5, n. 40, p. 25493–25504, 2020. Cit. on p. 57.

91 RAHAMAN, H.; LAHA, R. M.; MAITI, D. K.; GHOSH, S. K. Fabrication of Mn_2O_3 nanorods: an efficient catalyst for selective transformation of alcohols to aldehydes. **RSC Advances**, Royal Society of Chemistry, v. 5, n. 43, p. 33923–33929, 2015. Cit. on p. 57.

92 YAMANAKA, T.; NAGAI, T.; OKADA, T.; FUKUDA, T. Structure change of Mn_2O_3 under high pressure and pressure-induced transition. **Zeitschrift für Kristallographie-Crystalline Materials**, De Gruyter Oldenbourg, v. 220, n. 11, p. 938–945, 2005. Cit. on p. 57.

93 GILBERT, B.; FRAZER, B.; BELZ, A.; CONRAD, P.; NEALSON, K.; HASKEL, D.; LANG, J.; SRAJER, G.; DE STASIO, G. Multiple scattering calculations of bonding and X-ray absorption spectroscopy of manganese oxides. **The Journal of Physical Chemistry A**, ACS Publications, v. 107, n. 16, p. 2839–2847, 2003. Cit. on p. 57.

94 SØNDENÅ, R.; RAVINDRAN, P.; STØLEN, S.; GRANDE, T.; HANFLAND, M. Electronic structure and magnetic properties of cubic and hexagonal $SrMnO_3$. **Physical Review B**, APS, v. 74, n. 14, p. 144102, 2006. Cit. on p. 58.

95 SYONO, Y.; AKIMOTO, S.-i.; KOHN, K. Structure relations of hexagonal perovskite-like compounds ABX_3 at high pressure. **Journal of the Physical Society of Japan**, The Physical Society of Japan, v. 26, n. 4, p. 993–999, 1969. Cit. on p. 58.

96 KOBAYASHI, S.; TOKUDA, Y.; MIZOGUCHI, T.; SHIBATA, N.; SATO, Y.; IKUHARA, Y.; YAMAMOTO, T. Quantitative analyses of oxidation states for cubic $SrMnO_3$ and orthorhombic $SrMnO_{2.5}$ with electron energy loss spectroscopy. **Journal of applied physics**, AIP Publishing, v. 108, n. 12, 2010. Cit. on p. 58.

97 KIKUCHI, K.; CHIBA, H.; KIKUCHI, M.; SYONO, Y. Syntheses and magnetic properties of $La_{1-x}Sr_xMnO_y$ ($0.5 \leq x \leq 1.0$) perovskite. **Journal of Solid State Chemistry**, Elsevier, v. 146, n. 1, p. 1–5, 1999. Cit. on p. 58.

98 CHMAISSEM, O.; DABROWSKI, B.; KOLESNIK, S.; MAIS, J.; BROWN, D.; KRUK, R.; PRIOR, P.; PYLES, B.; JORGENSEN, J. Relationship between structural parameters and the Néel temperature in $Sr_{1-x}Ca_xMnO_3$ ($0 < \sim x < \sim 1$) and $Sr_{1-y}Ba_yMnO_3$ ($y < \sim 0.2$). **Physical Review B**, APS, v. 64, n. 13, p. 134412, 2001. Cit. on p. 58.

99 KURTZ, R. L.; HENRICH, V. E. Surface electronic structure and chemisorption on corundum transition-metal oxides: α-Fe_2O_3. **Physical Review B**, APS, v. 36, n. 6, p. 3413, 1987. Cit. on p. 58.

100 HENDEWERK, M.; SALMERON, M.; SOMORJAI, G. Water adsorption on the (001) plane of Fe_2O_3: An XPS, UPS, Auger, and TPD study. **Surface Science**, Elsevier, v. 172, n. 3, p. 544–556, 1986. Cit. on p. 58.

101 ZHANG, P.; COHEN, R.; HAULE, K. Magnetic phase diagram of FeO at high pressure. In: IOP PUBLISHING, 1. JOURNAL of Physics: Conference Series. [S.l.: s.n.], 2017. v. 827, p. 012006. Cit. on p. 58.

102 WILLIS, B.; ROOKSBY, H. Change of structure of ferrous oxide at low temperature. **Acta Crystallographica**, International Union of Crystallography, v. 6, n. 11-12, p. 827–831, 1953. Cit. on p. 58.

103 YAHI, N.; AZZAZ, Y.; AMERI, M.; BENOUIS, M.; BENSAID, D.; ARBOUCHE, O.; YAMANI, M.; MOULAY, N. Anti-Ferromagnetic Structure and Magnetic Properties of FeO with GGA+ U+ SOC Study. **Physics of the Solid State**, Springer, v. 62, p. 472–479, 2020. Cit. on p. 58.

104 CAPONE, M.; RIDLEY, C. J.; FUNNELL, N. P.; GUTHRIE, M.; BULL, C. L. Subtle structural changes in $LaFeO_3$ at high pressure. **physica status solidi (b)**, Wiley Online Library, v. 258, n. 2, p. 2000413, 2021. Cit. on p. 59.

105 GELLER, S.; WOOD, E. Crystallographic studies of perovskite-like compounds. I. Rare earth orthoferrites and $YFeO_3$, $YCrO_3$, $YAlO_3$. **Acta Crystallographica**, International Union of Crystallography, v. 9, n. 7, p. 563–568, 1956. Cit. on p. 59.

106 MAREZIO, M.; DERNIER, P. The bond lengths in $LaFeO_3$. **Materials Research Bulletin**, Elsevier, v. 6, n. 1, p. 23–29, 1971. Cit. on p. 59.

107 IMADA, M.; FUJIMORI, A.; TOKURA, Y. Metal-insulator transitions. **Reviews of modern physics**, APS, v. 70, n. 4, p. 1039, 1998. Cit. on pp. 59, 60.

108 CHRISTIANSEN, E.; NORD, M.; HALLSTEINSEN, I.; VULLUM, P. E.; TYBELL, T.; HOLMESTAD, R. Structural investigation of epitaxial $LaFeO_3$ thin films on (111) oriented $SrTiO_3$ by transmission electron microscopy. In: IOP

PUBLISHING, 1. JOURNAL of Physics: Conference Series. [S.l.: s.n.], 2015. v. 644, p. 012002. Cit. on p. 59.

109 HEIFETS, E.; KOTOMIN, E. A.; BAGATURYANTS, A. A.; MAIER, J. Thermodynamic stability of non-stoichiometric $SrFeO_{3-\delta}$: a hybrid DFT study. **Physical Chemistry Chemical Physics**, Royal Society of Chemistry, v. 21, n. 7, p. 3918–3931, 2019. Cit. on p. 60.

110 LONG, Y.; KANEKO, Y.; ISHIWATA, S.; TAGUCHI, Y.; TOKURA, Y. Synthesis of cubic $SrCoO_3$ single crystal and its anisotropic magnetic and transport properties. **Journal of Physics: Condensed Matter**, IOP Publishing, v. 23, n. 24, p. 245601, 2011. Cit. on pp. 60, 62.

111 SILVA, S. P. da; SITA, L. E.; SANTOS, C. S. dos; SCARMINIO, J. Effects on the phases and crystalline structures of $LiCoO_2$ cathode under thermal treatments up to $400^\circ C$. **Journal of Alloys and Compounds**, Elsevier, v. 810, p. 151933, 2019. Cit. on p. 60.

112 WAN, J.; ZHU, J.; XIANG, Y.; ZHONG, G.; LIU, X.; LI, Y.; ZHANG, K. H.; HONG, C.; ZHENG, J.; WANG, K., et al. Revealing the correlation between structure evolution and electrochemical performance of high-voltage lithium cobalt oxide. **Journal of Energy Chemistry**, Elsevier, v. 54, p. 786–794, 2021. Cit. on p. 60.

113 PETITTO, S. C.; MARSH, E. M.; CARSON, G. A.; LANGELL, M. A. Cobalt oxide surface chemistry: The interaction of CoO (1 0 0), Co_3O_4 (1 1 0) and Co_3O_4 (1 1 1) with oxygen and water. **Journal of Molecular Catalysis A: Chemical**, Elsevier, v. 281, n. 1-2, p. 49–58, 2008. Cit. on p. 60.

114 ZHENG, H. Electronic structure of CoO. **Physica B: Condensed Matter**, Elsevier, v. 212, n. 2, p. 125–138, 1995. Cit. on p. 60.

115 JAUCH, W.; REEHUIS, M.; BLEIF, H.; KUBANEK, F.; PATTISON, P. Crystallographic symmetry and magnetic structure of CoO. **Physical Review B**, APS, v. 64, n. 5, p. 052102, 2001. Cit. on p. 60.

116 KRÜGER, E. Magnetic structure of CoO. **Symmetry**, MDPI, v. 13, n. 8, p. 1513, 2021. Cit. on p. 60.

117 LAUBACH, S.; LAUBACH, S.; SCHMIDT, P. C.; ENSLING, D.; SCHMID, S.; JAEGERMANN, W.; THISSEN, A.; NIKOLOWSKI, K.; EHRENBERG, H. Changes in the crystal and electronic structure of $LiCoO_2$ and $LiNiO_2$ upon Li intercalation and de-intercalation. **Physical Chemistry Chemical Physics**, Royal Society of Chemistry, v. 11, n. 17, p. 3278–3289, 2009. Cit. on p. 61.

118 RADWANSKI, R.; ROPKA, Z. Magnetic properties and the electronic structure of $LiCoO_2$. **arXiv preprint cond-mat/0610611**, 2006. Cit. on p. 61.

119 KAWASAKI, S.; TAKANO, M.; TAKEDA, Y. Ferromagnetic Properties of $SrFe_{1-x}Co_xO_3$ Synthesized under High Pressure. **Journal of Solid State Chemistry**, Elsevier, v. 121, n. 1, p. 174–180, 1996. Cit. on p. 62.

120 BEZDICKA, P.; WATTIAUX, A.; GRENIER, J.; POUCHARD, M.; HAGENMULLER, P. Preparation and characterization of fully stoichiometric $SrCoO_3$ by electrochemical oxidation. **Zeitschrift für anorganische und allgemeine Chemie**, Wiley Online Library, v. 619, n. 1, p. 7–12, 1993. Cit. on p. 62.

121 BALAMURUGAN, S.; YAMAURA, K.; KARKI, A.; YOUNG, D.; ARAI, M.; TAKAYAMA-MUROMACHI, E. Specific-heat evidence of strong electron correlations and thermoelectric properties of the ferromagnetic perovskite $SrCoO_{3-\delta}$. **Physical Review B**, APS, v. 74, n. 17, p. 172406, 2006. Cit. on p. 62.

122 HWANG, J.; KIM, D.; KANG, J.-S.; KOLESNIK, S.; CHMAISSEM, O.; MAIS, J.; DABROWSKI, B.; BAIK, J.; SHIN, H.; LEE, J., et al. Soft x-ray absorption spectroscopy study of Mo-rich $SrMn_{1-x}Mo_xO_3$ ($x \geq 0.5$). **Physical Review B**, APS, v. 83, n. 7, p. 073103, 2011. Cit. on p. 62.

123 HÉBERT, C.; WILLINGER, M.; SU, D. S.; PONGRATZ, P.; SCHATTSCHNEIDER, P.; SCHLÖGL, R. Oxygen K-edge in vanadium oxides: simulations and experiments. **The European Physical Journal B-Condensed Matter and Complex Systems**, Springer, v. 28, p. 407–414, 2002. Cit. on pp. 64, 65.

124 BRIK, M.; OGASAWARA, K.; IKENO, H.; TANAKA, I. Fully relativistic calculations of the $L_{2,3}$-edge XANES spectra for vanadium oxides. **The European Physical Journal B-Condensed Matter and Complex Systems**, Springer, v. 51, p. 345–355, 2006. Cit. on p. 64.

125 BYSTRÖM, A.; WILHELMI, K.-A.; BROTZEN, O. Vanadium pentoxide - a compound with five-coordinated vanadium atoms. **Acta Chem Scand**, v. 4, p. 1119–1130, 1950. Cit. on p. 64.

126 EYERT, V.; HÖCK, K.-H. Electronic structure of V_2O_5: role of octahedral deformations. **Physical Review B**, APS, v. 57, n. 20, p. 12727, 1998. Cit. on p. 65.

127 MITRA, C.; HU, Z.; RAYCHAUDHURI, P.; WIRTH, S.; CSISZAR, S.; HSIEH, H.; LIN, H.-J.; CHEN, C.; TJENG, L. Direct observation of electron doping in $La_{0.7}Ce_{0.3}MnO_3$ using x-ray absorption spectroscopy. **Physical Review B**, APS, v. 67, n. 9, p. 092404, 2003. Cit. on pp. 67, 68, 70.

128 VINOGRADOV, A. S.; PREOBRAJENSKI, A. B.; KRASNIKOV, S. A.; CHASSÉ, T.; SZARGAN, R.; KNOP-GERICKE, A.; SCHLÖGL, R.; BRESSLER, P. X-ray absorption evidence for the back-donation in iron cyanide complexes. **Surface Review and Letters**, World Scientific, v. 9, n. 01, p. 359–364, 2002. Cit. on pp. 67–70.

129 GILBERT, B.; FRAZER, B.; BELZ, A.; CONRAD, P.; NEALSON, K.; HASKEL, D.; LANG, J.; SRAJER, G.; DE STASIO, G. Multiple scattering calculations of bonding and X-ray absorption spectroscopy of manganese oxides. **The Journal of Physical Chemistry A**, ACS Publications, v. 107, n. 16, p. 2839–2847, 2003. Cit. on pp. 67, 91–93, 96.

130 KIM, D.; LEE, E.; KIM, H. W.; KOLESNIK, S.; DABROWSKI, B.; KANG, C.-J.; KIM, M.; MIN, B.; LEE, H.-K.; KIM, J.-Y., et al. Correlation between Mn and Ru valence states and magnetic phases in $SrMn_{1-x}Ru_xO_3$. **Physical Review B**, APS, v. 91, n. 7, p. 075113, 2015. Cit. on pp. 67, 90–93.

131 WU, Z.; GOTA, S.; JOLLET, F.; POLLAK, M.; GAUTIER-SOYER, M.; NATOLI, C. Characterization of iron oxides by x-ray absorption at the oxygen K edgeusing a full multiple-scattering approach. **Physical Review B**, APS, v. 55, n. 4, p. 2570, 1997. Cit. on pp. 67, 91, 93, 94.

132 SPALDIN, N. A. **Magnetic materials: fundamentals and applications**. [S.l.]: Cambridge university press, 2010. Cit. on p. 77.

133 KANG, J.-S.; HAN, S.; PARK, J.-G.; WI, S.; LEE, S.; KIM, G.; SONG, H.; SHIN, H.; JO, W.; MIN, B. Photoemission and x-ray absorption of the electronic structure of multiferroic RMnO$_3$ (R= Y, Er). **Physical Review B**, APS, v. 71, n. 9, p. 092405, 2005. Cit. on p. 90.

134 OLALDE-VELASCO, P.; JIMÉNEZ-MIER, J.; DENLINGER, J.; YANG, W.-L. Atomic multiplets at the L$_{2,3}$ edge of 3d transition metals and the ligand K edge in x-ray absorption spectroscopy of ionic systems. **Physical Review B**, APS, v. 87, n. 24, p. 245136, 2013. Cit. on p. 91.

135 VAN ELP, J.; TANAKA, A. Threshold electronic structure at the oxygen K edge of 3d-transition-metal oxides: A configuration interaction approach. **Physical Review B**, APS, v. 60, n. 8, p. 5331, 1999. Cit. on p. 91.

136 WEISSBLUTH, M. **Atoms and molecules**. [S.l.]: Elsevier, 2012. Cit. on pp. 124, 125.

137 JACKSON, J. D. **Classical electrodynamics**. [S.l.]: John Wiley & Sons, 2021. Cit. on p. 125.

138 WIGNER, E. P. On the Matrices Which Reduce the Kronecker Products of Representations of S. R. Groups. In: **The Collected Works of Eugene Paul Wigner: Part A: The Scientific Papers**. Ed. by Arthur S. Wightman. Berlin, Heidelberg: Springer Berlin Heidelberg, 1993. P. 608–654. ISBN 978-3-662-02781-3. DOI: `10.1007/978-3-662-02781-3_42`. Available from: https://doi.org/10.1007/978-3-662-02781-3_42. Cit. on p. 137.

139 CRUZAN, O. R. TRANSLATIONAL ADDITION THEOREMS FOR SPHERICAL VECTOR WAVE FUNCTIONS. **Quarterly of Applied Mathematics**, Brown University, v. 20, n. 1, p. 33–40, 1962. ISSN 0033569X, 15524485. Available from: http://www.jstor.org/stable/43636359. Visited on: 10 Mar. 2023. Cit. on p. 137.

140 COHEN-TANNOUDJI, C.; DIU, B.; LALOE, F. **Quantum Mechanics, Volume 1: Basic Concepts, Tools, and Applications**. [S.l.]: Wiley-Vch, 2020. v. 1. Cit. on p. 138.

141 CUBIC Harmonic. [S.l.: s.n.]. `https://en.wikipedia.org/wiki/Cubic_harmonic`. Visited on: 13 Mar. 2023. Cit. on p. 141.

142 RETEGAN, M. **Crispy: v0.7.4**. [S.l.: s.n.], 2019. DOI: `10.5281/zenodo.1008184`. Available from: https://doi.org/10.5281/zenodo.1008184. Cit. on p. 158.

Appendix

APPENDIX A

The Fermi's Golden Rule

One of the main tasks here is to determine how the Fermi's Golden Rule presented in Chapter 3 is obtained in that form. Here, some considerations will be made to be able to achieve the ends necessary to obtain the desired equation. It is assumed that the scattering is small and constant and that this approach limits only to the photoelectric effect. X-ray acts on charged particles such as electrons. As an X-ray wave passes by an electron, its electric field exerts forces in alternating directions, leading to oscillations in both strength and direction. Traditionally, in most descriptions of X-ray absorption, the electromagnetic wave is represented by the vector field $\vec{A}$. However, the transition from classical to quantum mechanics requires a fundamental change. We move from the classical vector potential $\vec{A}(r,\vec{t})$ to a quantum mechanical operator. To accomplish this transition, a powerful tool from quantum mechanics is employed: second quantization. In this context, a creation operator is denoted as $a^{\dagger}_{\vec{k}q}$, which generates a photon with a specific wave vector $\vec{k}$ and polarization q. Similarly, we have an annihilation operator, given as $a_{\vec{k}q}$. Both of these operators adhere to the commutation relation related to Bose particles:

$$a_{\vec{k}q}a^{\dagger}_{\vec{k}'q'} - a^{\dagger}_{\vec{k}'q'}a_{\vec{k}q} = \delta_{\vec{k}\vec{k}'}\delta_{qq'}. \tag{A.1}$$

The number operator of a photon with $\vec{k}$ and q is given by $n_{\vec{k}q} = a^{\dagger}_{\vec{k}q}a_{\vec{k}q}$. Employing these operators leads to the quantum-mechanical representation of the vector potential in the Schrödinger representation as follows:

$$\vec{A}(\vec{r}) = \sum_{\vec{k}q} A_0 \hat{e}_{\vec{k}q}\left(a_{\vec{k}q}e^{i\vec{k}\cdot\vec{r}} + a^{\dagger}_{\vec{k}q}e^{-i\vec{k}\cdot\vec{r}}\right), \tag{A.2}$$

where A_0 is defined as [32, 136]:

$$A_0 = \sqrt{\frac{2\pi\hbar c^2}{V_s \omega_{\vec{k}}}}, \tag{A.3}$$

with $\omega_{\vec{k}} = c|\vec{k}|$ and V_s representing the system volume in which the photon is normalized, $\hat{e}_{\vec{k}q}$ serves as a unit vector for polarization q. It is worth noting that, for brevity, it will not delve into the explicit treatment of polarization effects in the subsequent discussion. The Hamiltonian governing the interaction between X-rays and electrons can be approximated using perturbation theory. In particular, its first term can be expressed as [32]:

$$\hat{H}_1 = \frac{e}{mc} \sum_i \hat{p}_i \cdot \vec{A}(\vec{r}_i) + \frac{e}{2mc} \sum_i \sigma_i \cdot \vec{\nabla} \times \vec{A}(\vec{r}_i). \tag{A.4}$$

The first term within the interaction Hamiltonian, $\hat{H}_1$, describes the influence of the vector field $\vec{A}$ upon the momentum operator $\hat{p}$ of an electron, or in other words, it describes how the electric field $\vec{E}$ acts upon the electron's momenta, with both fields sharing a collinear relationship. The proportionality factor in this term encompasses the electron's charge e, its mass m, and the speed of light c. The second term in the Hamiltonian characterizes the magnetic field $\vec{B}$ (which is derived from $\vec{\nabla} \times \vec{A}$) acting on the electron's spin σ. When considering X-ray interaction with matter, a pivotal role is assigned to the Golden Rule. This fundamental principle states that the transition probability W between an initial state Φ_i and a final state Φ_f within a system, caused by the absorption of an incident photon with energy $\hbar\omega$, can be expressed as:

$$W_{fi} = \frac{2\pi}{\hbar} \sum_f \left| \langle \Phi_f | \hat{T}_1 | \Phi_i \rangle \right|^2 \delta \left(E_f - Ei - \hbar\omega \right). \tag{A.5}$$

The wave functions for the initial and final states are composed of two components: one for the electron and one for the photon. The photon part of the wave function takes care of the annihilation of a photon in the X-ray absorption process. However, for the sake of brevity, it will not be delved into this aspect in this text. The delta function ensures energy conservation, signifying that a transition occurs only if the energy of the final state matches the sum of the energy in the initial state and the energy of the incident photon. Additionally, the square of the matrix element provides the transition rate.

The transition operator $\hat{T}_1$ describes one-photon transmission such as X-ray absorption. In the first-order approximation, this operator is equivalent to the interaction Hamiltonian. Thus, by incorporating the vector field into $\hat{H}_1$ and disregarding the summation over i:

$$\hat{T}_1 = \sum_{\vec{k},q} \frac{e}{m} \sqrt{\frac{2\pi\hbar}{V_s \omega_{\vec{k}}}} \left[a_{\vec{k}q} \left(\hat{e}_{\vec{k}q} \cdot \hat{p} \right) e^{i\vec{k}\cdot\vec{r}} + \frac{\hbar}{2} a^{\dagger}_{\vec{k}q} \left(\hat{e}_{\vec{k}q} \cdot \sigma \times \hat{k} \right) e^{-i\vec{k}\cdot\vec{r}} \right]. \tag{A.6}$$

The terms within the brackets can be categorized into two components: the first term signifies the electromagnetic interaction (a non-relativistic effect), while the second term accounts for spin interaction (a relativistic effect). Given that the spin interaction has minimal relevance in core-level spectroscopy, it will be omitted from these considerations. Consequently, the transition operator $\hat{T}_1$ simplifies to:

$$\hat{T}_1 = \sum_{\vec{k},q} \frac{e}{m} \sqrt{\frac{2\pi\hbar}{V_s \omega_{\vec{k}}}} \left[a_{\vec{k}q} \left(\hat{e}_{\vec{k}q} \cdot \hat{p} \right) e^{i\vec{k}\cdot\vec{r}} \right] . \tag{A.7}$$

The above equation can be rewritten considering the Taylor expansion of the exponential, given by:

$$e^{i\vec{k}\cdot\vec{r}} = 1 + i\vec{k}\cdot\vec{r} + \cdots \ . \tag{A.8}$$

The expansion is truncated after the first two terms. This happens because starting from the third term onward, the contributions become exceedingly small. Consequently, it is possible to safely neglect terms beyond the second order, resulting in the simplified transition operator $\hat{T}_1$:

$$\hat{T}_1 = \sum_{\vec{k},q} a_{\vec{k}q} \frac{e}{m} \sqrt{\frac{2\pi\hbar}{V_s \omega_{\vec{k}}}} \left[\left(\hat{e}_{\vec{k}q} \cdot \hat{p} \right) + i \left(\hat{e}_{\vec{k}q} \cdot \hat{p} \right) \left(\vec{k}\cdot\vec{r} \right) \right] , \tag{A.9}$$

the first term within the brackets corresponds to the electric dipole (ED) approximation, while the second term represents the electric quadrupole (EQ) approximation. There are two key reasons for the decision to omit the consideration of the EQ approximation in this text. The first reason comes from the fact that it is possible to calculate the value of $\vec{k}\cdot\vec{r}$ using the edge energy in electron volts (eV) and the atomic number of the analyzed atom in the following way [32]:

$$\vec{k}\cdot\vec{r} \approx \frac{\sqrt{\hbar\omega_{edge}}}{80Z} . \tag{A.10}$$

As an illustrative example, let's consider the K edge ($1s$ core level) of Zinc with an atomic number of $Z = 30$ and an edge energy of $\hbar\omega_{edge} = 9659\ eV$. In this case, the value of $\vec{k}\cdot\vec{r}$ is approximately 0.04. This pattern holds true for other $3d\ TM$ as well. Given that the transition probability is proportional to the square of the matrix element, the EQ transition is smaller by approximately a factor of 10^{-3} compared to the ED transition. Additionally, we can draw on an argument from electrodynamics [136, 137]. When the exponential term of the form $e^{i\vec{k}\cdot\vec{r}}$ can be approximated as unity ($e^{i\vec{k}\cdot\vec{r}} \approx 1$), while neglecting the other terms from its expansion, it is important to recall that this exponential is present in the vector potential $\vec{A}$ equation. This approximation corresponds to a scenario where all terms in the multipole expansion of the field, except for the ED term, are effectively disregarded Combining these arguments, we arrive at the electric dipole approximation, and within this approximation, the transition operator $\hat{T}_1$ can be expressed as:

$$\hat{T}_1 = \sum_{\vec{k},q} a_{\vec{k}q} \frac{e}{m} \sqrt{\frac{2\pi\hbar}{V_s \omega_{\vec{k}}}} \left[\hat{e}_{\vec{k}q} \cdot \hat{p} \right] . \tag{A.11}$$

But how is it possible to get to a more conventional form of the transition operator? For this, let us again consider the interaction Hamiltonian $\hat{H}_1$:

$$\hat{H}_1 = \frac{e}{m}\sum_{\vec{k},q}\sqrt{\frac{2\pi\hbar}{V_s\omega_{\vec{k}}}}\left(\hat{p}\cdot\hat{e}_{\vec{k}q}\right)\left[a_{\vec{k}q}e^{i\vec{k}\cdot\vec{r}} + a^{\dagger}_{\vec{k}q}e^{-i\vec{k}\cdot\vec{r}}\right]. \tag{A.12}$$

Taking into account that the Coulomb gauge $\vec{\nabla}\cdot\vec{A} = 0$ is being used, so $\hat{H}_1$ becomes, by writing it in a form like $\hat{H}_1 = \hat{H}_1^{(-)} + \hat{H}_1^{(+)}$, where

$$\hat{H}_1^{(-)} = \frac{e}{m}\sum_{\vec{k},q}\sqrt{\frac{2\pi\hbar}{V_s\omega_{\vec{k}}}}\left(\hat{e}_{\vec{k}q}\cdot\hat{p}\right)a_{\vec{k}q}e^{i\vec{k}\cdot\vec{r}}, \tag{A.13}$$

and

$$\hat{H}_1^{(+)} = \frac{e}{m}\sum_{\vec{k},q}\sqrt{\frac{2\pi\hbar}{V_s\omega_{\vec{k}}}}\left(\hat{e}_{\vec{k}q}\cdot\hat{p}\right)a^{\dagger}_{\vec{k}q}e^{-i\vec{k}\cdot\vec{r}}. \tag{A.14}$$

From this point onward, only $\hat{H}_1^{(-)}$ will be considered since for $\hat{H}_1^{(+)}$ there is a similar line of thought. In the absence of any interaction, the wave function of the entire system can be represented as the product of an atomic wave function and a wave function describing the radiation field.

$$\psi_a\left|n_1, n_2, \cdots, n_i, \cdots\right\rangle \equiv \left|\psi_a; n_1, n_2, \cdots, n_i, \cdots\right\rangle. \tag{A.15}$$

Here, ψ_a represents an eigenfunction of the atomic Hamiltonian given by:

$$\hat{H}_{atom.} = \sum_i\left(\frac{\vec{p}_i^{\,2}}{2m}\right) + V. \tag{A.16}$$

The wave function $\left|n_1, n_2, \cdots, n_i, \cdots\right\rangle$, with $n_i = n_{\vec{k}i,qi}$, characterizes the radiation field in the occupation numbers (or Fock space) representation. Now, let us delve into the analysis of the matrix elements of $\hat{H}_1^{(-)}$:

$$\left\langle\psi_b; n'_1, n'_2, \cdots, n'_i, \cdots\right|\hat{H}_1^{(-)}\left|\psi_a; n_1, n_2, \cdots, n_i, \cdots\right\rangle.$$

Utilizing the orthogonality relation for the many-photon state:

$$\left\langle n'_1, n'_2, \cdots, n'_i, \cdots | n_1, n_2, \cdots, n_i, \cdots\right\rangle = \delta_{n'_1 n_1}\delta_{n'_2 n_2}\cdots\delta_{n'_i n_i}\cdots \tag{A.17}$$

and substituting indices $\vec{k}_i q_i$ with a simpler notation i for the operators (creation and annihilation), the action of these operators on many-photon states can be described as follows:

$$\begin{aligned}
a_i\left|n_1, n_2, \cdots, n_i, \cdots\right\rangle &= \sqrt{n_i}\left|n_1, n_2, \cdots, n_i - 1, \cdots\right\rangle, \\
a_i^{\dagger}\left|n_1, n_2, \cdots, n_i, \cdots\right\rangle &= \sqrt{n_i + 1}\left|n_1, n_2, \cdots, n_i + 1, \cdots\right\rangle, \\
a_i\left|n_1, n_2, \cdots, 0, \cdots\right\rangle &= 0.
\end{aligned} \tag{A.18}$$

For the matrix element of $\hat{H}^{(-)}1$ to be non-zero, at least one mode must satisfy $n_i' = n_i - 1$. For a single mode characterized by $\vec{k}q$, or equivalently, photons with momentum $\hbar\vec{k}$ and polarization q, the notation can be simplified to:

$$\left\langle b; n_{\vec{k}q} - 1 \right| \hat{H}_1^{(-)} \left| a; n_{\vec{k}q} \right\rangle = \frac{e}{m}\sqrt{\frac{2\pi\hbar}{V_s \omega_{\vec{k}}}} \left\langle b; n_{\vec{k}q} - 1 \right| \left(\hat{e}_{\vec{k}q} \cdot \hat{p}\right) a_{\vec{k}q} e^{i\vec{k}\cdot\vec{r}} \left| a; n_{\vec{k}q} \right\rangle ,$$

$$\left\langle b; n_{\vec{k}q} - 1 \right| \hat{H}_1^{(-)} \left| a; n_{\vec{k}q} \right\rangle = \frac{e}{m}\sqrt{\frac{2\pi\hbar n_{\vec{k}q}}{V_s \omega_{\vec{k}}}} \left\langle b \right| \left(\hat{e}_{\vec{k}q} \cdot \hat{p}\right) e^{i\vec{k}\cdot\vec{r}} \left| a \right\rangle , \tag{A.19}$$

where $|a\rangle \equiv |\psi_a\rangle$ and $|b\rangle \equiv |\psi_b\rangle$ represent the initial and final atomic states, respectively.

Let us examine the matrix element now. Again, using the same arguments to take care of the exponential as before. With this, rewriting the matrix element:

$$\left\langle b \right| \left(\hat{e}_{\vec{k}q} \cdot \hat{p}\right) e^{i\vec{k}\cdot\vec{r}} \left| a \right\rangle \underset{\mathrm{e}^{\mathrm{i}\vec{k}\cdot\vec{r}}\approx 1}{=} \left\langle b \right| \left(\hat{e}_{\vec{k}q} \cdot \hat{p}\right) \left| a \right\rangle = \hat{e}_{\vec{k}q} \cdot \left\langle b \right| \hat{p} \left| a \right\rangle . \tag{A.20}$$

For this, let's express the momentum operator in terms of the position operator $\hat{r}$ and the atomic Hamiltonian A.16 . Knowing that the commutator of $\hat{r}$ and $\hat{H}_{atom.}$ can be written as:

$$\left[\hat{r}, \hat{H}_{atom.}\right] = \frac{i\hbar}{m}\hat{p} \tag{A.21}$$

$$\hat{p} = \frac{m}{i\hbar}\left[\hat{r}, \hat{H}_{atom.}\right],$$

putting this into the matrix element:

$$\begin{aligned} \hat{e}_{\vec{k}q} \cdot \left\langle b \right| \hat{p} \left| a \right\rangle &= \frac{m}{i\hbar}\hat{e}_{\vec{k}q} \cdot \left\langle b \right| \left[\hat{r}, \hat{H}_{atom.}\right] \left| a \right\rangle \\ &= \frac{m}{i\hbar}\hat{e}_{\vec{k}q} \cdot \left\langle b \right| \hat{r}\hat{H}_{atom.} - \hat{H}_{atom.}\hat{r} \left| a \right\rangle \\ &= \frac{-im}{\hbar}\hat{e}_{\vec{k}q} \cdot \left\langle b \right| \left(E_a - E_b\right) \hat{r} \left| a \right\rangle . \end{aligned}$$

This leads to:

$$\hat{e}_{\vec{k}q} \cdot \left\langle b \right| \hat{p} \left| a \right\rangle = \frac{im}{\hbar}\left(E_b - E_a\right) \hat{e}_{\vec{k}q} \cdot \left\langle b \right| \hat{r} \left| a \right\rangle . \tag{A.22}$$

Here, E_a and E_b represent the eigenvalues of $\hat{H}_{atom.}$ corresponding to the eigenstates $|a\rangle$ and $|b\rangle$. These eigenvalues, by virtue of energy conservation as discussed earlier, <u>must</u> satisfy the relation:

$$E_b - E_a = \hbar\omega_{ba} = \hbar\omega_{\vec{k}}.$$

Therefore, within the ED approximation, the matrix element simplifies to:

$$\frac{im\hbar\omega_{\vec{k}}}{\hbar}\hat{e}_{\vec{k}q} \cdot \left\langle b \right| \hat{r} \left| a \right\rangle , \tag{A.23}$$

and returning to the matrix element for $\hat{H}_1^{(-)}$:

$$\left\langle b; n_{\vec{k}q} - 1 \right| \hat{H}_1^{(-)} \left| a; n_{\vec{k}q} \right\rangle = \left\langle b \right| ie\sqrt{\frac{2\pi\hbar\omega_{\vec{k}} n_{\vec{k}q}}{V_s}} \left(\hat{e}_{\vec{k}q} \cdot \hat{r}\right) \left| a \right\rangle . \tag{A.24}$$

Since, in first order, the transition operator for X-ray absorption can be said to be equal to the interaction Hamiltonian, it is obtained the following:

$$\hat{T}_1 = ie\sqrt{\frac{2\pi\hbar\omega_{\vec{k}}n_{\vec{k}q}}{V_s}}\left(\hat{e}_{\vec{k}q}\cdot\hat{r}\right). \tag{A.25}$$

Returning to the Fermi's Golden Rule, one obtain (omitting the summation over k):

$$W_{fi} = \frac{4\pi^2e^2\omega n_q}{V_s}\sum_f \left|\langle\Phi_f|\left(\hat{e}_q\cdot\hat{r}\right)|\Phi_i\rangle\right|^2\delta\left(E_f - E_i - \hbar\omega\right). \tag{A.26}$$

Or, more succinctly:

$$W_{fi}\ \alpha\ \sum_f \left|\langle\Phi_f|\left(\hat{e}_q\cdot\hat{r}\right)|\Phi_i\rangle\right|^2\delta\left(E_f - E_i - \hbar\omega\right). \tag{A.27}$$

APPENDIX B

Atomic Multiplet Theory

B.1 The Atomic Hamiltonian

The atomic multiplet theory is the description of the atomic structure with quantum mechanics. The starting point for this theory is to solve the Schrodinger equation already known for a long time. It is usual to work with an N-electron atom, where the Schrodinger equation becomes:

$$\hat{H}_N \left|\psi\right\rangle = E_N \left|\psi\right\rangle, \tag{B.1}$$

where the Hamiltonian $\hat{H}_N$ is given by:

$$\hat{H}_N = \sum_N \frac{\hat{P}_i^2}{2m} - \sum_N \frac{Ze^2}{|\hat{r}_i|} + \sum_{pairs} \frac{e^2}{\hat{r}_{ij}} + \sum_N \xi\left(\hat{r}_i\right) \hat{L}_i \cdot \hat{S}_i. \tag{B.2}$$

Here we have a new term different from the one-electron case, that referring to the electron-electron repulsion. In addition, the first two terms are the same for all electrons in a given electronic configuration, which contributes to the result as an average energy, or $\hat{H}_{av}$. Then, the e-e interaction and spin-orbit terms define the relative energy of the different terms within the subjected configuration. In this way, we can write both interactions as follows:

$$H_{ee} = \textstyle\sum_{pairs} \frac{e^2}{\hat{r}_{ij}} \quad , \quad H_{LS} = \sum_N \xi\left(\hat{r}_i\right) \hat{L}_i \cdot \hat{S}_i. \tag{B.3}$$

Since we are dealing with multi-electron configurations that can be expressed with the quantum numbers L, S, and J, in general we can represent these configurations with a term symbol written as

$$^{2S+1}L_J$$

where L is the total orbital angular momentum, J is the total angular momentum and $2S{+}1$ is the spin degeneracy (singlet, triplet, etc.). Usually we use this definition when the spin-orbit coupling is considerable. Now, considering the interaction Hamiltonian, a usual approach to solve it is to distinguish two situations, LS-coupling and jj-coupling. When treating valence electrons, especially in light elements, it is possible to neglect the spin-orbit coupling and use pure LS-coupling. Also, considering electrostatic interactions, they are diagonal in L and S, thus, also in J. But the spin-orbit coupling is only diagonal with J, which implies that if the spin-orbit is considerably important, the overall Hamiltonian is only diagonal in J.

Resuming all the above, the result of spin-orbit coupling is that a term for the free ion is split into states of different energies. For example, a ^3P state of a carbon atom with a p^2 electron configuration would be split into three different energy states (according to the three possible J values 0, 1, and 2): $^3P_0$, $^3P_1$, $^3P_2$. Finally, the relative energies of the states can be predicted from Hund's Rules.

- Hund's Rules:
  - 1. Term symbol with maximum S.
  - 2. Term symbol with maximum L.
  - 3. Term symbol with maximum J (if the shell is more than half-full).
    - For subshells that are less than half-filled, the lowest energy state has the lowest J value.
    - For subshells that are exactly half-filled, there is only one J value, thus it is the lowest energy.
    - For subshells that are more than half-filled, the lowest energy state has the largest J value.

Now, the next step to take is to calculate the matrix elements of these states with the Hamiltonian B.2. Looking more carefully at the e-e repulsion term, we have the following:

$$\langle H_{ee}\rangle = \left\langle {}^{2S+1}L_J \right| \sum_{pairs} \frac{e^2}{\hat{r}_{ij}} \left| {}^{2S'+1}L'_{J'} \right\rangle . \tag{B.4}$$

This represents the relative energy of the different terms. To evaluate this, we can make use of basics of quantum mechanics to write the states that are going to be used here, beginning with the one-electron state, without the spin-orbit interaction for a more simple approach, so we have:

$$|\psi\rangle = |n, l, m_l, m_s\rangle = |R_{n,l}\rangle \, |Y_l^{m_l}\rangle \, |\chi_{ms}\rangle \, , \tag{B.5}$$

where R is related to the radial part, Y to the angular one and χ to the spin. But, since we are dealing with the interaction between two different electrons, we can make use of the two-electron state, which is written as

$$|\psi_i;\psi_j\rangle = \hat{A}\,|n_i,l_i,m_{li},m_{si};n_j,l_j,m_{lj},m_{sj}\rangle\,, \tag{B.6}$$

where i refers to the state ψ_i of the electron 1 and j to the state ψ_j of the electron 2. Also, $\hat{A}$ is the antisymmetric of the antisymmetrizer operator that makes sure that the wave functions of the system obey the Pauli exclusion principle by making the wave function of N identical fermions antisymmetric under the exchange of the coordinates of any pair of fermions. Now returning to the matrix element, if we take a closer look at the function, we can see that it is possible to expand it in terms of Legendre polynomials, like

$$\begin{aligned}\tfrac{e^2}{r_{12}} &= \tfrac{e^2}{\sqrt{r_1^2+r_2^2-2r_1r_2\cos\Omega}} \quad (r_1,r_2\rightarrow r_<,r_>)\\ &= \tfrac{e^2}{r_>}\tfrac{1}{\sqrt{1+\left(\frac{r_<}{r_>}\right)^2-2\frac{r_<}{r_>}\cos\Omega}}\\ &= \tfrac{e^2}{r_>}\textstyle\sum_{k=0}^{\infty}\left(\frac{r_<}{r_>}\right)^k P_k\left(\cos\Omega\right),\end{aligned} \tag{B.7}$$

then

$$\frac{e^2}{r_{12}} = \sum_{k=0}^{\infty}\frac{e^2 r_<^k}{r_>^{k+1}}P_k\left(\cos\Omega\right). \tag{B.8}$$

Now, we can actually write the e-e repulsion matrix elements as

$$\langle\psi_i;\psi_j|\,\frac{e^2}{r_{ij}}\,|\psi_p;\psi_q\rangle = \langle\psi_i;\psi_j|\sum_{k=0}^{\infty}\frac{e^2 r_<^k}{r_>^{k+1}}P_k\left(\cos\Omega\right)|\psi_p;\psi_q\rangle\,. \tag{B.9}$$

Now, using the equation for one-electron state, that makes possible to separate the radial from angular parts of each ψ state, and remembering that we have an antisymmetrizer operator for the two-electron states, we will have the following equation describing the e-e repulsion:

$$\begin{aligned}\langle\psi_i;\psi_j|\,\frac{e^2}{r_{ij}}\,|\psi_p;\psi_q\rangle = \sum_{k=0}^{\infty}\Bigg[&\underbrace{\left\langle R_{ni}^{li};R_{nj}^{lj}\right|\frac{e^2 r_<^k}{r>^{k+1}}\left|R_{np}^{lp};R_{nq}^{lq}\right\rangle}_{F^k}\underbrace{\left\langle Y_{li}^{mli};Y_{lj}^{mlj}\right|P_k\left(\cos\Omega\right)\left|Y_{lp}^{mlp};Y_{lq}^{mlq}\right\rangle\delta_{msi}^{msp}\delta_{msj}^{msq}}_{f_k} -\\ &-\underbrace{\left\langle R_{ni}^{li};R_{nj}^{lj}\right|\frac{e^2 r_<^k}{r>^{k+1}}\left|R_{nq}^{lq};R_{np}^{lp}\right\rangle}_{G^k}\underbrace{\left\langle Y_{li}^{mli};Y_{lj}^{mlj}\right|P_k\left(\cos\Omega\right)\left|Y_{lq}^{mlq};Y_{lp}^{mlp}\right\rangle\delta_{msi}^{msq}\delta_{msj}^{msp}}_{g_k}\Bigg].\end{aligned} \tag{B.10}$$

Following this, if we see the under text in the above equation, we can separate the angular from radial integrals, using the coefficients g_k and f_k and the Parameters F^k and G^k, the latter ones are known as the Slater-Condon Integrals or Slater-Condon parameters [43]. Also, because g_k and f_k are related to the angular integrals of the spherical harmonics, they can be expressed in terms of the Wigner's $3j$ and $6j$ symbols (due to orthonormality conditions and properties of the Wigner's symbols) [43]. The coefficients are, then,

$$f_k = (2l_1+1)(2l_2+1)(-1)^L \begin{pmatrix} l_1 & k & l_1 \\ 0 & 0 & 0 \end{pmatrix} \begin{pmatrix} l_2 & k & l_2 \\ 0 & 0 & 0 \end{pmatrix} \begin{Bmatrix} l_1 & l_2 & L \\ l_2 & l_1 & k \end{Bmatrix}. \tag{B.11}$$

And,

$$g_k = (2l_1+1)(2l_2+1)(-1)^S \begin{pmatrix} l_1 & k & l_2 \\ 0 & 0 & 0 \end{pmatrix} \begin{pmatrix} l_1 & k & l_2 \\ 0 & 0 & 0 \end{pmatrix} \begin{Bmatrix} l_1 & l_2 & L \\ l_1 & l_2 & k \end{Bmatrix}. \tag{B.12}$$

Also there is a reminder to this, if we are treating about equivalent electrons (same nl) the g_k term vanishes due to the selection rules of the Wigner's symbols! Finally, the matrix elements for the electron-electron repulsion are given by:

$$\langle \psi_i; \psi_j | \frac{e^2}{r_{ij}} | \psi_p; \psi_q \rangle = \sum_{k=0}^{\infty} \left[\overbrace{f_k F^K}^{Direct} + \overbrace{g_k G^k}^{Exchange} \right]. \tag{B.13}$$

Now something that will be established in here, since transition metals have, in their majority, the valence state of d^n ($l=2$) for their ground state configuration, the following calculations will proceed considering this specific configuration. For this case, the g term will vanish, and, by the selection rules for the Wigner's symbols, only the terms with $k=0,2,4$ are non-zero. If we considered transitions of $2p-3d$ character, for example, we would have the $k=0,2,4$ for the f terms and $k=1,3$ for the g terms.
Now, it is usual to express the matrix elements for the e-e repulsion in terms of the normalized S-C parameters, or even in terms of Racah parameters [32], which are a simplified version of the S-C parameters, since they are defined as linear combinations of the normalized S-C parameters. The transformation relations can be seen below.

$Slater-Condon$	$Normalized\ S-C$	$Racah$
F^0	$F_0 = F^0$	$A = F_0 - 49F_4$
F^2	$F_2 = \frac{F^2}{49}$	$B = F_2 - 5F_4$
F^4	$F_4 = \frac{F^4}{441}$	$C = 35F_4$

All terms present F_0, F^0 or A in their energies, because of that, they can be interpreted as a spherical term (a constant) in the e-e interaction and can be added to the $\langle H_{av} \rangle$.

Until now, we expressed all the e-e interaction within the spherical basis, because of the expansions made using spherical harmonics and the way we wrote the wave functions, using the atomic terms $\left|^{2S+1}L_J\right\rangle$. But it is more useful to write our basis using chemical orbitals, and for that we use cubic harmonics. To perform this is quite simple;

it only takes a basis transformation. For the sake of continuity, we will continue to use $d(l=2)$ states. Considering this, we have the following transformation relations:

$$\begin{aligned} |z^2\rangle &= |Y_2^0\rangle\,, \\ |zx\rangle &= \tfrac{1}{\sqrt{2}}(|Y_2^1\rangle - |Y_2^{-1}\rangle), \\ |yz\rangle &= \tfrac{i}{\sqrt{2}}(|Y_2^{-1}\rangle + |Y_2^1\rangle), \\ |xy\rangle &= \tfrac{i}{\sqrt{2}}(|Y_2^{-2}\rangle - |Y_2^2\rangle), \\ |x^2-y^2\rangle &= \tfrac{1}{\sqrt{2}}(|Y_2^{-2}\rangle + |Y_2^2\rangle). \end{aligned} \tag{B.14}$$

Now, since we are dealing with a new basis, it is convenient to use a new set of parameters that can express properly this basis, so, we will use the Kanamori Parameters. Such parameters can be written as a linear combination both of Racah or normalized Slater-Condon parameters, as given below

$$\begin{aligned} u &= A + 4B + 3C, \\ u' &= A - B + C, \\ j &= \tfrac{5}{2}B + C. \end{aligned} \tag{B.15}$$

$$\begin{aligned} u &= F_0 + 4F_2 + 36F_4, \\ u' &= F_0 - F_2 - 9F_4, \\ j &= \tfrac{5}{2}F_2 + \tfrac{45}{2}F_4. \end{aligned} \tag{B.16}$$

These parameters are very useful because they describe multiplet effects to the e-e interaction as being [62]:

- u (Intra Orbital Repulsion) -
  add for each pair in the same orbital;
- u' (Inter Orbital Repulsion) -
  add for each pair in a different orbital;
- j (Intra Atomic Exchange) -
  subtract for each pair with the same spin component.

Finally, with this, we can extract one last parameter, which is very useful to explain the e-e repulsion and the atomic multiplet Hamiltonian. The average e-e repulsion energy U. To do this, we need to acknowledge that a filled subshell, in the case of this discussion, a d^{10} state must not present any multiplet effect. So to describe this we use the Kanamori Parameters explained before. The parameters can be submitted in the following way: there are 5 intraband pairs in the d band, 40 interband possible pairs and 20 pairs with same spin components, this results in 45 pairs with an average repulsion energy. We can write the previous statement as the following equation:

$$E(d^{10}) = 5u + 40u' - 20j = 45U_{dd}. \tag{B.17}$$

Since the Kanamori Parameters can be given in terms of the Racah or normalized S-C, the average e-e repulsion energy can be written as:

$$U = A - \frac{14}{9}B + \frac{7}{9}C, \tag{B.18}$$

or

$$U = F_0 - \frac{14}{9}F_2 - 14F_4. \tag{B.19}$$

APPENDIX C

Crystal Field Theory in Different Symmetries

C.1 Octahedral (O_h) symmetry

Since the objective here is to demonstrate how the crystal field affects the calculations for the compounds used, let us start by solving the general crystal field potential, where it is used as a first approximation, the octahedral symmetry. In this case, it is considered a TM surrounded by a ligand octahedron, as shown in Figure 68.

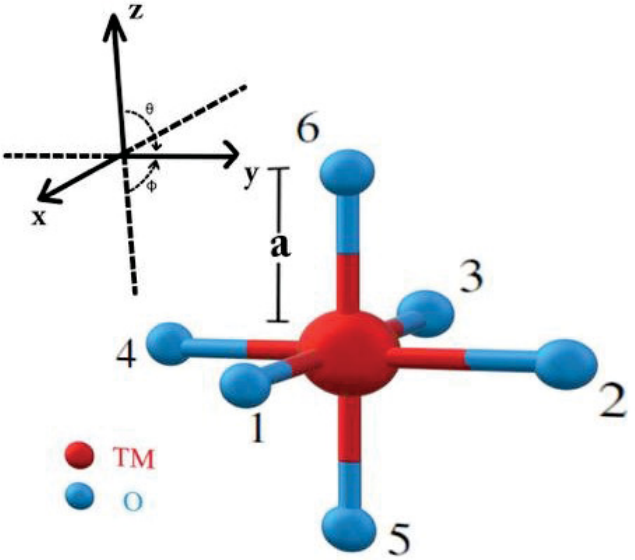

Figure 68 – Scheme showing the metal ion surrounded by its oxygen ligands in O_h symmetry.

In this scheme, the TM is in position $(0,0,0)$, while the ligands are in the positions ($\pm a$, 0, 0), (0,$\pm a$, 0), (0, 0, $\pm a$), where a is the lattice parameter or the distance from the central TM. Also, the ligands will be treated as point charges, so a static environment approximation is used [62]. Proceeding to the calculation part, it is possible to define the potential of one electron that is interacting with the ligands as:

$$V_{CF}(\vec{r}) = \sum_{i=1}^{6} \frac{Ze^2}{|\vec{R}_i - \vec{r}|}, \tag{C.1}$$

where $\vec{r}$ and $\vec{R}_i$ are the position vectors of the electron and the ligand ions, respectively. The expression given by C.1 can be considered as a small perturbation, because it is too small compared to other interactions such as electron-core and electron-electron interactions on the TM. One way to solve for this potential is to expand the above equation in terms of Legendre polynomials, then it becomes

$$V_{CF}(\vec{r}) = Ze^2 \sum_{i=1}^{6} \sum_{l=0}^{\infty} \frac{r_<^l}{r_>^{l+1}} P_l \cos\omega_i, \tag{C.2}$$

where $r_<$ and $r_>$ are the lesser and greater value between a and r, respectively, and ω_i corresponds to the angle between $\vec{r}$ and $\vec{R}_i$. Now, given the odd properties of the d orbitals, it is possible to consider here the values $r_< = r$ and $r_> = a$, so,

$$V_{CF}(\vec{r}) = Ze^2 \sum_{i=1}^{6} \sum_{l=0}^{\infty} \frac{r^l}{a^{l+1}} P_l \cos\omega_i. \tag{C.3}$$

Now, we can make use of the addition theorem for spherical harmonics, where

$$P_l \cos\omega_i = \frac{4\pi}{2l+1} \sum_{m=-l}^{l} Y_{l,m}^*(\theta_i^{'}, \phi_i^{'}) Y_{lm}(\theta, \phi). \tag{C.4}$$

where $(\theta_i^{'}, \phi_i^{'})$ and (θ, ϕ) are the coordinates of $\vec{R}_i$ and $\vec{r}$. Finally, the equation for the potential is

$$V_{CF}(\vec{r}) = Ze^2 4\pi \sum_{i=1}^{6} \sum_{l=0}^{\infty} \sum_{m=-l}^{l} \frac{r^l}{(2l+1)a^{l+1}} Y_{lm}^*(\theta_i^{'}, \phi_i^{'}) Y_{lm}(\theta, \phi). \tag{C.5}$$

Since we only deal with cubic symmetries, it is possible to rewrite the equation above in the way that it is possible to separate the part of it that only has the symmetry dependence. This dependence lies on the lattice distance a, and the angular positions of the ligand ions $(\theta_i^{'}, \phi_i^{'})$, with this, we can write the following expression.

$$q_{lm} = \frac{Ze^2 4\pi}{(2l+1)a^{l+1}} \sum_{i=1}^{6} Y_{lm}^*(\theta_i^{'}, \phi_i^{'}). \tag{C.6}$$

Finally, we have the general equation for the crystal field potential.

$$V_{CF}(\vec{r}) = \sum_{l=0}^{\infty} \sum_{m=-l}^{l} r^l q_{lm} Y_{lm}(\theta, \phi). \tag{C.7}$$

Now, the last part of the general method that can be applied to the cubic symmetries is the process of obtaining the potential matrix elements. With them, it is possible to obtain the potential's eigenvalues and eigenvectors that can be used to make a more complete analysis of this type of interaction. To obtain these matrix elements, it is necessary to consider the general solution for the crystal field problem, given by

$$\Psi_{nlm}(\vec{r}) = R_{nl}(r) Y_{lm}(\theta, \phi). \tag{C.8}$$

Using basic concepts of quantum mechanics, one can obtain the matrix elements through the following equation

$$\langle \Psi_{n'l'm'} | \, V_{CF}(\vec{r}) \, | \Psi_{n''l''m''} \rangle = \int \Psi^*_{n'l'm'}(\vec{r}) V_{CF}(\vec{r}) \Psi_{n''l''m''}(\vec{r}) d\vec{r}. \tag{C.9}$$

After substituting C.7 and C.6 into C.9, we will have a radial and an angular integrals to solve, but the radial contribution will remain unsolved and will be denoted as $\langle r^l \rangle$. Also, since the radial part will be left aside, the quantum number n will be left like this because it will not affect further calculations. As for the angular portion, we will have an integral of the type:

$$\int\int d\theta d\phi \sin\theta Y^*_{l'm'}(\theta, \phi) Y_{lm}(\theta, \phi) Y_{l''m''}(\theta, \phi) = C_{l'm'lml''m''}. \tag{C.10}$$

But it is possible to relate an integral like the one above with what is called Wigner $3-j$ symbols [138, 139], which can be related to spherical harmonics through the following equation

$$\begin{gathered} \int\int d\theta d\phi \sin\theta Y_{l_1 m_1}(\theta, \phi) Y_{l_2 m_2}(\theta, \phi) Y_{l_3 m_3}(\theta, \phi) = \\ = \sqrt{\tfrac{(2l_1+1)(2l_2+1)(2l_3+1)}{4\pi}} \begin{pmatrix} l_1 & l_2 & l_3 \\ 0 & 0 & 0 \end{pmatrix} \begin{pmatrix} l_1 & l_2 & l_3 \\ m_1 & m_2 & m_3 \end{pmatrix} \quad . \end{gathered} \tag{C.11}$$

So, using the property for the complex conjugate spherical harmonics and applying C.10 to C.11, we have the following result

$$C_{l'm'lml''m''} = (-1)^{m'} \sqrt{\frac{(2l'+1)(2l+1)(2l''+1)}{4\pi}} \begin{pmatrix} l' & l & l'' \\ 0 & 0 & 0 \end{pmatrix} \begin{pmatrix} l' & l & l'' \\ -m' & m & m'' \end{pmatrix}. \tag{C.12}$$

Now, before writing the matrix elements, let us impose some things that are necessary for this work. Since it is dealt with transition metals and, more specifically, TM of the $3d$ series, we see that the quantum numbers l' and l'' are equal to 2 and n in a general form is 3. This restricts the value of l in the range between 0 and 4. Now, we can pay more attention to Wigner's $3-j$ symbols, which have some selection rules, like $l^{'}+l+l^{''}=even$. Since $l^{'}=l^{''}=2$, for the rule to be satisfied, l must be 0, 2 or 4. With the previous arguments given, we can write the general formula for the crystal field potential matrix elements, when $3d$ orbitals are considered.

$$\left\langle 2\,m^{'}\middle| V_{CF}(\vec{r})\middle|2\,m^{''}\right\rangle = (-1)^{m^{'}} q_{lm}\left\langle r^{l}\right\rangle \frac{5}{2}\sqrt{\frac{(2l+1)}{\pi}}\begin{pmatrix} 2 & l & 2\\ 0 & 0 & 0\end{pmatrix}\begin{pmatrix} 2 & l & 2\\ -m^{'} & m & m^{''}\end{pmatrix}, \tag{C.13}$$

finally, using a known selection rule for orbital angular momentum in quantum mechanics [140], we find that the allowed values for quantum numbers $m^{'}$, $m^{''}$ and m are $(0,\pm 2)$ and $(0, \pm 2,\pm 4)$. Now that all the general method is exposed, let's look again at Figure 68, considering that we are dealing with a regular octahedron, the ligand angles ($\theta_i^{'},\phi_i^{'}$) are denoted by

$$\left(\theta_i^{'},\phi_i^{'}\right)=\left(\tfrac{\pi}{2},0\right),\left(\tfrac{\pi}{2},\tfrac{\pi}{2}\right),\left(\tfrac{\pi}{2},\pi\right),\left(\tfrac{\pi}{2},\tfrac{3\pi}{2}\right),(0,0),(\pi,0)\;;\;i=\{1,\cdots,6\}. \tag{C.14}$$

Taking into account the selection rules above and the ligand angles given, it is possible to obtain the values for the solution part that depends only on the symmetry given by equation C.6. In the end, due to the angles considered for the octahedral symmetry, not all possible values o l and m will be different from zero, only the following remained

$$\begin{aligned} q_{00} &= 6\sqrt{4\pi}\frac{Ze^2}{a},\\ q_{40} &= \frac{7}{3}\sqrt{\pi}\frac{Ze^2}{a^5},\\ q_{4\pm4} &= \frac{\sqrt{70\pi}}{6}\frac{Ze^2}{a^5}. \end{aligned} \tag{C.15}$$

At last, for the matrix elements, before substituting C.15 into C.13, it is necessary to take into account some other selection rules for the $3-j$ symbols, which are:

$$\begin{aligned} m^{i} &\in \{-l^{i},-l^{i+1},-l^{i+2},\cdots,l^{i}\}, i=\{\,{}^{\prime},{}^{\prime\prime}\,\},\\ m &= m^{'}-m^{''}, \end{aligned} \tag{C.16}$$

here, we have only the values 0 and 4 for l and 0 and ± 4 for m. Using the results of C.15 and considering C.16, we can evaluate the matrix elements. Also, since the term q_{00} is considered as a constant and will be present in all diagonal elements, it will be omitted because it will not be a real contribution to the potential. Thus, the non-zero matrix elements are

$$\begin{aligned} \langle 2\pm 2|\,V_{CF}(\vec{r})\,|2\pm 2\rangle &= \frac{1}{6}\frac{Ze^2}{a^5}\left\langle r^4\right\rangle,\\ \langle 2\pm 1|\,V_{CF}(\vec{r})\,|2\pm 1\rangle &= -\frac{2}{3}\frac{Ze^2}{a^5}\left\langle r^4\right\rangle,\\ \langle 2\,0|\,V_{CF}(\vec{r})\,|2\,0\rangle &= \frac{Ze^2}{a^5}\left\langle r^4\right\rangle,\\ \langle 2\pm 2|\,V_{CF}(\vec{r})\,|2\mp 2\rangle &= \frac{5}{6}\frac{Ze^2}{a^5}\left\langle r^4\right\rangle. \end{aligned} \tag{C.17}$$

However, since we are dealing with octahedral symmetry and the crystal field parameter for this symmetry is usually given by "$10Dq$", it is possible to write the matrix elements in terms of Dq, where D refers to the ligand ions and q to the TM electrons. Their values are known and are given below

$$D = \tfrac{35}{4}\tfrac{Ze^2}{a^5} \quad ; \quad q = \tfrac{2}{105}\left\langle r^4\right\rangle . \tag{C.18}$$

Therefore, the crystal field potential matrix in octahedral symmetry for a TM is given as

$$\begin{pmatrix} Dq & 0 & 0 & 0 & 5Dq \\ 0 & -4Dq & 0 & 0 & 0 \\ 0 & 0 & 6Dq & 0 & 0 \\ 0 & 0 & 0 & -4Dq & 0 \\ 5Dq & 0 & 0 & 0 & Dq \end{pmatrix} \tag{C.19}$$

Finally, it is possible to derive the crystal field unfolding of the d levels for a transition metal ion situated in an octahedral field, a concept briefly introduced in Chapter 3. This is accomplished by diagonalizing the matrix mentioned earlier. When this is done, two degenerate eigenvectors with an energy of $+6Dq$ emerge:

$$\begin{aligned} \left|\psi_{20}\right\rangle &= \left|d_{z^2}\right\rangle , \\ \frac{1}{\sqrt{2}}\left(\left|\psi_{2+2}\right\rangle + \left|\psi_{2-2}\right\rangle\right) &= \left|d_{x^2-y^2}\right\rangle . \end{aligned} \tag{C.20}$$

Additionally, three degenerate eigenvectors with energy $-4Dq$ appear:

$$\begin{aligned} \frac{i}{\sqrt{2}}\left(\left|\psi_{22}\right\rangle - \left|\psi_{2-2}\right\rangle\right) &= \left|d_{xy}\right\rangle , \\ \frac{i}{\sqrt{2}}\left(\left|\psi_{2+1}\right\rangle + \left|\psi_{2-1}\right\rangle\right) &= \left|d_{yz}\right\rangle , \\ \frac{1}{\sqrt{2}}\left(\left|\psi_{2+1}\right\rangle - \left|\psi_{2-1}\right\rangle\right) &= \left|d_{xz}\right\rangle . \end{aligned} \tag{C.21}$$

It should be noted that these eigenvectors are presented here in both the l, m basis, but also in cubic basis. The basis transformation will be explored more in the following section. For now, it is important to recognize that these eigenvectors correspond to the doubly degenerate and triply degenerate e_g and t_{2g} orbitals, which, as previously discussed, are separated in energy by a factor of $10Dq$.

C.2 Tetragonal (D_{4h}) symmetry

Here, almost everything that was explained in the O_h subsection will be used until equation C.13, but there is one small change that is needed. Previously it was considered a regular octahedron for calculations development. But it is not always like that. Usually in cubic symmetries, there can be a distortion in the apical oxygens, bringing the consequence that equation C.6 cannot be used since not all ligands are at a distance a from the central TM, as it is showcased in Figure 69. Because of that, it is necessary to take into account this new parameter in our calculations.

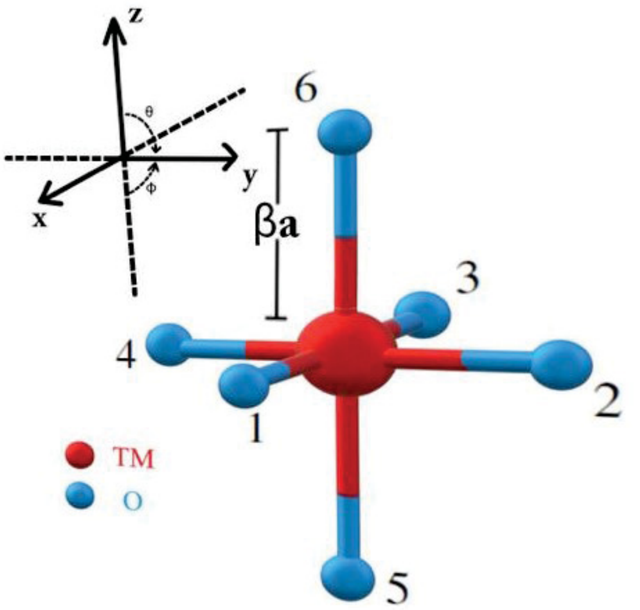

Figure 69 – Scheme showing the metal ion surrounded by its oxygen ligands in D_{4h} symmetry.

Since we are dealing only with the distortion on the apical ligands, we can adapt the symmetry part equation and include this new adjustable quantity. Taking into account Figure 69 and the previous argument, the q_{lm} equation can be written in the form

$$q_{lm} = \frac{Ze^2 4\pi}{(2l+1)} \left[\sum_{i=1}^{6} \frac{Y_{lm}^*(\theta_i', \phi_i')}{a^{l+1}} + \sum_{j=1}^{2} \frac{Y_{lm}^*(\theta_j', \phi_j')}{(\beta a)^{l+1}} \right], \tag{C.22}$$

where the j index refers to the apical ligands that are distorted by a distance of βa, where beta can represent a contraction ($0 < \beta < 1$) or an expansion ($\beta > 1$). There are two special cases of values that β can assume, those are when $\beta \to \infty$ and $\beta = 1$. The first one represents the special case of the square planar symmetry, and the latter is when the compound takes the regular octahedral symmetry and all the previous calculations are valid. To perform similar calculations to the octahedral subsection, it will only be considered the general tetragonal case, where the pairs of ligand angles are given next

$$\begin{gathered} \left(\theta_i', \phi_i'\right) = \left(\tfrac{\pi}{2}, 0\right), \left(\tfrac{\pi}{2}, \tfrac{\pi}{2}\right), \left(\tfrac{\pi}{2}, \pi\right), \left(\tfrac{\pi}{2}, \tfrac{3\pi}{2}\right) \; ; \; i = \{1, \cdots, 6\}, \\ \left(\theta_j', \phi_j'\right) = (0,0), (\pi, 0) \; ; \; j = \{1, 2\}. \end{gathered} \tag{C.23}$$

Again, considering the selection rules given before and the ligand angles above, we find that the symmetry terms, q_{lm} for the D_{4h} symmetry are

$$\begin{aligned} q_{00} &= \frac{Ze^2}{a} 4\sqrt{\pi}\left\{2+\frac{1}{\beta}\right\}, \\ q_{20} &= \frac{Ze^2}{a^3} 4\sqrt{\frac{\pi}{5}}\left\{-1+\frac{1}{\beta^3}\right\}, \\ q_{40} &= \frac{Ze^2}{a^5}\frac{2}{3}\sqrt{\pi}\left\{\frac{3}{2}+\frac{2}{\beta^5}\right\}, \\ q_{4\pm4} &= \frac{Ze^2}{a^5}\frac{\sqrt{70\pi}}{6}. \end{aligned} \tag{C.24}$$

Using the selection rules for the $3-j$ symbols C.16, one can obtain the matrix elements for the tetragonal symmetry

$$\begin{aligned} \langle 2\pm2|\, V_{CF}(\vec{r})\, |2\pm2\rangle &= \frac{4}{7}\frac{Ze^2}{a^3}\left\{1-\frac{1}{\beta^3}\right\}\left\langle r^2\right\rangle + \frac{1}{21}\frac{Ze^2}{a^5}\left\{\frac{3}{2}-\frac{2}{\beta^5}\right\}\left\langle r^4\right\rangle, \\ \langle 2\pm1|\, V_{CF}(\vec{r})\, |2\pm1\rangle &= \frac{2}{7}\frac{Ze^2}{a^3}\left\{-1+\frac{1}{\beta^3}\right\}\left\langle r^2\right\rangle - \frac{4}{21}\frac{Ze^2}{a^5}\left\{\frac{3}{2}+\frac{2}{\beta^5}\right\}\left\langle r^4\right\rangle, \\ \langle 2\,0|\, V_{CF}(\vec{r})\, |2\,0\rangle &= \frac{4}{7}\frac{Ze^2}{a^3}\left\{-1+\frac{1}{\beta^3}\right\}\left\langle r^2\right\rangle + \frac{2}{7}\frac{Ze^2}{a^5}\left\{\frac{3}{2}+\frac{2}{\beta^5}\right\}\left\langle r^4\right\rangle, \\ \langle 2\pm2|\, V_{CF}(\vec{r})\, |2\mp2\rangle &= \frac{5}{6}\frac{Ze^2}{a^5}\left\langle r^4\right\rangle. \end{aligned} \tag{C.25}$$

Next, we need to write the energy matrix for this case. To do that, we are going to use a potential matrix for the symmetry D_{4h} written on the basis of cubic harmonics [32]. Then, using some conversion relations for d orbitals [141], the first matrix can be written on the spherical harmonics basis, as the one done in the O_h case. First, there are the conversion relations from cubic harmonics to spherical harmonics for the d orbitals, in a more complete way than the one presented in Appendix B:

$$\begin{aligned} d_{z^2} &= \sqrt{\frac{15}{4\pi}}\frac{3z^2-r^2}{2r^3\sqrt{3}} = Y_{20}, \\ d_{xz} &= \sqrt{\frac{15}{4\pi}}\frac{xz}{r^2} = \frac{1}{\sqrt{2}}(Y_{2-1}-Y_{21}), \\ d_{yz} &= \sqrt{\frac{15}{4\pi}}\frac{yz}{r^2} = \frac{i}{\sqrt{2}}(Y_{2-1}+Y_{21}), \\ d_{xy} &= \sqrt{\frac{15}{4\pi}}\frac{xy}{r^2} = \frac{i}{\sqrt{2}}(Y_{2-2}-Y_{22}), \\ d_{x^2-y^2} &= \sqrt{\frac{15}{4\pi}}\frac{x^2-y^2}{2r^2} = \frac{1}{\sqrt{2}}(Y_{2-2}+Y_{22}). \end{aligned} \tag{C.26}$$

The cubic base energy matrix is given by

$$H_C^{D_{4h}} = \begin{pmatrix} 6Dq+2Ds-Dt & 0 & 0 & 0 & 0 \\ 0 & 6Dq-2Ds-6Dt & 0 & 0 & 0 \\ 0 & 0 & -4Dq+2Ds-Dt & 0 & 0 \\ 0 & 0 & 0 & -4Dq-Ds+4Dt & 0 \\ 0 & 0 & 0 & 0 & -4Dq-Ds+4Dt \end{pmatrix} \tag{C.27}$$

Through this, it is possible to perform a base transformation to obtain, from C.27 a matrix in the spherical harmonics basis, making it possible to perform some comparison with the O_h case, thus, obtaining the required relations for the crystal field parameters in tetragonal symmetry (Dq, Ds, Dt). Therefore, for the transformation, the following matrix will be used:

$$T = \begin{pmatrix} \frac{1}{\sqrt{2}} & 0 & 0 & 0 & \frac{1}{\sqrt{2}} \\ 0 & 0 & 1 & 0 & 0 \\ \frac{i}{\sqrt{2}} & 0 & 0 & 0 & -\frac{i}{\sqrt{2}} \\ 0 & \frac{1}{\sqrt{2}} & 0 & -\frac{1}{\sqrt{2}} & 0 \\ 0 & \frac{i}{\sqrt{2}} & 0 & \frac{i}{\sqrt{2}} & 0 \end{pmatrix}. \tag{C.28}$$

Finally, after the base transformation, we have the potential matrix for the crystal field in the D_{4h} symmetry

$$\begin{pmatrix} Dq+2Ds-Dt & 0 & 0 & 0 & 5Dq \\ 0 & -4Dq-Ds+4Dt & 0 & 0 & 0 \\ 0 & 0 & 6Dq-2Ds-6Dt & 0 & 0 \\ 0 & 0 & 0 & -4Dq-Ds+4Dt & 0 \\ 5Dq & 0 & 0 & 0 & Dq+2Ds-Dt \end{pmatrix}. \tag{C.29}$$

If the Ds and Dt are manually brought to zero, we get something very similar to the O_h case, but it is necessary to confirm that the Dq parameter here is the same as in the octahedral case, for this the following relations can be used.

$$Dq + 2Ds - Dt = \langle 2\pm 2|\, V_{CF}(\vec{r})\, |2 \pm 2\rangle\,, \tag{C.30.a}$$

$$-4Dq - Ds + 4Dt = \langle 2\pm 1|\, V_{CF}(\vec{r})\, |2 \pm 1\rangle\,, \tag{C.30.b}$$

$$6Dq - 2Ds - 6Dt = \langle 2\, 0|\, V_{CF}(\vec{r})\, |2\, 0\rangle\,, \tag{C.30.c}$$

$$5Dq = \langle 2\pm 2|\, V_{CF}(\vec{r})\, |2 \mp 2\rangle\,. \tag{C.30.d}$$

From C.30.d we can confirm that the Dq present in the tetragonal case is the same as in the octahedral case. But to be able to perform the theoretical calculations present in this work, it is necessary to establish the values of Ds and Dt. Then, using C.17, C.18 into C.30.a, C.30.b, C.30.c and C.30.d we get the following.

$$\begin{gathered} Dt = \tfrac{2}{21}\tfrac{Ze^2}{a^5}\left\langle r^4\right\rangle \left\{1 - \tfrac{1}{\beta^5}\right\}, \\ Ds = \tfrac{2}{7}\tfrac{Ze^2}{a^3}\left\langle r^2\right\rangle \left\{1 - \tfrac{1}{\beta^3}\right\} + \tfrac{2}{7}\tfrac{Ze^2}{a^5}\left\langle r^4\right\rangle \left\{-1 + \tfrac{1}{\beta^5}\right\}, \\ Dq = \tfrac{1}{6}\tfrac{Ze^2}{a^5}\left\langle r^4\right\rangle. \end{gathered} \tag{C.31}$$

Finally, if we tend the distortion parameter to 1, there is only the Dq term left, so the O_h condition is satisfied. Also, we can write when the distortion tends to ∞, corresponding to the square planar symmetry, thus

$$Dt = \tfrac{2}{21}\tfrac{Ze^2}{a^5}\left\langle r^4\right\rangle ,$$

$$Ds = \tfrac{2}{7}Ze^2\left\{\frac{\left\langle r^2\right\rangle}{a^3} - \frac{\left\langle r^4\right\rangle}{a^5}\right\} , \tag{C.32}$$

$$Dq = \tfrac{1}{6}\tfrac{Ze^2}{a^5}\left\langle r^4\right\rangle .$$

C.3 Square pyramidal (C_{4v}) symmetry

Again, some of the considerations used in the previous cases will be used, but now we will consider a different type of cubic symmetry, the square pyramidal symmetry, represented by Figure 70.

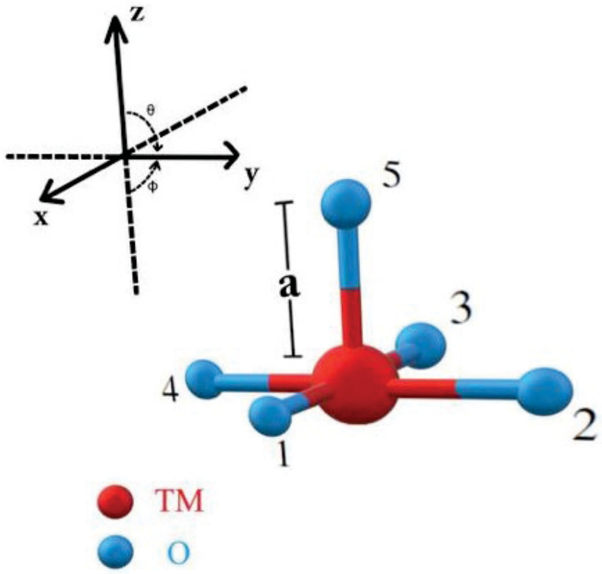

Figure 70 – Scheme showing the metal ion surrounded by its oxygen ligands in C_{4v} symmetry.

In this case, it is necessary to consider the schematic above, which represents the oxygen positions in relation to the central TM, taking into account their position and angles in the Cartesian axis. It is possible to see that in this symmetry there is only 5 ligand oxygen bonded to the central TM. With this, and considering the line of thought used in the previous symmetries, the symmetry factor q_{lm} can be written as:

$$q_{lm} = \frac{Ze^2 4\pi}{a^{l+1}\left(2l+1\right)}\sum_{i=1}^{5}\left(-1\right)^m Y_{l-m}\left(\theta_i^{'}, \phi_i^{'}\right) , \tag{C.33}$$

and the ligand angles $\theta_i^{'}$ and $\phi_i^{'}$ are given by:

$$\left(\theta_i^{'}, \phi_i^{'}\right) = \left(\frac{\pi}{2}, 0\right), \left(\frac{\pi}{2}, \frac{\pi}{2}\right), \left(\frac{\pi}{2}, \pi\right), \left(\frac{\pi}{2}, \frac{3\pi}{2}\right), \left(0, 0\right) \; ; \; i = \left\{1, \cdots, 5\right\} . \tag{C.34}$$

Finally, again considering the selection rules explained in the octahedral case for l and m due to Wigner's $3-j$ symbols used to obtain the matrix elements, and also using the new group of bonding angles given above, the non-vanishing symmetry terms ,q_{lm}, for the C_{4v} case will be:

$$\begin{aligned} q_{00} &= \frac{Ze^2}{a} 10\sqrt{\pi}, \\ q_{20} &= -\frac{Ze^2}{a^3}\frac{\sqrt{20\pi}}{5}, \\ q_{40} &= \frac{Ze^2}{a^5}\frac{5}{3}\sqrt{\pi}, \\ q_{4\pm4} &= \frac{Ze^2}{a^5}\frac{\sqrt{70\pi}}{6}. \end{aligned} \tag{C.35}$$

Finally, from the selection rules given in equation C.16 and the equation for the matrix elements C.13, one can obtain the non-zero matrix elements for the C_{4v} symmetry, which are:

$$\begin{aligned} \langle 2\pm2| V_{CF}(\vec{r}) |2\pm2\rangle &= \frac{2}{7}\frac{Ze^2}{a^3}\left\langle r^2\right\rangle + \frac{5}{42}\frac{Ze^2}{a^5}\left\langle r^4\right\rangle, \\ \langle 2\pm1| V_{CF}(\vec{r}) |2\pm1\rangle &= -\frac{1}{7}\frac{Ze^2}{a^3}\left\langle r^2\right\rangle - \frac{10}{21}\frac{Ze^2}{a^5}\left\langle r^4\right\rangle, \\ \langle 2\,0| V_{CF}(\vec{r}) |2\,0\rangle &= -\frac{2}{7}\frac{Ze^2}{a^3}\left\langle r^2\right\rangle + \frac{5}{7}\frac{Ze^2}{a^5}\left\langle r^4\right\rangle, \\ \langle 2\pm2| V_{CF}(\vec{r}) |2\mp2\rangle &= \frac{5}{6}\frac{Ze^2}{a^5}\left\langle r^4\right\rangle. \end{aligned} \tag{C.36}$$

As it was done for the D_{4h} symmetry, it is necessary to write the energy matrix for this case. From [64] it is known that the C_{4v} symmetry unfolds into b_1, a_1, b_2 and e states. The numbers coincidently are the same as in the tetragonal case. It is possible to express these states using crystal field parameters like:

$$\begin{aligned} b_1\left(x^2-y^2\right) &\rightarrow \quad +6Dq+2Ds-1Dt \\ a_1\left(z^2\right) &\rightarrow \quad +6Dq-2Ds-6Dt \\ b_2\left(xy\right) &\rightarrow \quad -4Dq+2Ds-1Dt \\ e\left(yz,xz\right) &\rightarrow \quad +6Dq+2Ds-1Dt \end{aligned}$$

These energy values for each state coincide with the energy splitting related to the D_{4h} symmetry. Thus, it is possible to use again the same basis transformation used in the last case, resulting in the following matrix for the crystal field potential, now in C_{4v} symmetry:

$$\begin{pmatrix} Dq+2Ds-Dt & 0 & 0 & 0 & 5Dq \\ 0 & -4Dq-Ds+4Dt & 0 & 0 & 0 \\ 0 & 0 & 6Dq-2Ds-6Dt & 0 & 0 \\ 0 & 0 & 0 & -4Dq-Ds+4Dt & 0 \\ 5Dq & 0 & 0 & 0 & Dq+2Ds-Dt \end{pmatrix}. \tag{C.37}$$

Therefore, as in the case D_{4h}, the matrix elements for the CF potential $V_{CF}\left(\vec{r}\right)$ considering the C_{4v} symmetry can be written in terms of the parameters Dq, Ds and Dt in a way like equations C.30.a–C.30.d :

$$Dq + 2Ds - Dt = \langle 2 \pm 2|\, V_{CF}(\vec{r})\, |2 \pm 2\rangle \,, \tag{C.38.a}$$

$$-4Dq - Ds + 4Dt = \langle 2 \pm 1|\, V_{CF}(\vec{r})\, |2 \pm 1\rangle \,, \tag{C.38.b}$$

$$6Dq - 2Ds - 6Dt = \langle 2\, 0|\, V_{CF}(\vec{r})\, |2\, 0\rangle \,, \tag{C.38.c}$$

$$5Dq = \langle 2 \pm 2|\, V_{CF}(\vec{r})\, |2 \mp 2\rangle \,.. \tag{C.38.d}$$

From C.38.d it is visible that the parameter Dq present here is the same for the tetragonal and octahedral cases. Again, it is required to find out how to write the other two parameters, Ds and Dt in this symmetry. For this, let us consider equations C.18 and C.36 and substituting with values into C.38.a, C.38.b, C.38.c and C.38.d, one obtains, finally, the following relations:

$$\begin{aligned} Dq &= \tfrac{1}{6}\tfrac{Ze^2}{a^5}\left\langle r^4\right\rangle \,, \\ Dt &= \tfrac{1}{21}\tfrac{Ze^2}{a^5}\left\langle r^4\right\rangle = \tfrac{2}{7}Dq, \\ Ds &= \tfrac{1}{7}\tfrac{Ze^2}{a^3}\left\langle r^2\right\rangle \,. \end{aligned} \tag{C.39}$$

APPENDIX D

Group Theory Applied to Molecules

Incorporating concepts from group theory enhances the study of crystal field theory, offering a fresh and valuable perspective for theoretically interpreting essential characteristics, especially in the investigation of transition metal oxides. Since a significant focus of this work lies on interpreting spectral results, with meticulous attention to the symmetry aspect of the analyzed compounds, this emphasizes the importance of integrating knowledge about group theory applied to molecules, thus building a more comprehensive analysis of the results and bringing a better understanding about the electronic structure of the transition metal oxides.

D.1 Splitting of atomic levels in a crystal field

Let us begin by considering atoms exposed to a null field, which is equivalent to treating an isolated atom in free space. In this scenario, the group representing the situation is that of a sphere [63]. To determine the group representations, spherical harmonics are traditionally employed:

$$Y_l^m\left(\theta,\phi\right)\ \alpha\ P_l^m\left(\theta\right)e^{im\phi}. \tag{D.1}$$

A relationship can be written as [63]:

$$P_R Y_l^m\left(\theta,\phi\right)=\sum_{m'} Y_l^{m'}\left(\theta,\phi\right)D_{m',m}^{(l)}\left(R\right). \tag{D.2}$$

where the rotation operator P_R acts on the spherical harmonics as $P_R f\left(x\right)=f\left(R^{-1}x\right)$ for a rotation of the form defined by an angle α around the z-axis. The effect of this rotation on the spherical harmonics is as follows:

$$P_\alpha Y_l^m(\theta,\phi) = Y_l^m(\theta,\phi-\alpha) = e^{-im\alpha} Y_l^m(\theta,\phi)\,, \tag{D.3}$$

and it demonstrates that $Y_l^m(\theta,\phi)$ is an eigenfunction of the rotation operator with an angle α around the z-axis having eigenvalues $e^{-im\alpha}$.

Upon comparing Equation D.2 with Equation D.3, it becomes evident that the representation of this particular rotation is a diagonal matrix [63]:

$$D^{(l)}(\alpha) = \begin{pmatrix} e^{-il\alpha} & 0 & \dots & 0 \\ 0 & e^{-i(l-1)\alpha} & \dots & 0 \\ \vdots & \vdots & \ddots & \vdots \\ 0 & 0 & \dots & e^{il\alpha} \end{pmatrix} \tag{D.4}$$

The character related to this representation can be expressed using the following equation.

$$\chi^l(\alpha) = TrD^l(\alpha) = e^{-il\alpha} + \ldots + e^{il\alpha}$$

This summation can be understood as a geometric progression:

$$\chi^{(l)}(\alpha) = e^{-il\alpha} \sum_{k=0}^{2l} \left(e^{i\alpha}\right)^k = e^{-il\alpha} \frac{e^{i(2l+1)\alpha} - 1}{e^{i\alpha} - 1} = \frac{e^{i\left(l+\frac{1}{2}\right)\alpha} - e^{-i\left(l+\frac{1}{2}\right)\alpha}}{e^{i\frac{\alpha}{2}} - e^{-i\frac{\alpha}{2}}}$$

Simplifying, we obtain [63]:

$$\chi^{(l)}(\alpha) = \frac{\sin\left[\left(l+\frac{1}{2}\right)\alpha\right]}{\sin\left(\frac{\alpha}{2}\right)}. \tag{D.5}$$

All rotations with an angle α belong to the same class, regardless of the rotation axis. Consequently, when an atom is subjected to a non-spherical field, it becomes important to identify the rotations that maintain the system invariant.

Again, let's consider the octahedral scheme in Figure 62. The symmetry group that this molecule belongs is the O_h, which have the character table given below:

O_h	E	$6C_4$	$3C_4^2$	$8C_3$	$6C_2$	i	$6S_4$	$3\sigma_h$	$8S_6$	$6\sigma_d$
A_{1g}	1	1	1	1	1	1	1	1	1	1
A_{2g}	1	-1	1	1	-1	1	-1	1	1	-1
E_g	2	0	2	-1	0	2	0	2	-1	0
T_{1g}	3	1	-1	0	-1	3	1	-1	0	-1
T_{2g}	3	-1	-1	0	1	3	1	-1	0	-1
A_{1u}	1	1	1	1	1	-1	-1	-1	-1	-1
A_{2u}	1	-1	1	1	-1	-1	1	-1	-1	1
E_u	2	0	2	-1	0	-2	0	-2	1	0
T_{1u}	3	1	-1	0	-1	-3	-1	1	0	1
T_{2u}	3	-1	-1	0	1	-3	1	1	0	-1

Now, let's consider the case $l = 2$ (d orbitals) and utilize Equation D.5, to determine how the orbitals are represented in terms of the irreducible representations of the O_h symmetry group.

O_h	E	$6C_4$	$3C_4^2$	$8C_3$	$6C_2$	i	$6S_4$	$3\sigma_h$	$8S_6$	$6\sigma_d$
Γ^d	5	-1	1	-1	1	5	-1	1	-1	1

Making the correct calculations, one can obtain that the representation Γ^d can unfold in the symmetry operations e_g and t_{2g} in a way like $\Gamma^d = E_g \oplus T_{2g}$, as represented in Figure 71.

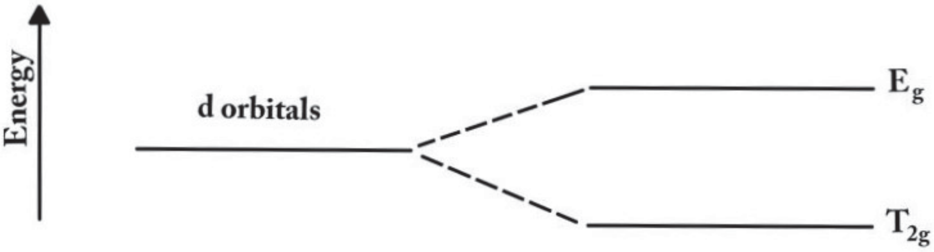

Figure 71 – Unfolding of a d orbital under influence of a crystal field with octahedral (O_h) symmetry.

Continuing with the octahedrum for the calculations which simplifies explanations, we represent the basis functions $\psi_{lm}\left(\vec{r}-\vec{r}_n\right)$, where $\vec{r}_n$ indicates the center where the six ligand atoms are displayed. When these functions are spanned, the result is [63]:

$$P_R\psi_{lm}\left(\vec{r}-\vec{r}_n\right) = \psi_{lm}\left(R^{-1}\vec{r}-\vec{r}_n\right) = \psi_{lm}\left[R^{-1}\left(\vec{r}-\vec{r}_n\right)\right],$$

considering $\vec{r}_{nR} \equiv R_{\vec{r}n}$, using the following equation:

$$P_R\Psi_\nu^{(n)} = \sum_{\mu=1}^{ln} \Psi_\mu^{(n)} D_{\mu\nu}^{(n)}\left(R\right). \tag{D.6}$$

Consequently,

$$P_R\varphi_{lm}\left(\vec{r}-\vec{r}_n\right) = \varphi_{lm}\left[R^{-1}\left(\vec{r}-\vec{r}_{nR}\right)\right] = \sum_{m'} \varphi_{lm'}\left(\vec{r}-\vec{r}_{nR}\right) D_{m'm}^{(l)}, \tag{D.7}$$

which can also be written as:

$$P_R\varphi_{lm}\left(\vec{r}-\vec{r}_n\right) = \sum_{m'n'} \varphi_{lm'}\left(\vec{r}-\vec{r}_{n'}\right) \tilde{D}_{m'm,n'n}^{(l)}\left(R\right). \tag{D.8}$$

Comparing Equation D.7 with Equation D.8,

$$\tilde{D}_{m'm,n'n}^{(l)}\left(R\right) = D_{m'm,n'n}^{(l)}\left(R\right)\delta_{n'n_R}. \tag{D.9}$$

Denoting $\chi_c^{(l)}(R)$ as the characters related to the shell atoms for a given angular momentum l,

$$\chi_c^{(l)}(R) = \sum_{mn} \tilde{D}^{(l)}_{m'm,n'n}(R) = \left(\sum_m D^l_{mm}(R)\right)\left(\sum_n \delta_{nn}\right). \tag{D.10}$$

The first factor in parentheses is $\chi^l(R)$, and the second factor gives the number of atoms that did not change position when the R operation was applied. Since $\chi^0(R) = 1$, for any R,

$$\chi_c^0 = \sum_n \delta_{nn_R}. \tag{D.11}$$

Thus, Equation D.10 can be written as

$$\chi_c^l(R) = \chi^l(R)\,\chi_c^0(R). \tag{D.12}$$

Finally, in the case of d orbitals ($l = 2$), the characters are:

O_h	E	$6C_4$	$3C_4^2$	$8C_3$	$6C_2$	i	$6S_4$	$3\sigma_h$	$8S_6$	$6\sigma_d$
$\chi^{l=2}$	5	-1	1	-1	1	5	-1	1	-1	1
χ_c^2	30	-2	2	0	0	0	0	4	0	2

Denoting by Γ^d_{shell}, the correspondent representation of the characters χ_c^2, it is possible to see all possible symmetry operations present in an octahedrum when taking into account the d orbital.

D.2 Multielectronic states

The interplay between multielectronic states and monoelectronic configurations allows us to establish a correlation diagram that bridges the gap between the free ion and the ion subjected to an infinite interaction.

D.2.1 Ligand field theory

In a crystalline environment, the spin multiplicity of the total state of a free ion remains preserved. Let us take the example of a d^2 configuration subjected to an octahedral field. Figure 72 illustrates all the permissible terms for this configuration and how they can be unfolded [63].

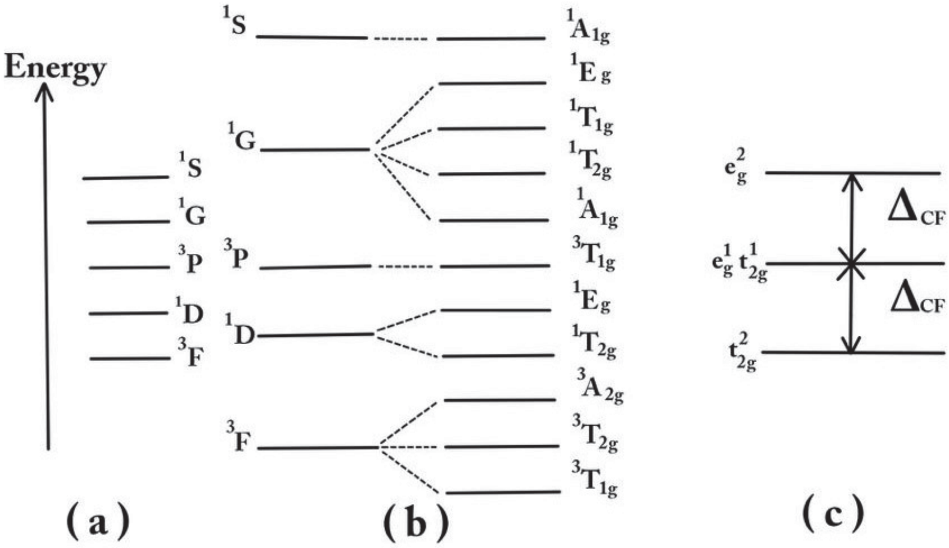

Figure 72 – (a) Multielectronic state of a ion without the presence of a field. (b) Unfolding of the multielectronic state under the influence of a weak octahedral field. (c) Possible configurations for the ion on the strong octahedral field limit.

There are three possible electron configurations: (1) both electrons in the t_{2g} orbital, (2) one electron in t_{2g} and one in e_g , and (3) both electrons in e_g. Each configuration results in a final state that needs to be accounted for in the direct product of the participating orbitals. Thus, the characters table of the possible products is as follows:

	E	$6C_4$	$3C_4^2$	$8C_3$	$6C_2$	i	$6S_4$	$3\sigma_h$	$8S_6$	$6\sigma_d$
$t_{2g} \otimes t_{2g}$	9	1	1	0	1	9	1	1	0	1
$t_{2g} \otimes e_g$	6	0	-2	0	0	6	0	-2	0	0
$e_g \otimes e_g$	4	0	4	1	0	4	0	4	1	0

If the decomposition is made, it is possible to identify which irreducible representations can be used to represent each operation,

$$t_{2g} \otimes t_{2g} \rightarrow A_{1g} \oplus E_g \oplus T_{1g} \oplus T_{2g}$$
$$t_{2g} \otimes e_g \rightarrow T_{1g} \oplus T_{2g}$$
$$e_g \otimes e_g \rightarrow A_{1g} \oplus A_{2g} \oplus E_g$$

The Pauli's exclusion principle determines whether a state is a singlet or a triplet. When considering the configuration t_{2g}^2, it is possible to visualize the orbital t_{2g} as a group of six boxes, as depicted in Figure 73 [63]:

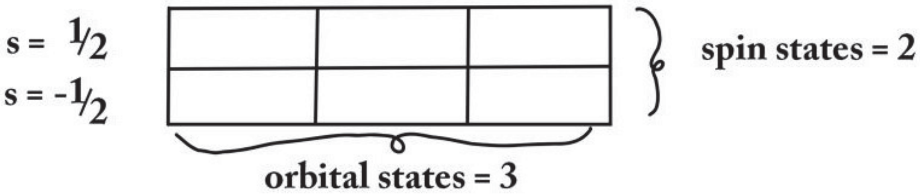

Figure 73 – Visual representation of the t_{2g} orbital considering the number of orbital and spin states.

The number of possible states is given by:

$$\frac{6!}{(6-2)!2!} = 15.$$

The total degeneracy of the t_{2g} orbital is 15 and can be distributed as [63]:

$$^{a}A_{1g}\ ,\ ^{b}E_{g}\ ,\ ^{c}T_{1g}\ ,\ ^{d}T_{2g}$$

Since the orbitals degeneracy are: for a_{1g} 1, e_g 2, t_{1g} 3 and t_{2g} 3, the equation

$$a + 2b + 3c + 3d = 15, \tag{D.13}$$

must be satisfied with a, b, c and d being 1 or 3. The possible solutions are:

	a	b	c	d
1.	1	1	1	3
2.	1	1	3	1
3.	3	3	1	1

The possible sets of total states generated by t_{2g}^2 are:

$$^{1}A_{1g}\ ^{1}E_{g}\ ^{1}T_{1g}\ ^{3}T_{2g};$$
$$^{1}A_{1g}\ ^{1}E_{g}\ ^{3}T_{1g}\ ^{1}T_{2g};$$
$$^{3}A_{1g}\ ^{3}E_{g}\ ^{1}T_{1g}\ ^{1}T_{2g}.$$

A similar procedure is followed for e_g^2, however, in this case, the electrons are distributed across four equivalent boxes. The possible sets for this configuration are as follows:

$$^{1}A_{1g}\ ^{3}A_{2g}\ ^{1}E_{g};$$
$$^{3}A_{1g}\ ^{1}A_{2g}\ ^{3}E_{g}.$$

Moving on to the configuration $t_{2g}e_g$, one electron can occupy any of the six possibilities while the other can independently occupy any of the four possibilities. This leads to a total of $6 \cdot 4 = 24$ possibilities. By applying the same process as explained before, we obtain the following.

$$^{1}T_{1g}\ ,\ ^{3}T_{1g}\ ,\ ^{1}T_{2g}\ ,\ ^{3}T_{2g}.$$

The task now is to determine the spin multiplicity of the states formed from the electronic interactions of the configurations e_g^2 and t_{2g}^2. Considering the case of e_g^2, let us reduce the symmetry from O_h to D_{4h}. To do this, we consider an octahedron of the same type as before, MX_6. When the distance between the apical ligands in relation to the central atom is varied, the symmetry is reduced from O_h to D_{4h}. During this process, some operations of octahedral symmetry are lost, while others are transformed into different classes. As a result, the characters of the e_g representation under O_h operations disassemble into the representations of the D_{4h} operations, such as:

D_{4h}	E	$2C_4$	C_2	$2C_2^{'}$	$2C_2^{''}$	i	$2S_4$	σ_h	$2\sigma_v$	$2\sigma_d$
$e_g\,(O_h)$	2	0	2	2	0	2	0	2	2	0

The characters above break up into $a_{1g} \oplus b_{1g}$ of D_{4h}. The degeneracy of the e_g orbital under O_h symmetry is lifted, leading to the formation of the orbitals a_{1g} and b_{1g} under D_{4h} symmetry, with the orbital b_{1g} having the lower energy. Thus, the two electrons that occupie the e_g orbital can now be redistributed among the configurations b_{1g}^2, $b_{1g}a_{1g}$ or a_{1g}^2.

	$\otimes$	$(2S+1)\ possibilidades$
b_{1g}^2	A_{1g}	$^1A_{1g}$
$b_{1g}a_{1g}$	B_{1g}	$^1B_{1g},^3B_{1g}$
a_{1g}^2	A_{1g}	$^1A_{1g}$

The total number of possible combinations under O_h, which is 4, is kept in the D_{4h} symmetry.

The behaviour analysis of the total state, when the symmetry is reduced, results in the relation between the O_h and D_{4h} states:

$$O_h \to D_{4h}$$
$$A_{1g} \to A_{1g}$$
$$A_{2g} \to B_{1g}$$
$$E_g \to \begin{cases} A_{1g} \\ B_{1g} \end{cases}$$

The spin degeneracy remains unchanged during symmetry reduction. For instance, if A_{1g} is a singlet in O_h, it retains its singlet nature in D_{4h}. Furthermore, regardless of the spin multiplicity of E_g in O_h, the unfolded states A_{1g} and B_{1g} must have the same multiplicity in D_{4h}. Let us consider a triplet for E_g under the O_h symmetry. In D_{4h}, the unfolding yields two triplets, one in A_{1g} and the other in B_{1g}.

$$^3E_g \to ^3A_{1g} \oplus ^3B_{1g}$$

Since A_{1g} is generated by the configurations a_{1g}^2 and b_{1g}^2, the triplet state is not allowed by the Pauli's principle. Consequently, both states A_{1g} in D_{4h} cannot be singlets. Due to this fact, the states A_{1g} and E_g in O_h can only be singlets. Therefore, the possible total states that arise from e_g^2 in O_h are solely:

$$^1A_{1g}\ ,\ ^3A_{2g}\ ,\ ^1E_g$$

In this case, when the symmetry is reduced, the possible total states in D_{4h} are, $^1A_{1g}$, $^3B_{1g}$, $^1A_{1g}$ and $^1B_{1g}$. Continuing in a similar manner, we obtain the possible total states for the configurations t_{2g}^2:

$$^1A_{1g}\ ,\ ^1E_g\ ,\ ^1T_{2g},\ ^3T_{1g}$$

and $t_{2g}e_g$:

$$^1T_{1g}\ ,\ ^1T_{2g}\ ,\ ^3T_{1g},\ ^3T_{2g}$$

D.2.2 The Jahn-Teller effect

The Jahn-Teller effect, also known as Jahn-Teller distortion, refers to the geometrical distortion of molecules and ions resulting from specific electron configurations. This effect is most commonly observed in octahedral complexes of transition metals [63]. The distortion typically involves the elongation of bonds with ligands lying along the z-axis, but occasionally it can also result in shortening of these bonds. Elongations reduce the electrostatic repulsion between the electron pair on the Lewis basis ligand and any electrons in orbitals with a z component, leading to a decrease in the energy of the complex. Importantly, the distortion maintains the inversion center of the molecule. The Jahn-Teller effect is most pronounced when an odd number of electrons occupy the e_g orbitals. This scenario arises in complexes with configurations d^9, low-spin d^7 or high-spin d^4, all of which have doubly degenerate ground states, where high-spin fills d orbitals to maximize spin, whereas low-spin prioritizes electron pairing before filling higher energy levels. In such compounds, the e_g orbitals involved in the degeneracy are directed towards the ligands, resulting in significant energetic stabilization upon distortion. The effect can also occur due to degeneracy caused by electrons in the t_{2g} orbitals. However, in such cases, the effect is less noticeable, as there is minimal lowering of repulsion when the ligands are moved further away from the t_{2g} orbitals, which do not directly point at the ligands. Similarly, in tetragonal complexes, the distortion is subtle because there is less potential for stabilization because the ligands are not directly oriented toward the orbitals.

APPENDIX E

Computational Implementation

Several specific, yet crucial considerations were incorporated into the codes to adequately address the effects studied in this dissertation. By adding certain extra considerations to the programs, it was possible to achieve the results presented in this work. Here, these additional details will be prompted.

E.1 *Quanty*

In *Quanty* [57], various versions of the code are dedicated to computing results for X-ray absorption spectroscopy, including spectra, expected values, and eigenvectors. These capabilities allow for a wide range of results, providing robust evidence of the influence of the effects explored in this work. However, implementing these effects in the code is not straightforward. For a better understating of this powerful toll, this section will be divided into explaining the basic concepts, examples of these basic concepts, and the illustration of how the implementation of the effects studied in this dissertation was given.

E.1.1 Basic concepts of *Quanty*

First it is necessary to define the basis set of the studied system. *Quanty* needs, at a minimum, the number of Fermionic and Bosonic modes. For clarity and ease in creating operators in subsequent steps, these modes can be grouped into shells. For instance, a d-shell can be characterized by two groups: one that contains electrons with spin up and the other with spin down.

Another crucial component are Operators, defined in *Quanty* using second quantization. Any operator can be expressed in a general form like:

$$\begin{aligned}\hat{O} = {} & \alpha^{(0,0)}\mathbb{1} \\ & + \sum_i \left[\alpha_i^{(1,0)} a_i^\dagger + \alpha_i^{(0,0)} a_i\right] \\ & + \sum_{ij} \left[\alpha_{ij}^{(2,0)} a_i^\dagger a_j^\dagger + \alpha_{ij}^{(1,1)} a_i^\dagger a_j + \alpha_{ij}^{(0,2)} a_i a_j\right] + \cdots\end{aligned}$$

For example, the creation operator on the 0 orbital can be written using the *NewOperator()* function. *Quanty* also allows the creation of wave functions and the calculation of their related eigenstates, as well as the determination of expectation values for a given wave function. Wave functions can be generated from a string containing 1's (occupied orbitals) and 0's (unoccupied orbitals). For instance, a wave function representing a single electron in a p_x orbital with a spin down state is created considering the number of Fermionic and Bosonic modes, and the definition on how the orbitals are occupied, for example, 000010.

Given an operator $\hat{O}$, one can calculate the eigenstates related to the operator using the *Eigensystem()* function. This function uses iterative methods to obtain results and requires a starting point as the main input. It is not mandatory to have a set of starting functions as input, but rather a set of restrictions, as used in this work. For example, to obtain the eigenstates related to the Hamiltonian $\hat{H}$ of a system with a basis size of $N_{psis} = 210$ states, considering that all orbitals in the d shell are filled with an occupation range of 2 to 2, such as:

```
StartRestrictions = {NFermions, NBosons, {"1111111111",2,2}}
Psi_list_d = Eigensystem(H, StartRestrictions, 210)
```

where NFermions and NBosons are the number of Fermionic and Bosonic modes. Therefore, with this information, one can calculate expectation values, mathematically expressed as:

$$\langle \psi_i | \hat{O} | \psi_j \rangle = \int_{r1} \int_{r2} \cdots \int_{r_n} \psi_i^* \left(\vec{r}_1, \vec{r}_2, \cdots, \vec{r}_n\right) \hat{O} \psi_j \left(\vec{r}_1, \vec{r}_2, \cdots, \vec{r}_n\right) dr_1 dr_2 \cdots dr_n$$

In *Quanty*, complex conjugates are automatically assumed, and expectation values are implemented simply as the multiplication of single, or sets, of wave functions and operators. For example, to find the expected energy value of a given system , it is sufficient to multiply it by the wave functions obtained, such as:

```
for i, Psi in ipairs(Psi_list_d) do
    exp_val_E = Psi * Hamiltonian * Psi
end
```

Finally, considering the spectroscopy technique under study, obtaining spectra in *Quanty* can be done in two ways: by obtaining it step by step, in other words, in a more "old school" way, or using the method already implemented in *Quanty* way, the *CreateSpectra()* function. This function takes the Hamiltonian $\hat{H}$, the transition operator $\hat{T}$ that better describes the transition related to the specific technique that is being simulated, and the list of calculated wave functions as arguments. The spectrum can be further customized by specifying an energy range, the number of points, Lorentzian broadening for simulating lifetime, and the restrictions established to the specific type of spectra desired.

E.1.2 Implementing the basic concepts of *Quanty*

Figures 74–84 present the basic concepts that are needed to properly use *Quanty*. Beginning with the most simple things such as defining a shell, creating an operator or a wave function, as presented in Figures 74, 75 and 76. Or even more elaborated aspects, like the creation of the basis of the system considered, calculating the eigenvalues of the system's Hamiltonian and finally creating the spectra to the considered technique, as showcased in Figures 77, 78 and 79.

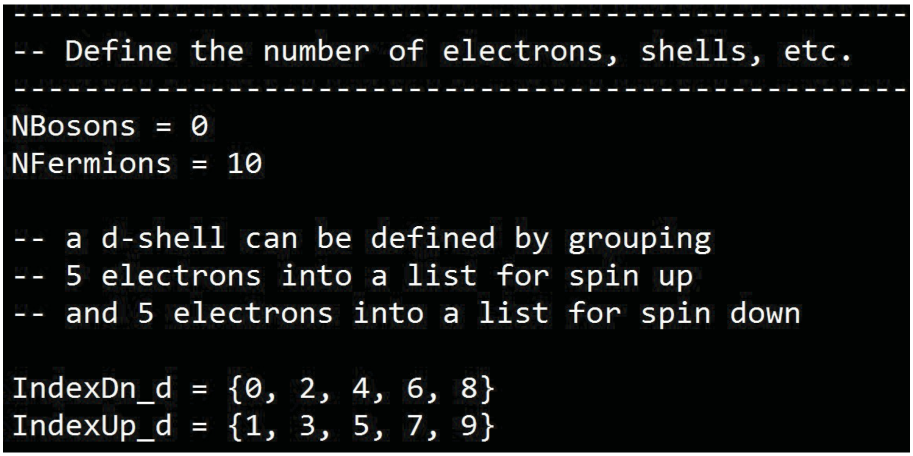

```
--------------------------------------------------
-- Define the number of electrons, shells, etc.
--------------------------------------------------
NBosons = 0
NFermions = 10

-- a d-shell can be defined by grouping
-- 5 electrons into a list for spin up
-- and 5 electrons into a list for spin down

IndexDn_d = {0, 2, 4, 6, 8}
IndexUp_d = {1, 3, 5, 7, 9}
```

Figure 74 – This figure visually explains the crucial step of grouping Fermionic modes within a d-shell in *Quanty*. This grouping is fundamental for accurately defining the basis set of the studied system.

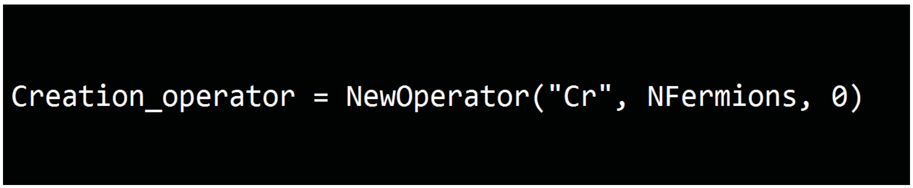

```
Creation_operator = NewOperator("Cr", NFermions, 0)
```

Figure 75 – Illustration of creating a creation operator in *Quanty*.

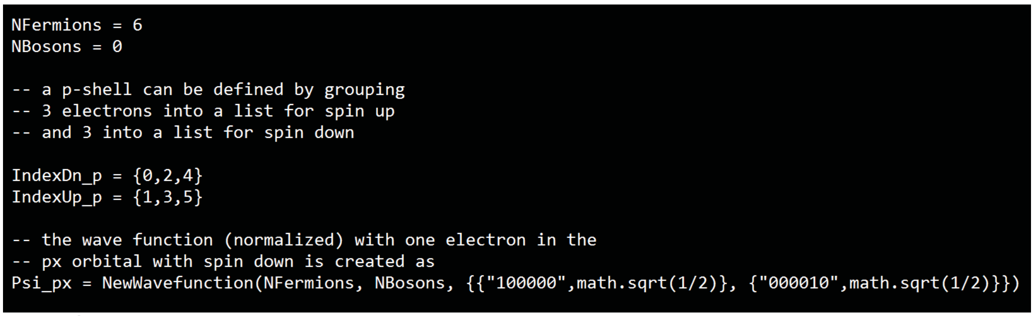

```
NFermions = 6
NBosons = 0

-- a p-shell can be defined by grouping
-- 3 electrons into a list for spin up
-- and 3 into a list for spin down

IndexDn_p = {0,2,4}
IndexUp_p = {1,3,5}

-- the wave function (normalized) with one electron in the
-- px orbital with spin down is created as
Psi_px = NewWavefunction(NFermions, NBosons, {{"100000",math.sqrt(1/2)}, {"000010",math.sqrt(1/2)}})
```

Figure 76 – Creation of a wave function for a single electron in a p_x orbital with a spin down state.

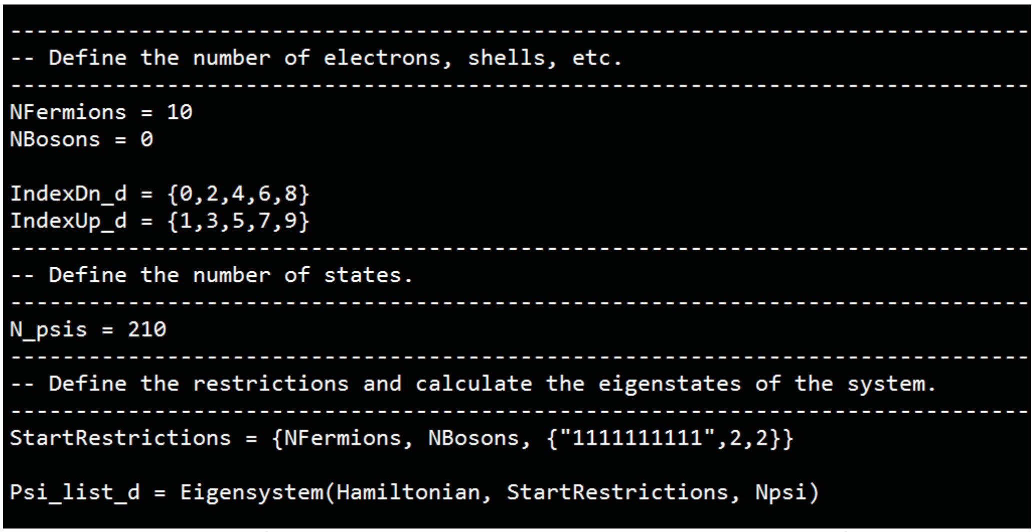

```
--------------------------------------------------------------------------------
-- Define the number of electrons, shells, etc.
--------------------------------------------------------------------------------
NFermions = 10
NBosons = 0

IndexDn_d = {0,2,4,6,8}
IndexUp_d = {1,3,5,7,9}
--------------------------------------------------------------------------------
-- Define the number of states.
--------------------------------------------------------------------------------
N_psis = 210
--------------------------------------------------------------------------------
-- Define the restrictions and calculate the eigenstates of the system.
--------------------------------------------------------------------------------
StartRestrictions = {NFermions, NBosons, {"1111111111",2,2}}

Psi_list_d = Eigensystem(Hamiltonian, StartRestrictions, Npsi)
```

Figure 77 – Specifying input for eigenstate calculation in *Quanty*.

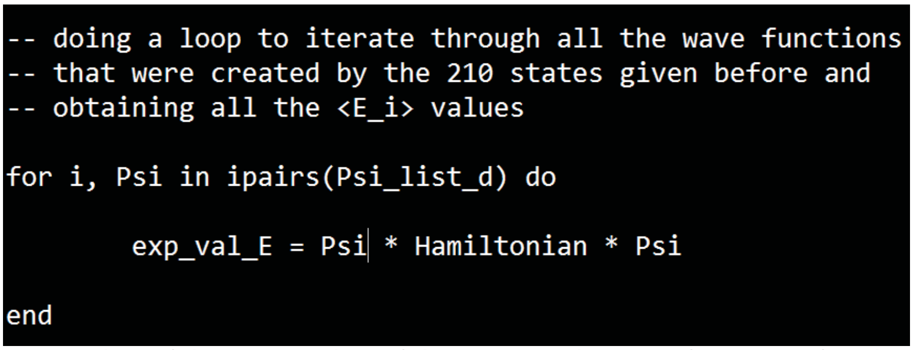

```
-- doing a loop to iterate through all the wave functions
-- that were created by the 210 states given before and
-- obtaining all the <E_i> values

for i, Psi in ipairs(Psi_list_d) do

        exp_val_E = Psi * Hamiltonian * Psi

end
```

Figure 78 – Illustration of the calculation of the expected value of energy of a given system in *Quanty*.

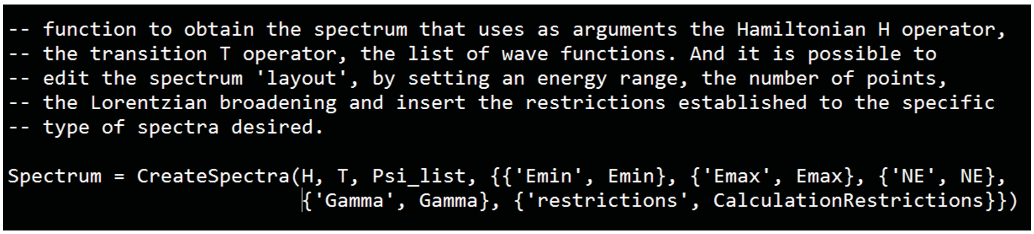

```
-- function to obtain the spectrum that uses as arguments the Hamiltonian H operator,
-- the transition T operator, the list of wave functions. And it is possible to
-- edit the spectrum 'layout', by setting an energy range, the number of points,
-- the Lorentzian broadening and insert the restrictions established to the specific
-- type of spectra desired.

Spectrum = CreateSpectra(H, T, Psi_list, {{'Emin', Emin}, {'Emax', Emax}, {'NE', NE},
                         {'Gamma', Gamma}, {'restrictions', CalculationRestrictions}})
```

Figure 79 – Creating the a spectrum in *Quanty* with previously defined and obtained parameters such as the Hamiltonian, transition operator and basis size, it also includes the spectrum layout editing.

E.1.3 Implementing the covalence and symmetry effects in *Quanty*

To address the covalence effect, the code incorporates concepts from a software called *Crispy* [142], which utilizes a graphical user interface to calculate core-level spectra using semi-empirical multiplet approaches. In this case, the covalence is accounted by the implementation of the configuration interaction method, where it is considered a number of electronic configurations that commands which kind of configuration it is being considered in the calculations, for example, 1 electronic configuration stands for the ionic state, from 2 electronic configurations and so forth it is being considered electron exchange. Also there are sets of restrictions to let the code "know" when to include the charge transfer effects (Δ and hybridization parameters, for example) in the Hamiltonian evaluation. Figure 80 illustrates the set of restrictions in the code that accounts for covalence effects.

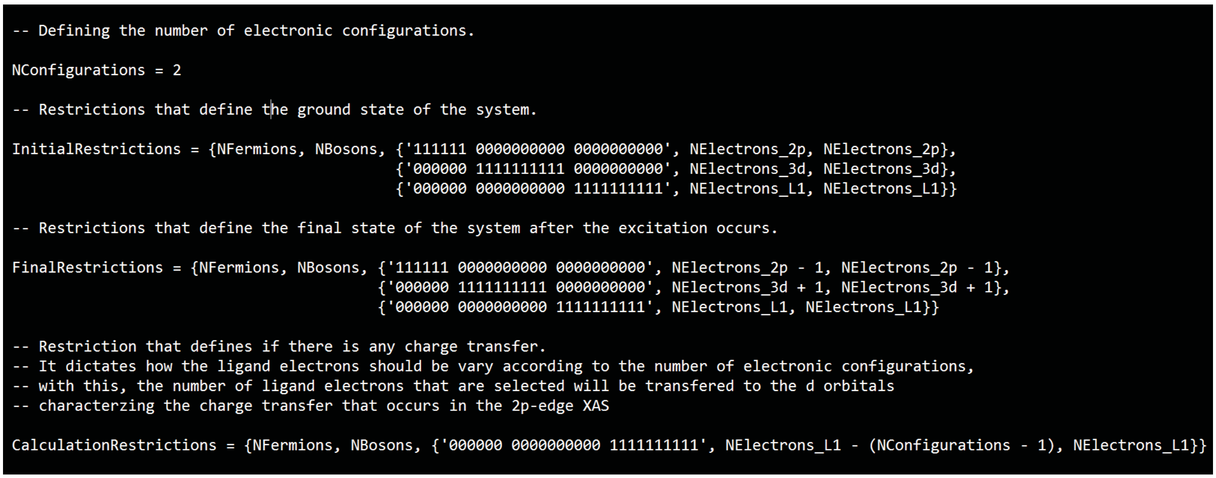

```
-- Defining the number of electronic configurations.

NConfigurations = 2

-- Restrictions that define the ground state of the system.

InitialRestrictions = {NFermions, NBosons, {'111111 0000000000 0000000000', NElectrons_2p, NElectrons_2p},
                                           {'000000 1111111111 0000000000', NElectrons_3d, NElectrons_3d},
                                           {'000000 0000000000 1111111111', NElectrons_L1, NElectrons_L1}}

-- Restrictions that define the final state of the system after the excitation occurs.

FinalRestrictions = {NFermions, NBosons, {'111111 0000000000 0000000000', NElectrons_2p - 1, NElectrons_2p - 1},
                                         {'000000 1111111111 0000000000', NElectrons_3d + 1, NElectrons_3d + 1},
                                         {'000000 0000000000 1111111111', NElectrons_L1, NElectrons_L1}}

-- Restriction that defines if there is any charge transfer.
-- It dictates how the ligand electrons should be vary according to the number of electronic configurations,
-- with this, the number of ligand electrons that are selected will be transfered to the d orbitals
-- characterzing the charge transfer that occurs in the 2p-edge XAS

CalculationRestrictions = {NFermions, NBosons, {'000000 0000000000 1111111111', NElectrons_L1 - (NConfigurations - 1), NElectrons_L1}}
```

Figure 80 – Covalence effects in *Quanty* code. There are three restrictions present here; the first two accounts for the initial and excited states of the system. The third one defines whether there is any charge transfer occurring. It dictates how the ligand electrons should vary according to the number of electronic configurations.

One of the gracious aspects about *Quanty* is the the flexibility to modify its code according to specific needs. That is the reason why it was possible to include the symmetries treated in this dissertation. Originally, *Quanty* only supported O_h and D_{4h} symmetries, among others. To account for symmetry effects, the code utilizes tools for writing crystal field and hybridization operators, crucial components dependent on symmetry in calculations. Two key aspects of the code are relevant here: crystal field and hybridization evaluations. For the crystal field, the potential that describes this interaction in *Quanty* is expanded on the renormalized spherical harmonics basis and denoted as potential $A_{k,m}$. Figure 81 shows the original $A_{k,m}$ values for octahedral and tetragonal symmetries. Although in the case of the O_h symmetry there is no problem in the definition of this potential, for the tetragonal symmetry there are some things that should be considered. For example, it does not account for the distortion parameter β that was shown in Appendix C, and also, not always all three crystal field parameters (Dq, Ds and Dt) are available in the literature. Because of that, a way to define the crystal field parameters in function of Dq (it is more easily found) and also include the distortion parameter to make it more general and applicable to any system that displays the D_{4h} symmetry was developed.

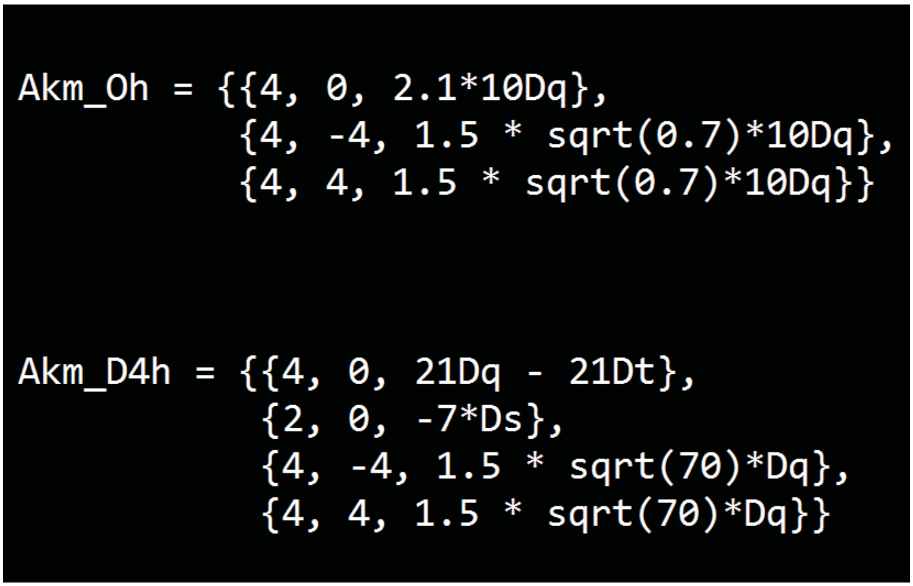

```
Akm_Oh = {{4, 0, 2.1*10Dq},
          {4, -4, 1.5 * sqrt(0.7)*10Dq},
          {4, 4, 1.5 * sqrt(0.7)*10Dq}}



Akm_D4h = {{4, 0, 21Dq - 21Dt},
           {2, 0, -7*Ds},
           {4, -4, 1.5 * sqrt(70)*Dq},
           {4, 4, 1.5 * sqrt(70)*Dq}}
```

Figure 81 – Showcase of how the original effective crystal field potentials are defined for the O_h and D_{4h} symmetries. They are expanded on renormalized spherical harmonics basis.

From this it is possible to make some calculations to obtain the desired potential. Considering $A_{km}\_D_{4h}$:

$$\begin{aligned} A_{4,0} &= 21Dq - 21Dt, \\ A_{2,0} &= -7Ds, \\ A_{4,\underline{4}} &= A_{4,4} = \frac{3}{2}\sqrt{70}Dq. \end{aligned} \tag{E.1}$$

Remembering the results from Appendix C.2 for the values of Dq, Ds and Dt for the

D_{4h} symmetry,

$$\begin{aligned} Dq &= \frac{1}{6}\frac{Ze^2}{a^5}\left\langle r^4\right\rangle, \\ Ds &= \frac{2}{7}\left\{\frac{ze^2}{a^3}\left[1-\frac{1}{\beta^3}\right]\left\langle r^3\right\rangle + \frac{Ze^2}{a^5}\left[-1+\frac{1}{\beta^5}\right]\left\langle r^4\right\rangle\right\}, \\ Dt &= \frac{2}{21}\frac{Ze^2}{a^5}\left[1-\frac{1}{\beta^5}\right]\left\langle r^4\right\rangle. \end{aligned} \tag{E.2}$$

where β represents the distortion parameter of the apical oxygens as it was already delved in Appendix C. So, there will be the following for the $A_{k,m}$'s, since $Dt = \frac{4}{7}Dq\left[1-\frac{1}{\beta^5}\right]$:

$$\begin{aligned} A_{4,0} &= 21Dq - 21\frac{4}{7}Dq\left[1-\frac{1}{\beta^5}\right] \\ &= 21Dq - 12Dq + \frac{12}{\beta^5}Dq \\ &= 9Dq + 12Dq\frac{1}{\beta^5} \\ &= 3Dq\left(3+\frac{4}{\beta^5}\right). \end{aligned} \tag{E.3}$$

In the case of $A_{2,0}$, if $\beta \to 1 : Ds \to 0$, but if $\beta \to \infty$

$$Ds_\infty \to \frac{2}{7}\frac{Ze^2}{a^3}\left\langle r^2\right\rangle - \frac{12}{7}Dq.$$

Thus,

$$\frac{2}{7}\frac{Ze^2}{a^3}\left\langle r^2\right\rangle = Ds_\infty + \frac{12}{7}Dq. \tag{E.4}$$

With this, it is possible to write Ds in terms of this new parameter called Ds_∞ and Dq.

$$Ds = \left(Ds_\infty + \frac{12}{7}Dq\right)\left(1-\frac{1}{\beta^3}\right) + \frac{12}{7}Dq\left(\frac{1}{\beta^5}-1\right). \tag{E.5}$$

And, finally, rewrite $A_{2,0}$ with this new definition,

$$\begin{aligned} A_{2,0} = -7Ds &= (-7Ds_\infty - 12Dq)\left(1-\frac{1}{\beta^3}\right) - 12Dq\left(\frac{1}{\beta^5}-1\right) \\ &= -7Ds_\infty - 12Dq + 12Dq + (7Ds_\infty + 12Dq)\frac{1}{\beta^3} - 12Dq\frac{1}{\beta^5} \\ A_{2,0} &= -7Ds_\infty + (7Ds_\infty + 12Dq)\frac{1}{\beta^3} - 12Dq\frac{1}{\beta^5}. \end{aligned} \tag{E.6}$$

In addition, as shown in this work, both D_{4h} and C_{4v} symmetries have the same crystal field unfolding, which means that the $A_{k,m}$ related to the C_{4v} symmetry is the same as for the D_{4h} case but without the β distortion parameter. Since for this symmetry, it is more easily found the three crystal field parameters (Dq, Ds and Dt coincidentally), the original form of the potential was kept. Thus, Figure 82 illustrates how the crystal

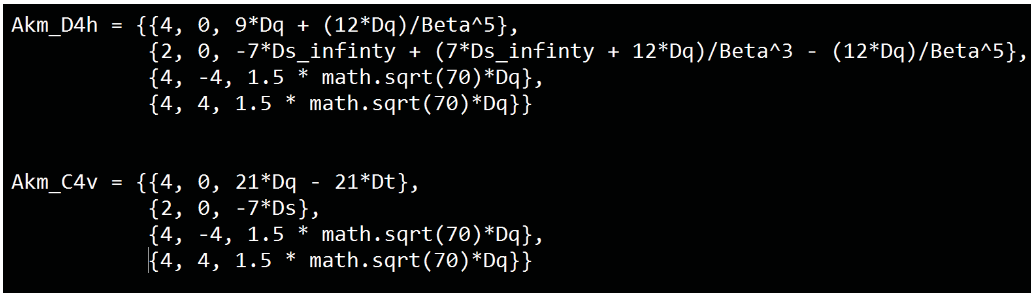

```
Akm_D4h = {{4, 0, 9*Dq + (12*Dq)/Beta^5},
          {2, 0, -7*Ds_infinty + (7*Ds_infinty + 12*Dq)/Beta^3 - (12*Dq)/Beta^5},
          {4, -4, 1.5 * math.sqrt(70)*Dq},
          {4, 4, 1.5 * math.sqrt(70)*Dq}}


Akm_C4v = {{4, 0, 21*Dq - 21*Dt},
          {2, 0, -7*Ds},
          {4, -4, 1.5 * math.sqrt(70)*Dq},
          {4, 4, 1.5 * math.sqrt(70)*Dq}}
```

Figure 82 – Adapted crystal field potentials for the symmetries considered in this work (D_{4h}, C_{4v}) with the inclusion of the distortion parameter $beta$ and the created crystal field parameter Ds_{∞}.

field potential expanded on renormalized spherical harmonics are written in the program utilized to obtain the XAS results for these two reduced symmetries.

Moving forward, the hybridization evaluation takes into account two crucial factors to ensure the accurate treatment of symmetry. First there is the definition of the operators associated with the specific unfolding of orbitals within each symmetry. For the symmetries D_{4h} and C_{4v}, four orbitals come into play, namely A_{1g}, B_{1g}, B_{2g}, and E_g. Furthermore, it is imperative to obtain precise hybridization energy values for each of these orbitals. These energy values are expressed in terms of Slater-Koster integrals [68] and can vary depending on the specific case. Regarding the operators, the existing implementation for D_{4h} symmetry serves as a foundation. Taking advantage of the shared orbital unfolding between D_{4h} symmetry and the square pyramidal case, the same operator definitions were seamlessly applied. This consistency is illustrated in Figure 83, where the operators for this section are depicted alongside the definition for octahedral symmetry.

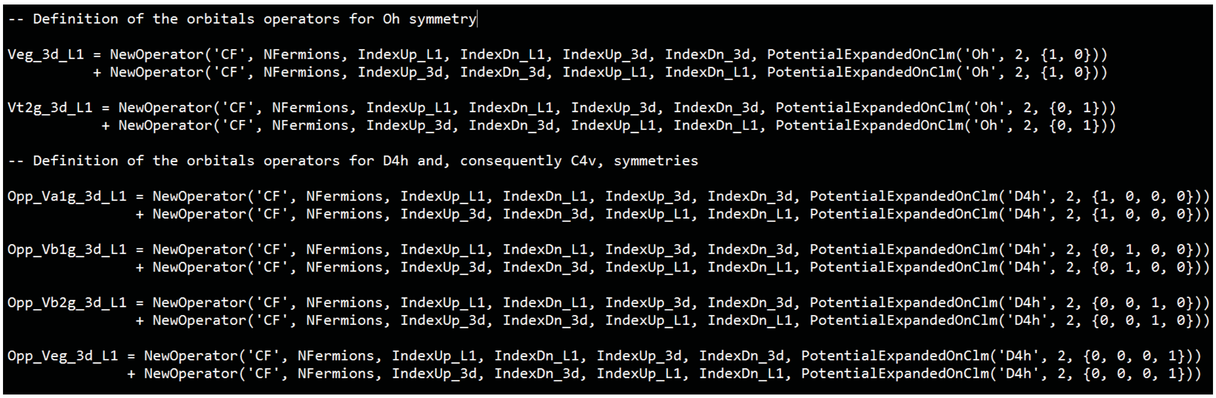

```
-- Definition of the orbitals operators for Oh symmetry

Veg_3d_L1 = NewOperator('CF', NFermions, IndexUp_L1, IndexDn_L1, IndexUp_3d, IndexDn_3d, PotentialExpandedOnClm('Oh', 2, {1, 0}))
          + NewOperator('CF', NFermions, IndexUp_3d, IndexDn_3d, IndexUp_L1, IndexDn_L1, PotentialExpandedOnClm('Oh', 2, {1, 0}))

Vt2g_3d_L1 = NewOperator('CF', NFermions, IndexUp_L1, IndexDn_L1, IndexUp_3d, IndexDn_3d, PotentialExpandedOnClm('Oh', 2, {0, 1}))
           + NewOperator('CF', NFermions, IndexUp_3d, IndexDn_3d, IndexUp_L1, IndexDn_L1, PotentialExpandedOnClm('Oh', 2, {0, 1}))

-- Definition of the orbitals operators for D4h and, consequently C4v, symmetries

Opp_Va1g_3d_L1 = NewOperator('CF', NFermions, IndexUp_L1, IndexDn_L1, IndexUp_3d, IndexDn_3d, PotentialExpandedOnClm('D4h', 2, {1, 0, 0, 0}))
               + NewOperator('CF', NFermions, IndexUp_3d, IndexDn_3d, IndexUp_L1, IndexDn_L1, PotentialExpandedOnClm('D4h', 2, {1, 0, 0, 0}))

Opp_Vb1g_3d_L1 = NewOperator('CF', NFermions, IndexUp_L1, IndexDn_L1, IndexUp_3d, IndexDn_3d, PotentialExpandedOnClm('D4h', 2, {0, 1, 0, 0}))
               + NewOperator('CF', NFermions, IndexUp_3d, IndexDn_3d, IndexUp_L1, IndexDn_L1, PotentialExpandedOnClm('D4h', 2, {0, 1, 0, 0}))

Opp_Vb2g_3d_L1 = NewOperator('CF', NFermions, IndexUp_L1, IndexDn_L1, IndexUp_3d, IndexDn_3d, PotentialExpandedOnClm('D4h', 2, {0, 0, 1, 0}))
               + NewOperator('CF', NFermions, IndexUp_3d, IndexDn_3d, IndexUp_L1, IndexDn_L1, PotentialExpandedOnClm('D4h', 2, {0, 0, 1, 0}))

Opp_Veg_3d_L1 = NewOperator('CF', NFermions, IndexUp_L1, IndexDn_L1, IndexUp_3d, IndexDn_3d, PotentialExpandedOnClm('D4h', 2, {0, 0, 0, 1}))
              + NewOperator('CF', NFermions, IndexUp_3d, IndexDn_3d, IndexUp_L1, IndexDn_L1, PotentialExpandedOnClm('D4h', 2, {0, 0, 0, 1}))
```

Figure 83 – Illustration showcasing the operators created for hybridization within the context of D_{4h} symmetry, leveraging the shared orbital unfolding with the square pyramidal case. The figure also includes the definition of symmetry for octahedral symmetry, providing a comprehensive overview of the implemented approach.

Concerning the definition of orbital energies, in both scenarios, the eigenvalues of the charge transfer matrix were computed. This matrix was constructed utilizing the findings detailed in the Slater-Koster article [68], augmented with additional elements, such as the distortion parameter β, to align with the specific objectives of this study. Figure 84 encapsulates the comprehensive definitions of all symmetries examined in this dissertation.

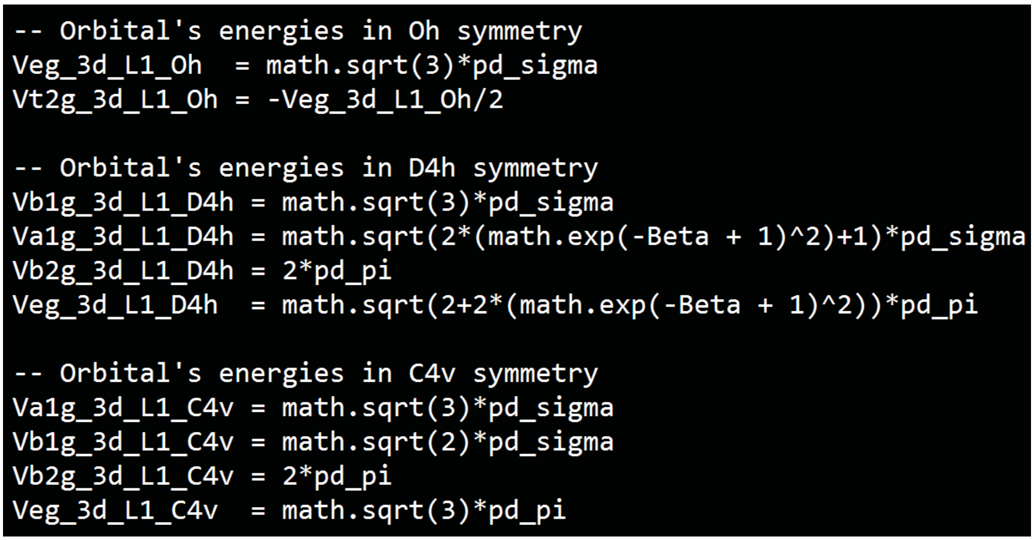

```
-- Orbital's energies in Oh symmetry
Veg_3d_L1_Oh  = math.sqrt(3)*pd_sigma
Vt2g_3d_L1_Oh = -Veg_3d_L1_Oh/2

-- Orbital's energies in D4h symmetry
Vb1g_3d_L1_D4h = math.sqrt(3)*pd_sigma
Va1g_3d_L1_D4h = math.sqrt(2*(math.exp(-Beta + 1)^2)+1)*pd_sigma
Vb2g_3d_L1_D4h = 2*pd_pi
Veg_3d_L1_D4h  = math.sqrt(2+2*(math.exp(-Beta + 1)^2))*pd_pi

-- Orbital's energies in C4v symmetry
Va1g_3d_L1_C4v = math.sqrt(3)*pd_sigma
Vb1g_3d_L1_C4v = math.sqrt(2)*pd_sigma
Vb2g_3d_L1_C4v = 2*pd_pi
Veg_3d_L1_C4v  = math.sqrt(3)*pd_pi
```

Figure 84 – Illustration depicting the determination of orbital energies in function of the Slater-Koster integrals. They were computed considering the elements required to approximate the symmetry being studied, such as the distortion parameter β in D_{4h}.

E.2 *MATLAB*

In the case of the *MATLAB* code [78], it was developed with the intuit of obtaining results regarding the XAS technique, more precisely the $O\ 1s$ edge of the compounds studied in this work. The code was originally already existent in the group, however, it did not have the covalence implemeted in the way possible to control the number of electronic configurations considered for each calculation, like it is done in *Quanty*. According to a determined number of electronic configurations, the program created basis files to be used in the evaluation of the ground and excited states. It is possible to consider from only 1 configuration until the maximum number required of ECs to account for all possible electron transitions until the d shell is complete.

The program encompasses four key functional steps. It begins with an initial filling state that corresponds to the nominal valence pertinent to the studied system, generating basis files. With these basis files, along with variable parameters, it is possible to create the ground and excited states for the system. This involves constructing the Hamiltonian and determining the eigenvalues and eigenvectors for both states. In addition, the program involves creating transition operators specific to the technique employed. Notably, for the focus of this thesis on X-ray Absorption Spectroscopy, the code simulates the oxygen $1s$-edge of the compounds presented in Chapter 4. Having covered two steps of the code, the ground and excited states of the system, along with their energies obtained through the diagonalization of energy matrices, are now known. This knowledge enables the calculation of intensities crucial to the generation of the final spectrum. The inclusion of Lorentzian and Gaussian functions to address lifetime and resolution effects results in the attainment of the desired outcomes, and this is done through a specific function created in the code. Originally, the program already contained the octahedral symmetry in the evaluations. In this case, it is a bit more simple to include the reduced cases, although it is similar to what was done in *Quanty*. Basically, it is required to modify the function responsible for creating the Hamiltonian operator by including the crystal field and hybridization factors that can be influenced by the symmetry being considered. Regarding the crystal field part, the results obtained for the parameters Dq, Ds, and Dt, where the latter two are written in terms of Ds_{∞} and Dq. Then, the contribution to the crystal field contribution is built by identifying in the basis which type of orbital the electrons present are and relating them with the correct relation of crystal field parameters, which can be seen in equation C.30, in Appendix C.2. Since it is quite an extensive code line, it will not be present here. Finally, to include the hybridization correctly according to the symmetry considered, a similar process was used. There is no need to create operators; however, the charge transfer process is accounted for by orbital energies written in terms of the Slater-Koster integrals [68], just as shown in Figure 85.

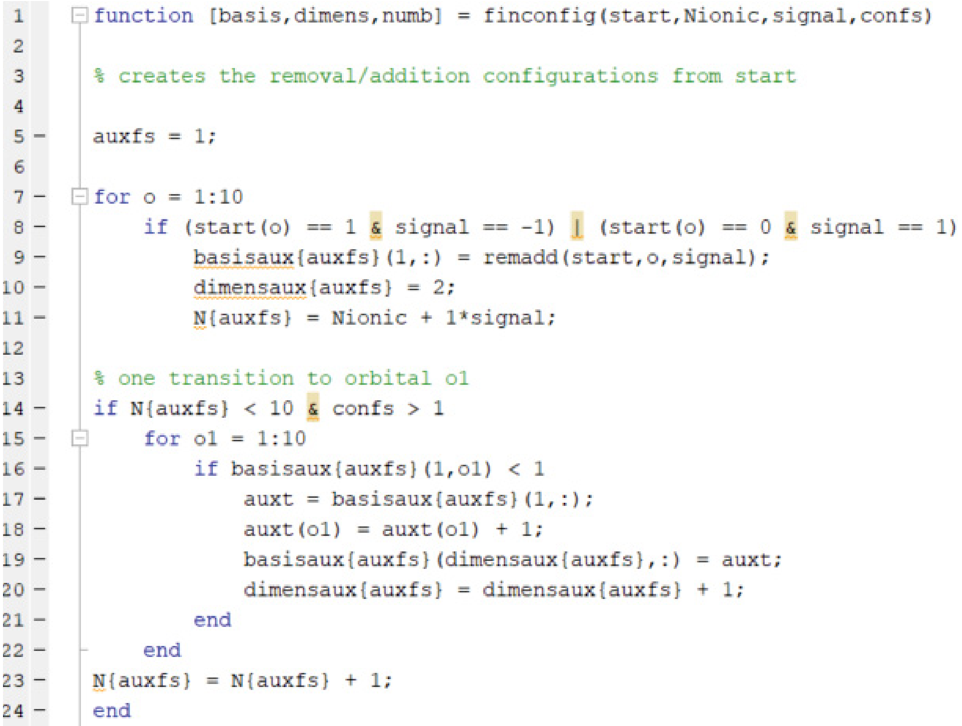

```
function [basis,dimens,numb] = finconfig(start,Nionic,signal,confs)

% creates the removal/addition configurations from start

auxfs = 1;

for o = 1:10
    if (start(o) == 1 & signal == -1) | (start(o) == 0 & signal == 1)
        basisaux{auxfs}(1,:) = remadd(start,o,signal);
        dimensaux{auxfs} = 2;
        N{auxfs} = Nionic + 1*signal;

% one transition to orbital o1
if N{auxfs} < 10 & confs > 1
    for o1 = 1:10
        if basisaux{auxfs}(1,o1) < 1
            auxt = basisaux{auxfs}(1,:);
            auxt(o1) = auxt(o1) + 1;
            basisaux{auxfs}(dimensaux{auxfs},:) = auxt;
            dimensaux{auxfs} = dimensaux{auxfs} + 1;
        end
    end
N{auxfs} = N{auxfs} + 1;
end
```

Figure 85 – Illustration on how the covalence is accounted in the *MATLAB* code. By defining a number of electronic configurations, the program is able to create the basis files that will be used to create the information about the ground and final states.

With all four steps here, it is possible to obtain information regarding ground and excited states like mean energy, number of electrons, and, of course, the XAS spectrum related to the O K-edge.

APPENDIX F

Curricular Data

F.1 Events Attended

1. **IX Simpósio de Estrutura Eletrônica e Dinâmica Molecular**. Brasília, Brazil. Poster presentation: Covalence Influence On X-ray Absorption Spectra On The 2p Edge Of Transition Metal Oxides (2022).

2. **IV Workshop of the Graduate Program in Physics of UFPR**. Curitiba, Brazil. Poster presentation: Covalence Influence On X-ray Absorption Spectra On The 2p Edge Of Transition Metal Oxides (2022).

3. **Brazilian Physics Society Autumn Meeting**. Ouro Preto, Brazil. Oral presentation: $L_{2,3}$ X-ray absorption spectra of transition metal oxides (Mn, Fe, Co): The influence of covalence effects (2023).

4. 41^{st} **International Conference on Vacuum Ultraviolet and X-ray Physics (VUVX 2023)**. Campinas, Brazil. Oral presentation: $L_{2,3}$ X-ray absorption spectra of transition metal oxides (Mn, Fe, Co): The influence of covalence effects (2023).

5. 15^{th} **International Conference on Electronic Spectroscopy and Structures**. Oulu, Finland. Poster presentation: $L_{2,3}$ X-ray absorption spectra of transition metal oxides (Mn, Fe, Co): The influence of covalence effects (2023).

6. **XVIII Escola Brasileira de Estrutura Eletrônica**. Campinas, Brazil. Poster presentation: Covalence effects on $L_{2,3}$ X-ray absorption spectra of transition metal oxides (V, Mn) with different symmetries (2023).

7. **V Workshop of the Graduate Program in Physics of UFPR**. Curitiba, Brazil. Oral presentation: Covalence effects on $L_{2,3}$ X-ray absorption spectra of transition metal oxides (V, Mn) with different symmetries (2023).